STRUCTURALLY AND ELECTRONICALLY RESPONSIVE METAL–ORGANIC FRAMEWORKS ASSEMBLED FROM A MODULAR BUILDING UNIT

by
Francis James Claire, III

A dissertation submitted to Johns Hopkins University in conformity with the requirements for the degree of Doctor of Philosophy

Baltimore, Maryland
March 2021

ABSTRACT

As interest in integrating metal–organic frameworks (MOFs) into active device architectures grows, it is necessary to develop effective methods for synthesizing high-quality materials with suitable electronic performance and responsive properties. We introduce a novel molecular building unit, $Mo_2(INA)_4$, for the modular assembly of a series of extended molecular frameworks. By modifying the solvent environment in which the molecular building unit assembles, we can control the structure of the resulting coordination polymer or MOF. From dimethylformamide solution, a one-dimensional linear coordination polymer, MF–101, crystallizes with an electronic structure distinct from that of the molecular species. Two-dimensional MOF structures, MF–102 and MF–103, are crystallized from dimethylacetamide solutions. The hierarchical pore structure of the 2D MOF exhibits unique CO_2 adsorption for an isotherm collected at 195 K. Cyclic voltammetry and electrokinetic analysis identify redox activity in the framework.

We demonstrate a new method for synthesizing high-quality MOF single crystals through chemical vapor deposition of the $Mo_2(INA)_4$ molecular cluster, MF–104. The resulting crystals have exceptionally uniform surfaces and can be grown to cover areas up to 8600 μm^2 and thicknesses down to 30 nm. Direct, reversible conversion between MF–102 and MF–104 is realized through solvent vapor exposure. Devices are fabricated from vapor-phase grown single crystals MF–104 and exhibit 30-fold changes in conductivity upon single crystal-to-single crystal phase conversion. Additionally, MF–104 crystals show reversible 8-fold changes in conductivity in response to illumination at modest powers.

Our method of modular MOF assembly from designer molecular building units shows promise in producing novel materials with structurally and electronically responsive properties. Chemical vapor deposition is shown to be an effective synthetic method for preparing high-quality MOF crystals and thin films for integration into advanced devices.

Advisor: Prof. Thomas J. Kempa

Thesis Committee: Prof. V. Sara Thoi
Prof. Arthur E. Bragg

ACKNOWLEDGEMENTS

First and foremost, I wish to express my gratitude and appreciation to my advisor, Prof. Thomas J. Kempa, for his incredible impact on my development as a scientist during my time at Johns Hopkins and for his friendship over the past five years. He provided me with the perfect balance of encouragement, motivation, inspiration, and guidance to be successful in all aspects of my life. His enthusiasm for rigorous science is contagious and has been one of my main motivating influences since joining his lab. Every time I have even the briefest conversation with Tom I learn something new, whether it's a complex physics concept or a fact about European history or the correct way to climb a boulder problem. (I will be able to climb as well as him soon!) Coming to JHU and joining the Kempa Group was the best decision I've ever made. Prof. Kempa fostered the greatest work environment one could hope for, enabling every one of his students to produce impressive scientific results while forming great friendships with our labmates that will last long after our time at JHU ends.

I am extremely lucky to have worked with so many great scientists and people as part of the Kempa Group. The long days and nights of working in lab were made enjoyable by being alongside great friends. Dr. Minyuan Li was a great mentor and teacher who introduced me to MOF chemistry when I first joined the Kempa Group. I would not have made it very far with inorganic synthesis without his synthetic expertise. The success of the MOF subgroup is due in no small part to Dr. Marina Solomos, who was instrumental in my development as a researcher. Marina's impressive work ethic and detailed experimental design constantly motivated me to improve as a scientist. And our ridiculous conversations at our desks are definitely a top highlight from my time at Hopkins. I was fortunate to work with so many great undergraduate researchers throughout my time at Hopkins. Stephany Tenney was integral to the development of many synthetic methodologies. Irina Chirca, Guillermo Contreras, Louie Hoffenberg, and Yuzuka Karube have all helped to push our MOF chemistry in new directions.

I have enjoyed the opportunity to introduce Dara Weiss and Zhenya Luo to the chemistry we have been working on in the MOF subgroup and it has been an honor to watch them each progress and improve as scientists over the past two years. I am confident that I am leaving the MOF subgroup in good hands with a lot of potential for future success and I am very excited to see what type of complex MOF devices Dara will make and how many new modular frameworks Zhenya will create.

I am thankful for all the great friendships I have made in the Kempa group. Tomojit Chowdhury, Erick Sadler, Ben Stephens, and Eric Thompson were all around from the very beginning of my time at Johns Hopkins and have made my entire graduate school experience more enjoyable. It was great to be surrounded by people who were willing to have equally deep and extensive conversations about science and/or D&D at all times. Marta Sliwa and every student who has joined the group since then has fit right in very quickly and I am grateful for our friendships.

Last but not least, I have to extend my sincerest gratitude to my family and all my friends who have supported and encouraged me through this whole process. After a long week in lab, nothing was better than to have great friends to commiserate with over jungle beers or a glass of whiskey. And thank you to my sisters, Dr. Claire for motivating me to keep improving academically, and Emily for motivating me to keep improving physically (I'm still better at climbing than you). And finally, a very special thank you to my parents for your endless love and support and for pretending to care about all the minute details of chemistry stories. My sincerest appreciation to everyone who has helped and motivated me along the way.

-Jamie

TABLE OF CONTENTS

LIST OF TABLES

LIST OF FIGURES

CHAPTER ONE

CHAPTER TWO

CHAPTER THREE

CHAPTER FOUR

CHAPTER FIVE

APPENDIX A

APPENDIX B

CHAPTER ONE

Developments in metal-organic frameworks enabling new science and next-generation devices

---

Selections from this chapter are published under the citation listed below and co-authored with the following authors:

Marina A. Solomos,[a] F. James Claire,[a] and Thomas J. Kempa*[a,b]

a. Department of Chemistry, Johns Hopkins University, Baltimore, MD 21218, USA

b. Department of Materials Science & Engineering, Johns Hopkins University, Baltimore, MD 21218, USA.

J. Mater. Chem. A, **2019**, 7, 23537–23562

1.1 Introduction: Metal–organic frameworks

Metal–organic frameworks (MOFs), and more broadly coordination polymers (CPs), are versatile materials comprised of organic ligands coordinated to metal centers that form extended networks in one, two, or three dimensions.[1-3] These materials have garnered significant scientific attention in the past two decades due primarily to their innate physical properties, large pore volumes, and high surface areas. These properties can be tuned through judicious selection of organic and inorganic components to produce MOFs for a wide range of applications, from gas storage to catalysis to ion separation.[1-11] Such applications take advantage of the passive properties of MOFs which can be modified during the design process to produce desired properties. For example, large organic linkers can be used to create larger stable pores within the framework and appropriately functionalized ligands can facilitate selective catalytic transformations.

There has recently been significant interest in developing MOFs with active or responsive properties in order to realize more complex device concepts, including sensors, switches, and actuators.[12-17] To date, these devices are primarily fabricated from inorganic semiconductor materials such as silicon and transition metal dichalcogenides (TMDs). MOFs are promising candidates to enable next-generation active devices, but there are two important criteria that must be met to realize this:[18-22]

1. *MOFs must be designed with structures and properties that can be manipulated by external stimuli.*
2. *The synthetic methods must produce high-quality crystalline MOFs to enable their seamless integration into device architectures.*

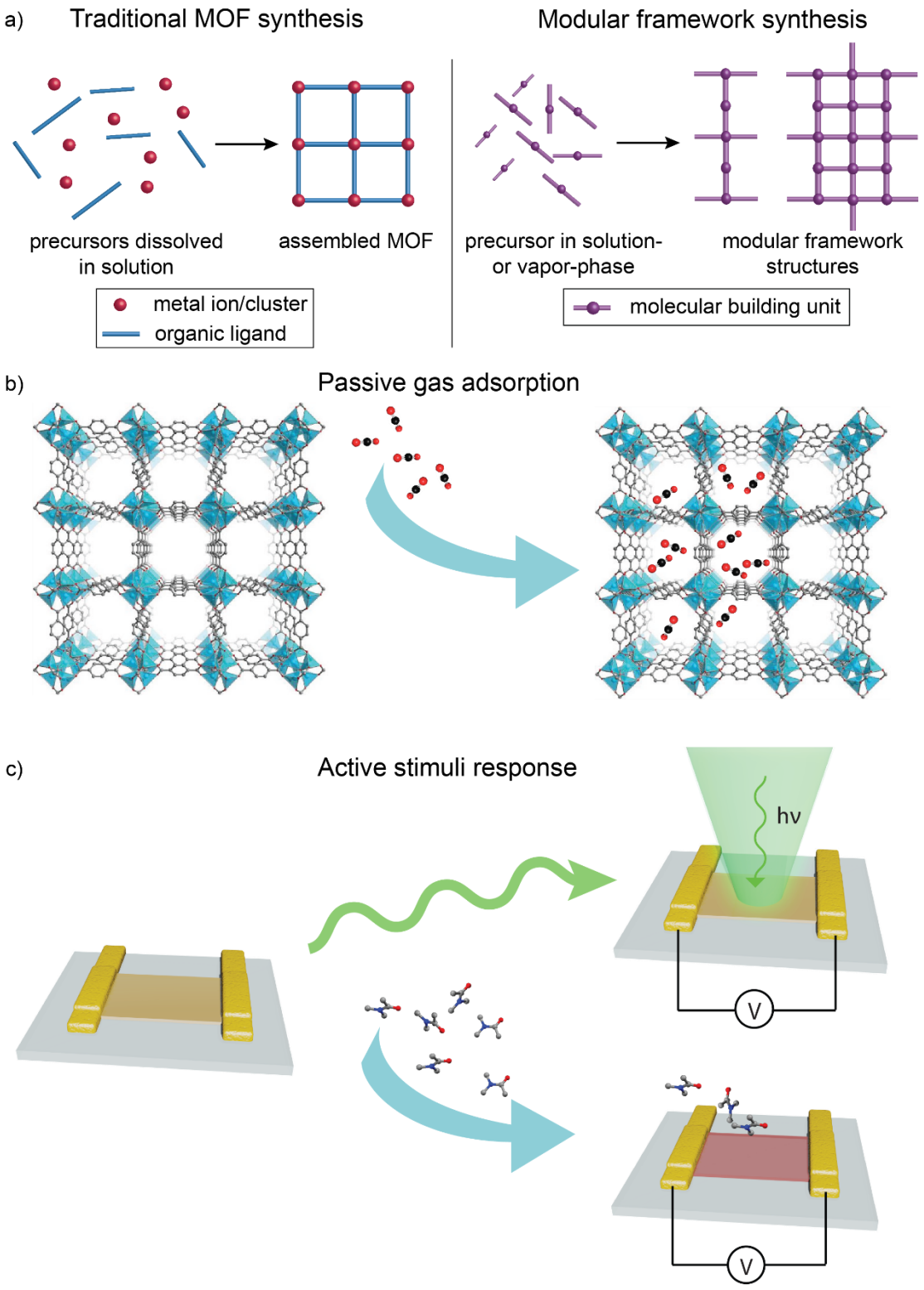

Figure 1.1 | (a) Comparison of traditional MOF syntheses involving metal clusters and organic ligands dissolved in solution versus our new modular synthetic method involving a single precursor which can be assemble into molecular framework from the solution phase or vapor phase. (b) Passive properties of MOFs such as their large pore volume enable storage of large

quantities of CO_2. (c) MOFs with responsive properties can be integrated into active devices that exploit conductivity changes in the material in response to external stimuli of optical irradiation (top) and solvent intercalation (bottom).

Our work aims to address these challenges in an effort to develop novel molecular framework materials suitable for implementation into active devices. We introduce a series of frameworks assembled from the $Mo_2(INA)_4$ molecular building unit through novel solution- and gas-phase synthetic methods.[24-26]

1.2 Background: Two-dimensional metal–organic frameworks

To appreciate the emerging opportunity in the study of 2D molecular crystal lattices, specifically MOFs, one need only to look at the massive attention dedicated over the past 10 years to 2D atomic crystals. Graphene, graphene analogs of the Group IV elements, and single-layer TMDs are 2D atomic crystals that exhibit in-plane covalent bonding, out-of-plane van der Waals interactions with their surroundings, and electronic and optical properties that are distinct from those found in their bulk parent solids.[27–33] These materials are frequently classified as van der Waals solids and can be combined with one another to yield so-called van der Waals heterostructures encompassing expanded or hybrid properties.[34]

In this vein, 2D MOFs are a compelling platform on which to discover new emergent properties and expand the library of 2D materials.[35–40] Two-dimensional molecular crystals can be synthetically designed and subsequently tuned to target a multitude of desirable material properties.[13,41–44] Porous by nature, 2D MOFs offer higher surface areas than their bulk counterparts, heightened guest capture[45] and sensing[46] abilities, new charge transport modalities,[47] and improved catalytic performance.[48,49] Moreover, the extensive internal surfaces within MOFs can be post-synthetically modified to introduce additional tailorable functionalities.[41,49] Notably, the reduced dimensionality, the access to diverse bonding motifs,

and the tunable symmetry and size of unit cells within 2D molecular lattices raises the tantalizing prospect for design and discovery of new properties that, in turn, could be leveraged to create a new generation of optoelectronic devices.[3,50–52]

The appeal of 2D MOFs, molecular nanosheets, and crystalline thin films is well established within the solid-state community.[42,47,51,53–58] Past and current efforts consistently emphasize the need for improved thin film fabrication techniques. These methods must yield high-quality materials with minimal crystallographic defects and uniform surfaces, while exerting precise control over their dimensions.[59,60] Ideally, these methods should be scalable, facile, and cost-efficient to facilitate large-scale production of 2D molecular crystals. High-quality films of MOFs are characterized as having strong substrate interactions, uniform pore orientation, and well-defined layers.[61,62] In addition to these requirements, the preparation of singly- or highly-crystalline thin films over large areas is necessary for the integration of 2D MOF into devices and other architectures.[61,63] New molecular systems and synthetic methods, or adaptations of existing synthetic methods, as well as new characterization techniques, are required to accomplish these goals.[48]

Though many methods exist for the growth of polycrystalline, micrometer-thick MOF films, to-date very few methods can grow high-quality crystalline thin films approaching the single-layer limit. Standard preparative routes target anisotropic crystal dimensions by inhibiting MOF layer assembly (e.g. through interfacial synthesis and surfactant assisted growth), while substrate-directed growth methods rely on surface functionalization or patterning to template MOF thin films as they grow layer-by-layer.[62,64,65] These “top-down” and “bottom-up” approaches have, in turn, led to a variety of promising techniques that improve thin film crystallinity and approach monolayer thicknesses by targeting the nucleation of molecular crystals. As the quality of 2D MOF and thin films improves, their incorporation into multifunctional materials will be realized.

1.3 Synthetic methods for 2D MOFs

Solution-based synthetic methods for the preparation of crystalline thin films of molecular systems are well established. Though preferred by most researchers, solution-based growth struggles to afford a high degree of control over thin film quality just as solvent-based bulk recrystallization of MOFs remains a perennial challenge. Numerous problems conspire against the formation of consistently high-quality MOF thin films, including the formation of defects, polycrystalline domains, metastable phases, and macroscale cracks. To address many of these concerns, as well as eliminate unwanted solvent effects, the preparation of thin film molecular crystals via gas phase methods has recently gained attention as a promising approach to the deposition of uniform layers of molecular materials with control of thickness. In combination with patterned templates or functionalized substrates, the discovery of molecular framework systems capable of forming ordered crystalline thin films from the gas-phase has the potential to transform 2D MOF studies.

1.3.1 Solution-phase syntheses

Two-dimensional MOF nanosheets are frequently synthesized from solution by adapting or expanding upon traditional solvothermal strategies employed for preparation of the corresponding bulk phases. As is the case during preparation of 2D atomic crystals, exfoliation of MOF crystals is able to disrupt van der Waals contact forces and yield a layered lattice. However, gentler, solution-based exfoliation methods are often required to prevent substantial damage to the framework's crystalline structure. In many cases, the layered structure of MOFs lends itself well to simple sonication delamination.[66,67]

Initial wet ball-milling of bulk MOF crystals in methanol and propanol at slow speeds was shown by Yang et al.[48] to facilitate methanol penetration between constituent $Zn_2(bim)_4$ layers and to stabilize the resultant nanosheets prior to further exfoliation by sonication

(**Figure 1.2**). The nanosheets have uniform thicknesses and are reported to be as thin as 1.12 nm, which is consistent with a monolayer. Sun and co-workers[68] recently reported a facile method for sonication exfoliation of a cobalt and pyrazine based MOF, $Co(CNS)_2(pyz)_2$, in ethanol for 30 minutes. The product was collected by rotary evaporation and was found to consist of monolayer nanosheets, which exhibited solvatochromic behavior and were subsequently implemented as solvent polarity sensors.

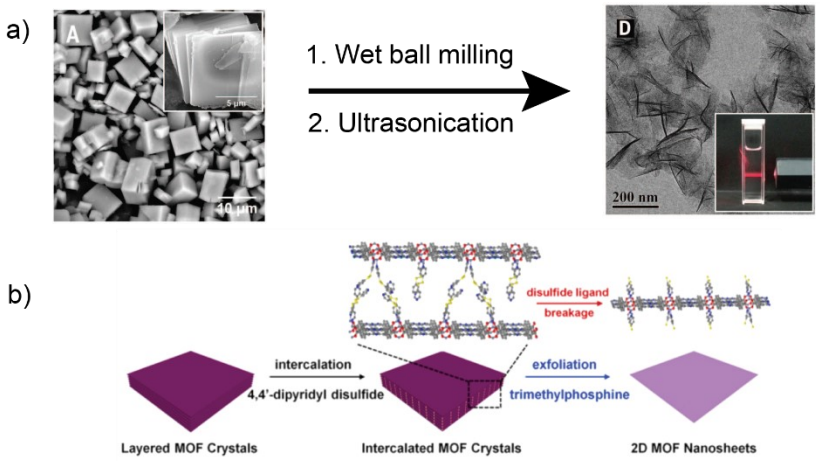

Figure 1.2 | (a) SEM image of as-synthesized $Zn_2(bim)_4$ crystals (left) which undergo wet ball milling and ultrasonication to exfoliate single layers. TEM image of exfoliated nanosheets (right). The inset shows Tyndall scattering of the colloidal solution of nanosheets. (b) Schematic representation of the chemical exfoliation process using 4,4'-dipyridyl disulfide to produce single MOF nanosheets. From *Science*. **346**, 1356–1359 (2014). Reprinted with permission from AAAS. Reprinted (adapted) with permission from *J. Am. Chem. Soc.* **139**, 9136–9139 (2017). Copyright 2017 American Chemical Society.

Chemical exfoliation methods have also been used to disrupt layered frameworks. PPF-1 MOF crystals, comprised of porphyrin sheets assembled from zinc paddlewheels, were exposed to 4,4'-dipyridyl disulfide to form a new, intercalated 3D MOF. Selective reduction of the disulfide bond by trimethylphosphine yielded ~1 nm thick MOF nanosheets. Zhou et al.[69] compared their method to surfactant-assisted exfoliation and found chemical exfoliation to be better suited for extracting single layer nanosheets (**Figure 1.2**). Similarly, Zhang et al.[70]

designed a layered MOF incorporating 2,3-dihydroxy-1,4-benzenedicarboxylic acid as a redox-active pillar ligand. Selective oxidation of the pillar ligands realized conversion of the 3D MOF to ultrathin 2D nanosheets (~2 nm thick) in O_2 saturated electrolyte solutions. Delamination of $Cu_2(bdc)_2$ MOF crystals in oleylamine was demonstrated by Kaskel and coworkers[71] to yield ~70 nm thick sheets. The authors found that addition of PVP during crystallization of the parent $Cu_2(bdc)_2$ bulk phase yielded thinner (4–14 nm) 2D MOF sheets after exfoliation in oleylamine. Foster et al.[72] use a strategy of chemical design and ultrasonic exfoliation to prepare copper-based MOF nanosheets. They installed hydrophobic or hydrophilic pendant ligands in the parent bulk MOF phase and attempted exfoliation in solvents of ranging polarities. Sonication in acetonitrile for 12 hours yielded nanosheets as thin as 2–10 nm, and found that the nanosheet dimensions could be tuned through judicious choice of exfoliation solvent, sonication duration, and centrifugation time.

Interfacial syntheses using solution phases of metal and linker are another route towards the preparation of nanosheets and include strategies such as direct mixing, liquid-liquid layering, or three liquid layering processes. Inspiration for these strategies comes from success in preparing large area MOF films of controlled thickness at vapor-liquid interfaces.[73] Tsapatsis et al.[74] showed that Cu(BDC) nanosheet formation is possible by mixing of copper (II) nitrate trihydrate in DMF and acetonitrile with a 1,4-benzenedicarboxylic acid solution. Either no mixing or gentle agitation formed ~25 nm thick Cu(BDC) nanosheets, which were readily collected by centrifugation. These nanosheets were then incorporated into mixed-matrix membranes, which exhibited an increased matrix selectivity for CO_2/CH_4. Thicker Cu(BHT) films were prepared by Zhu et al.[75] using a liquid-liquid interface reaction between aqueous copper (II) nitrate and benzenehexathiol in dichloromethane. The films, which can be clearly identified as forming at the interface, range in thickness from 20–140 nm, with thicker films exhibiting increased surface roughness. Films of 15–500 nm thickness were

transferred to substrates and exhibited record conductivities ranging from 750–1580 S cm^{-1}.

Using a three-layer approach, Gascon et al.[76] demonstrated the formation of 5–25 nm thick Cu(BDC) nanosheets by separating layered solutions of the copper (II) nitrate and 1,4-benzenedicarboxylic acid precursors with an intermediate solvent layer. Slow diffusion of metal ions and BDC linker molecules forms MOF films within the intermediate layer. In yet another adaptation of liquid-liquid interfacial reactions, Su et al.[77] formed large area thin films of two new MOFs, Au_3BHT_2 and Ag_3BHT_2, by forming an organic solvent-water interface in a large dish with a SiO_2-coated silicon wafer resting at the bottom. Slow injection of a metal ion solution into the organic layer facilitated the formation of thin films of Ag_3BHT_2 and Au_3BHT_2 in 30 min and 6.5 hours, respectively. The MOF thin films were deposited onto the SiO_2 substrate through careful removal of the solvent. Though the films are several hundreds of nanometers thick and contain defects, the Ag-containing MOF exhibited a significant conductance of 363 S cm^{-1}.

As seen in the examples above, interfacial synthesis is effective at limiting growth of molecular materials perpendicular to the interface and is therefore commonly used to prepare 2D MOF materials. The incorporation of a surfactant during nucleation and growth of MOFs has also been shown to be effective in encouraging the formation of nanosheets. Zhang et al.[78] developed a surfactant-assisted method for the formation of 2D Zn-TCPP MOF nanosheets. When introduced as a reagent during conventional MOF synthesis, polyvinylpyrrolidone (PVP) selectively attaches to zinc cations on the MOF surface and leads to anisotropic growth. Zn-TCPP nanosheets 7.6 ± 2.6 nm thick were achieved and correspond to 8 ± 3 layers of Zn-TCPP per nanosheet. Tsapatsis et al.[79] also demonstrated the utility of surfactant incorporation during MOF synthesis by mixing a metal precursor and ligand in a suspension of CTAB in heptane and hexanol. The selective binding of CTAB to the major

crystal planes of Zn(Bim)OAc in conjunction with optimization of temperature conditions facilitates the formation of surfactant-free MOF nanosheets with 7 nm thicknesses (**Figure 1.3**).

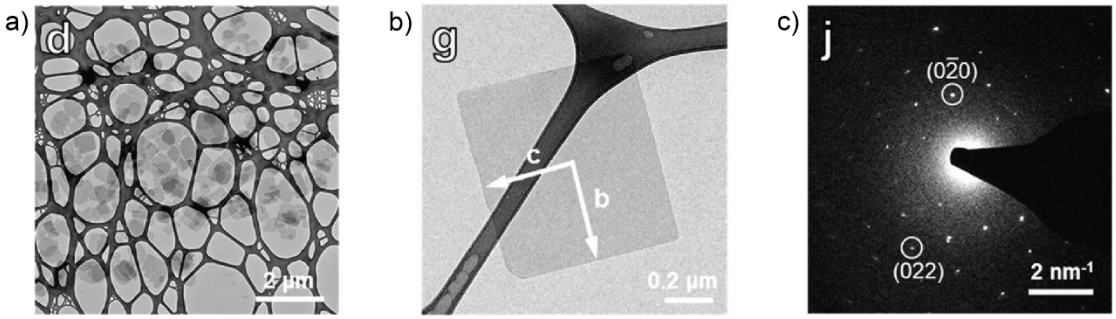

Figure 1.3 | TEM images of (a) several nanocrystals and (b) single nanocrystal Zn(Bim)OAc synthesized in a suspension of CTAB in heptane and hexanol at 25 °C. (c) Corresponding electron diffraction pattern of single nanocrystal. Reprinted (adapted) with permission *Chem. Mater.* **30**, 69–73 (2018). Copyright 2018 American Chemical Society.

To enable their eventual incorporation into more functional materials and devices, MOF nanosheets must be either transferred to or selectively grown on substrates. Adapting the layer-by-layer process (LbL), Kitagawa et al.[80] utilized standard solvothermal techniques to prepare nanoflakes of a range of MOFs. In one example, the authors prepared Cu-TCPP nanoflakes, approximately 15 nm or 33 porphyrin layers in thickness, suspended them in ethanol, and then added them dropwise to the surface of water, thereby assembling a thin film which could be transferred to assorted substrates through a simple stamping process. Characterization of the thin film revealed that it has a crystallinity and orientation similar to that of the SURMOF bulk phase. Coronado et al.[81] prepared MOF thin films as thin as 10 nm by dipping functionalized substrates (silicon, gold, and permalloy) into a CoTCPP-pyridine solution, which had been dispersed over a copper (II) nitrate solution. The functionalized substrates successfully directed the transfer of MOF nanosheets onto suitable interfaces for device integration, whereas bare substrates exhibited poor or failed transfer.

As an alternative to the transfer of MOF films onto substrates, MOF thin films can be directly grown on selected regions of a substrate if the desired areas are pre-functionalized with self-assembled monolayers (SAMs).[82,83] Wöll et al. demonstrated the utility of functionalized substrates for the bottom-up assembly of MOF thin films.[62,84–86] Gold surfaces functionalized with 11-mercapto-1-undecanol were subjected to sequential, layer-by-layer (LbL) depositions of metal and ligand solutions (liquid phase epitaxy), with growth cycles monitored by a quartz crystal microbalance (QCM). Resultant MOF films were 64–80 nm thick and loaded with assorted metal ions. Further work on carboxylate-functionalized Au surfaces showed that MOF thin films with similar thicknesses can be prepared by spray coating metal and ligand solutions sequentially. Performing LbL growth on QCMs, Allendorf et al. have shown that both functionalized semiconductor surfaces[87,88] and patterned substrates[89] are able to facilitate growth of two or three unit cell thick, stacked crystalline MOF sheets of HKUST-1. While monitoring the MOF assembly process with QCMs, Fischer and coworkers[90] alternately deposited $Zn_4O(OAc)_6$ solution and various 3,5-dialkyl-4-carboxypyrazolate linkers onto functionalized gold sensors to form crystalline thin films of $[Zn_4O]^{6+}$ MOFs. The influence of acetic acid modulators, which are added to either the metal or ligand solutions prior to LbL assembly, on the crystallinity of the thin films was assessed. Marks, Stoddard, and colleagues[91] prepared gamma-cyclodextrin (CD) self-assembled monolayers to facilitate the epitaxial growth of CD-MOF polycrystalline thin films on glass substrates. The large-area surface coverage and oriented growth (2 μm) of these films allowed for their direct incorporation into a functional device with enhanced proton conductance and CO_2 sensing abilities. Hupp[92] also prepared surface-supported, patterned films of ZIF-8 for the formation of hybrid materials with vapor sensing capabilities.

1.3.2 Vapor-phase syntheses

Solution-based methods enjoy widespread use in the preparation of molecular films, but recent attention has focused on solvent-free and gas phase deposition strategies. Just as atomic layer deposition (ALD) and chemical vapor deposition (CVD) are commonly used for the synthesis of 2D materials,[93,94] molecular layer deposition (MLD) and CVD are now becoming attractive candidates for the preparation of high-quality crystalline MOF thin films.[95–98] Ritala et al. prepared of MOF-5 thin films by ALD[99] through iterative application of zinc acetate and 1,4-benzenedicarboxylic acid precursor pulses within a hot wall reactor. The initially deposited amorphous material was transformed into MOF-5 upon water vapor exposure. Ameloot and coworkers have further demonstrated the promise of solvent-free preparative routes. They showed that heating a zinc oxide film covered with a thin layer of 2-methylimidzaole to 433 K produces ZIF-8 within one minute.[100] More recently, Ameloot et al. used CVD[101] to deposit zinc oxide on a range of flat and textured substrates, and then treated these substrates with 2-methylimidazole vapor under ALD conditions (**Figure 1.4**). This two-step process yielded continuous 52–104 nm thick ZIF-8 polycrystalline films (**Figure 1.4**).

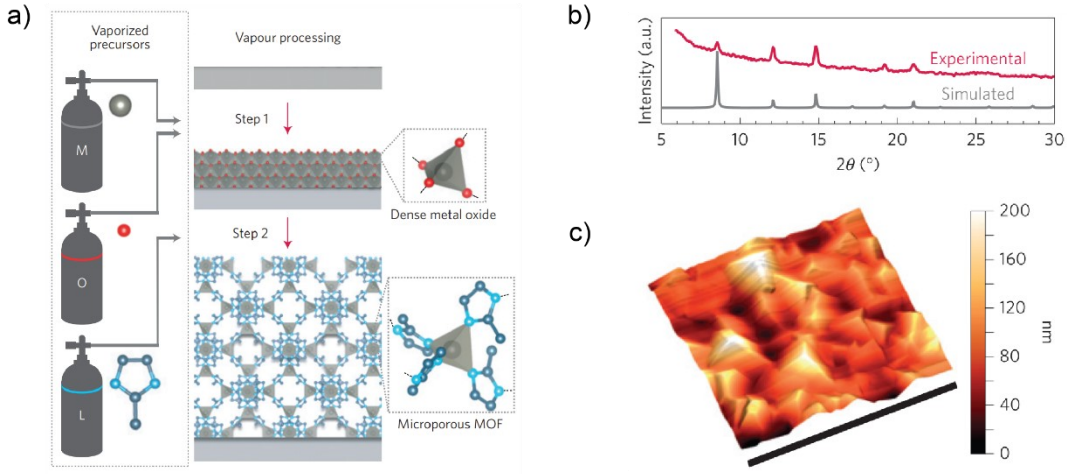

Figure 1.4 | (a) Schematic representation of CVD synthesis of ZIF-8 through a two-step process of depositing dense metal oxide followed by introduction of organic ligand. (b) conversion of ZnO to ZIF-8 observed via pXRD pattern of film compared to simulated ZIF-8. (c) 3D rendered AFM topograph of polycrystalline film. Adapted by permission from Springer Nature: *Nat. Mater.* **15**, 304–310 (2016). © 2016

These vapor-phase synthetic methods show promise in produce MOF thin films, though they lack in precise control to form high-quality single crystals. In our work, we have utilized a single-step CVD reaction to grow directly ultra-thin single crystals of a MOF comprised of dimolybdenum paddlewheel clusters (**Chapter 4**).[24-26] These high quality and phase pure single crystals have exceptionally uniform surfaces, are highly oriented, and can be mechanically exfoliated to yield singly crystalline thin films with thicknesses approaching several nanometers. Our work represents the first effort to prepare singly crystalline MOF thin films from the gas phase.

1.4 Characterization

Thorough characterization of 2D or nearly-2D molecular materials is of paramount importance in the quest to discover promising properties that may manifest within these materials, and in the ongoing effort to develop new synthetic strategies to address exigent challenges discussed above. Several features of a MOF thin film or few-layer nanosheet must be determined in order to inform its subsequent application: (1) film quality, (2) material phase, (3) nanosheet dispersion, (4) stability, and (5) pore size. Most bulk MOF characterization techniques can be translated to the analysis of dimensionally restricted materials without requiring major modification. However, careful attention must be paid to data quality and interpretation of results, because sample variability can introduce systematic errors and because properties measured on bulk materials may be significantly altered when the same material takes on a nanoscale dimension. Though tedious, multiple nanosheets or thin films should be individually characterized to build a robust, statistically-significant dataset. Furthermore, powerful in situ techniques—which may need to be modified or developed specifically for 2D molecular materials studies—will aid in assessing the aforementioned features during synthesis and device fabrication.

Since single crystal X-ray diffraction is usually impossible due to the inherently lower dimensionality of nearly-2D molecular films, these materials are frequently characterized with powder X-ray diffraction (pXRD). pXRD allows for relatively straightforward assessment of sample crystallinity, phase, and layering/lattice spacing, but often requires bulk samples, which may not be representative of the individual films, and a known crystal structure to serve as a reference (**Figure 1.5**).[76] Though Aida et al.[102] were successful in obtaining single crystal structures of their self-exfoliating Cu(II) MOF, pXRD proved useful in studying the accordion-like expansion process their MOF was able to undergo. Upon exposing their MOF to THF vapor, the authors observed an interlayer expansion that was represented by large shifts of the (001) peak in 2θ. This result corroborated previously observed large increases in the interlayer d-spacing from 6.8 Å to 17.0 Å prior to self-exfoliation. Wöll et al.[103] employed out-of-plane pXRD to assess the lattice-constants of their liquid-phase epitaxially-grown, heterostructured SURMOFs and to confirm the orientation of their thin film. pXRD can also be used to monitor growth processes and the effects of modulators on film phase, as Ameloot et al. did in monitoring acetic acid vapor modulation on UiO-66 films.[104] Synchrotron X-ray diffraction and grazing incidence X-ray diffraction (GIXD) can provide additional information regarding the internal layers of a thin film.[105,106]

Other characterization methods that provide chemical information include Fourier-transform infrared (FT-IR), Raman,[107–109] and solid state nuclear magnetic resonance (NMR) spectroscopies.[110,111] Also commonly used in the MOF community, Brunauer–Emmett–Teller (BET) analysis probes the pore structure of thin films and nanosheets by fitting their gas adsorption-desorption[95,112,114] isotherms. Calculated surface areas from BET analysis indicate the accessible pore volume of MOFs and are used to compare these materials on the basis of their gas storage potential or permeability.

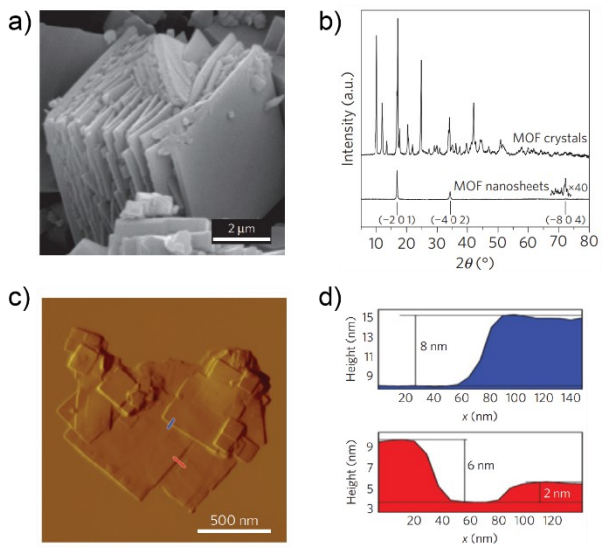

Figure 1.5 | (a) SEM image of bulk CuBDC MOF crystals comprised of layered MOF nanosheets. (b) pXRD comparison of bulk CuBDC MOF crystals vs. nanosheets. (c) AFM image of MOF nanosheets with (d) height profiles along indicated regions used to precisely measure the thickness of single- to few-layer crystals. Adapted by permission from Springer Nature: *Nat. Mater.* ***14****, 48–55 (2015).* © 2015

In contrast to these aforementioned techniques, which are most often performed on bulk quantities of sample, optical microscopy and atomic force microscopy (AFM) are most informative when deployed on individual specimens or distinct and smaller regions of a sample. Optical microscopies, especially those encompassing dark-field and phase-contrast imaging, are useful for visualizing film quality and surface defects in larger crystals or large-area thin films, though probe depth and resolution are defined by the energy and intensity of the optical beam, parameters of the microscope optics, and the Abbe diffraction limit. Zhao et al. could clearly observe the surface roughness of their millimeter-wide Cu-TCPP thin films by visualizing regions having different textures and color saturations.[112] Atomic force microscopy (AFM) is considerably more useful for analyzing the surface roughness and thickness of nanoscale thin films. Most analyses of exfoliated thin film MOFs utilize AFM to measure the step-heights of individual layers within a multi-layer film.[67,76,115–117] The angstrom-level z (height) resolution of AFM facilitates comparison of AFM acquired step-heights to known crystal lattice spacings, provided that the 2D layers are properly oriented.

Electron microscopy, which encompasses a range of advanced techniques including scanning electron microscopy (SEM), transmission electron microscopy (TEM), scanning transmission electron microscopy (STEM), and, most recently, in situ and aberration-corrected TEM/STEM, is used to obtain high-resolution to atomic-resolution data of ultrathin molecular materials. The insulating nature of many MOFs presents imaging challenges, though many of these can be overcome through the use of conductive support films and coatings, which provide effective charge dissipation. The complementary resolution levels of SEM and TEM images provide excellent structural insight across multiple lengthscales. SEM often lends morphological insight regarding the likelihood that a sample can be readily exfoliated[118] and TEM provides an assessment of the crystallinity and inter-layer alignment within multi-layer films.[119] When combined with energy-dispersive X-ray spectroscopy (EDS), SEM or TEM can also provide elemental mapping of the sample's surface.[57,115,120,121] Though less frequently used, scanning tunneling microscopy (STM) is a powerful technique that allows for the imaging of single MOF = layers on metal substrates and provides atom-level resolution and electronic structure information at the monolayer level.[122–125]

The choice of characterization technique can also be guided by the intended application of the 2D nanosheet. For some systems, magnetic susceptibility measurements are useful for investigating electronic structure and bonding. Gómez-García and coworkers identified ferromagnetic Fe-Fe interactions in their MOF systems likely arising from mixed-valency of the Fe(II)/Fe(III) lattice.[66] For these and other functional MOF systems, authors are increasingly providing charge transport measurements.[114,126–128]

Crystalline thin films and nanosheets can change their phases and associated properties which mandates the development and use of in situ characterization methods to monitor and potentially control solid-state transitions.[129] More importantly, in situ analysis of MOF thin film growth would provide valuable insights regarding plausible mechanisms for

formation of these coordinated frameworks. In turn, such studies could inform design and optimization of reactions to achieve higher quality 2D molecular materials. An assortment of in situ X-ray diffraction techniques is currently available but their widespread use is limited.[130] Methods to monitor morphology and crystallinity, such as in situ SEM[131] and TEM,[132] exist and are employed for 2D atomic materials but have not been readily used for analysis of molecular systems. Weckhuysen et al. developed an in situ AFM method and used it to monitor HKUST-1 thin film growth by observing a 10 x 10 μm section of Cu-BTC solution deposited on a functionalized Au substrate.[133] Nucleation of copper and BTC linker was observed and HKUST-1 grain formation could be monitored at several temperatures. In an effort to provide chemical information, Parsons et al. developed an in situ technique for attenuated total reflectance infrared spectroscopy.[134] The formation of HKUST-1 was monitored by examining the conversion of ZnO and $Cu(NO_3)_2$ to the MOF upon addition of H3BTC. The symmetric and asymmetric stretching modes of the HKUST-1 carboxylate groups were monitored every 0.49 seconds. Continued development of in situ characterization techniques for 2D molecular materials will undoubtedly advance further investigation of these systems.

1.5 Studies and Potential Applications

While researchers continue to explore the potential of true 2D MOFs, these materials have demonstrated impact in a number of electronics, energy storage, catalysis, and biomedicine applications. The plethora of fundamental studies and applications enabled by 2D atomic crystals bodes well for the potential impact of 2D molecular frameworks, which allow for an exceptional degree of freedom in chemical design. We anticipate that collaboration between the solid-state, inorganic, and condensed matter communities will spawn new research areas with extraordinary potential.

1.5.1 Charge transport and storage

The prospect of eliciting efficient and tunable charge transport and storage in 2D MOFs has driven extensive research over the past decade.[42,43,63,135–138] Multiple groups have developed graphene-like MOFs in hopes of achieving record values for conductivity or capacitance.[139–142] Dincă et al. produced one of the most highly conductive MOFs, $Ni_3(HITP)_2$, and subsequently prepared films with 500 nm thicknesses. Films deposited on quartz substrates resulted in room temperature conductivities of 40 S cm^{-1} and also exhibited higher conductances with increasing temperature.[141] Canovas et al.[143] identified a 2D MOF, $Fe_3(THT)_2(NH_4)_3$, with a room temperature carrier mobility of 220 $cm^2 V^{-1} s^{-1}$ and a direct bandgap of 0.25 eV. These semiconducting films were prepared by an interfacial growth method that yielded large area, multilayer samples.

Gómez-García and coworkers[66] further characterized both of their mixed-valence, magnetic Fe(II)/Fe(III) MOFs and reported room temperature conductivities of 0.03 and 0.003 S cm^{-1} for bulk crystals when measured parallel to the honeycomb MOF structure. Their measurements revealed much lower conductivities ($\sim 10^{-4}$ and 10^{-6} S cm^{-1}) when measuring perpendicular to the honeycomb layer. Though nanosheets of these MOFs were produced, their associated carrier conductivities were not reported. Conversely, Nishihara et al.[128] successfully prepared nanosheets of their nickel bis(dithiolene) complex and reported a conductivity of 160 S cm^{-1} for a single crystalline flake using a four-point probe setup within an SEM. Also using four-point probe measurements, Zhu et al.[75] recorded a high conductivity of 1580 S cm^{-1} for their copper benzenehexathiol (Cu-BHT) coordination polymer. Field effect transistors (FETs) were subsequently prepared from the Cu-BHT films and exhibited high hole- and electron-mobilities, with a single FET device managing to exhibit a hole mobility of 99 $cm^2 V^{-1} s^{-1}$ and electron mobility of 116 $cm^2 V^{-1} s^{-1}$. Xu et al.1[73] also fabricated a FET

incorporating a $Ni_3(HITP)_2$ membrane prepared via an air-liquid interfacial method. Multiple devices indicated hole mobilities ranging from 38 ± 8 $cm^2\ V^{-1}\ s^{-1}$ to 48.6 $cm^2\ V^{-1}\ s^{-1}$. The authors hypothesized that these high values result from extensive charge delocalization within the layers, which are comprised of nickel ions coordinated to ligands with radical character. Close-packing of each vertical layer may also introduce opportunistic π-π interactions.

Focusing on their $Ni_3(HITP)_2$ material, Dincă et al. prepared the first solely MOF comprised electrochemical double layer capacitors (EDLCs) and showed that their devices reach a normalized gravimetric capacitance of 18 μF cm^{-2}, exceeding the values observed in most carbon materials.[144] These results encourage continued efforts to demonstrate the unique potential of MOFs as active components in charge carrying and storing devices.

Surface-mounted MOF (SURMOF) thin films and 2D sheets can serve as prototypical examples of organized molecular systems for device applications. Ballav et al. prepared a Cu-TCNQ SURMOF on mercaptoundecoanoic acid-functionalized FTO and Au substrates using the layer-by-layer (LbL) method.[145] Electron beam lithography facilitated the fabrication of Cu-TCNQ SURMOF thin film devices with consistent conductivity values in the range of 10^{-5} S cm^{-1}. The SURMOF of Cu-TCNQ also exhibited unique rectifying behavior when exposed to I_2 vapor, while bulk Cu-TCNQ under identical exposure conditions did not. Though not explicitly a SURMOF, Allendorf et al.[89] prepared a $Cu_3(BTC)_2$ thin film on patterned SiO_2/Si wafers and soaked the film in a TCNQ/dichloromethane solution to load the MOF with conductive TCNQ. The conductivity of the loaded film was measured to be as high as 7 S m^{-1}, thereby suggesting that loading 2D molecular materials with functional compounds may likewise be a viable strategy for introducing desirable properties.

1.5.2 Sensing

Two-dimensional MOFs are attractive candidate sensor materials due to their highly exposed pore and surface areas and the inherent sensitivity of their electronic structures to gating through adsorption or binding of analytes. MOF thin film or nearly-2D materials have the potential to detect gases, solvents, metal ions[146,147] and contaminants[40,148] if interaction of these analytes with the framework induces, ideally reversible, optical, electronic, or crystallographic changes. In this regard, the Mirica group has recently demonstrated the broad utility of MOFs as sensors by incorporating assorted 2D frameworks into detection platforms. Their self-organized frameworks on textile (SOFT) devices (**Figure 1.6**),[149] MOF-loaded shrinkable polymer films,[150] and bimetallic 2D MOF device prepared through dropcast[151] are good sensors for NO, H_2S, NH_3, and/or H_2O.

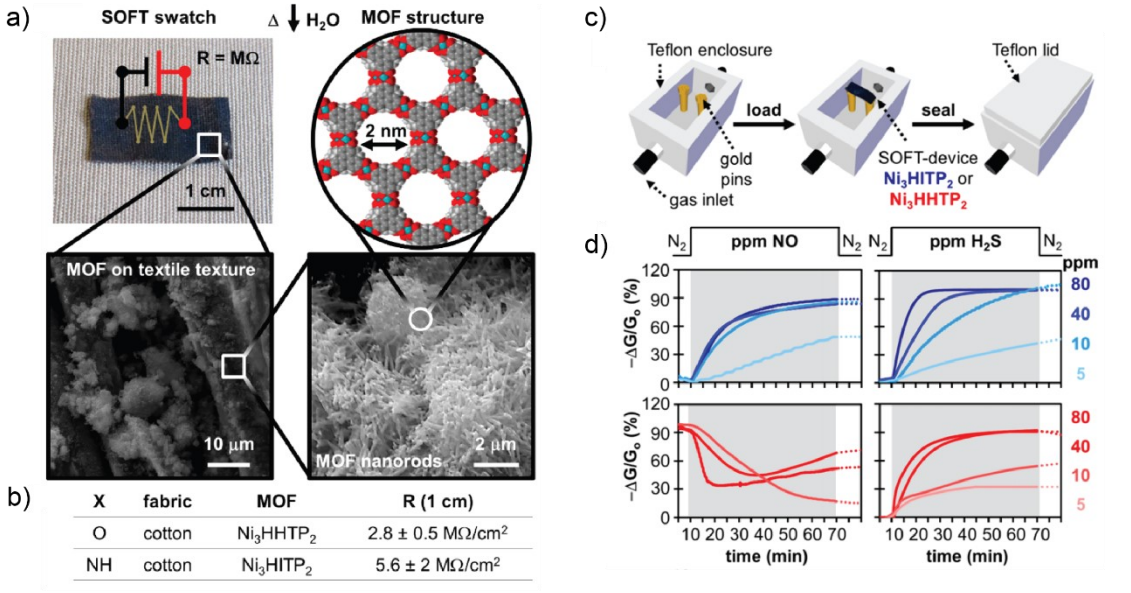

Figure 1.6 | (a) Conductive SOFT-devices produced from solvothermal condensation of MOF reagents in water onto textiles. Photograph of SOFT-device (top left), SEM images of textile fibers coated by MOF film (bottom left), SEM image of characteristic MOF nanorod structure (bottom right), and space-filling model of MOF (top right). (b) Sheet resistance measurements for SOFT-devices. (c) Schematic of custom enclosure for measuring (d) response of SOFT-sensors when exposed to NO (left) or H2S (right). Reprinted (adapted) with permission from *J. Am. Chem. Soc.* **139**, 16759–16767 (2017). Copyright 2017 American Chemical Society.

Focusing on smaller scale materials, Allendorf et al. prepared HKUST-1 thin films on substrates by spin coating a DMSO solution containing $Cu(NO_3)_2 \cdot 3H_2O$ and 1,3,5-benzenetricarboxylic acid in a layer-by-layer manner.[161] Between each layering cycle, the deposited HKUST-1 layer was heated for five minutes at 70 ˚C. As a final step, the MOF was soaked in methanol and activated at 100 ˚C for 30 min to ready the thin film for sensing tests. The purple films were exposed to 0.2–95 % relative humidity (RH) at 296 K and reflectance spectroscopy was used to monitor the thin film response. Exposure to humidity, particularly at lower RH, red shifts the reflectance spectrum and correlates to a color change from purple to light blue in the HKUST-1 thin film. Removal of water through a 5 min dry air purge results in reversion of the MOF thin film to its previous state. In this manner, trends in the percent reflectance of the thin film as a function of RH were assessed. The thin film was even incorporated into a practical LED photodector for low RH testing. Eddaoudi et al. prepared two thin films, NbOFFIVE-1-Ni and ALFFIVE-1-Ni that enabled detection of CO_2 down to 400-5000 ppm.[152] In this work, a novel paste-like MOF deposition method was used to prepare homogenous and uniform thin film coatings of both MOFs on interdigitated electrodes (IDE) and QCMs. The IDE sensing assessment showed a decrease in capacitance of the MOFs during their exposure to various CO_2 concentrations, while QCM data reflected in situ changes in the MOFs' mass due to surface adsorption of CO_2.

Many MOF thin films have been prepared to detect small organic molecules. Dincă et al. dropcasted $Cu_3(HITP)_2$[153] dispersions to prepare an ammonia vapor sensor with sub-ppm detection capabilities. Xu et al.[127] demonstrated a 2–20 nm $Cu_3(HHTP)_2$ thin film grown by spray LbL as an excellent room-temperature, chemiresistive ammonia sensor. The thin film selectively detects ammonia and can reliably report on concentrations as low as 100 ppm. Dincă et al. also identified that pellets of their conductive 2D MOFs can be used as sensors for assorted volatile organic compounds,[39] suggesting that singly crystalline thin films or

nanosheets could be promising sensors. Ethylamine sensing was accomplished by Zn(BDC)(H_2O) MOF nanosheets prepared by Jiang et al.[154] Here, binding of ethylamine by the MOF was monitored through fluorescence spectroscopy.

1.5.3 Gas uptake

The same features that enable MOF thin films to participate in selective molecular separations render them promising candidates as gas storage materials. Carbon dioxide storage has attracted much attention from the MOF community but remains challenging for MOF nanosheets, which lack bulk porosity for adsorption. Moorthy et al.[155] delaminated their bulk imidazole and triptycene-based MOFs into nanosheets by disrupting interlayer hydrogen bonding. CO_2 adsorption capacities as high as 124–209 cc g^{-1} were measured for the bulk MOFs and are better than reported uptake values for N_2 and H_2, but adsorption capacities are not reported for the nanosheets. Do et al.[156] formed nanocube, nanosheet, and nanorod morphologies of their $Cu_2(ndc)_2(dabco)$ MOF by incorporating acetic acid and/or pyridine modulators during synthesis. CO_2 uptake for each morphology was improved relative to the bulk, and measured 5.0, 4.8, 4.3, and 3.5 mmol g^{-1} (at 1 bar and 273 K) for the nanocube, nanosheet, nanorod, and bulk samples, respectively. By modulating crystal growth and repressing certain crystal faces, tailored materials with specific morphologies and facial functionalities can be prepared. Kang and coworkers[157] compared CO_2 working capacities of ZIF-8, ZIF-L, and dia(Zn)-HCOONa (a hexagonal nanosheet). At elevated temperatures between 50-100°C, similar working capacities were observed whereas the latter two systems were considered nonporous at 77 K in N_2 physisorption experiments. The authors suggest increased framework flexibility at higher temperatures likely correlates to increased CO_2 adsorption. Coskun et al. synthesized graphene/ZIF-8 composites[158] and investigated their CO_2 capture at 303 K and at pressures as high as 35 bar. Rao et al.[159] also prepared

graphene/MOF composites with their Cd-PBM MOF. The composites, totaling 2.5–3 nm in thickness, appear to undergo uptake of CO_2 in a stepwise manner with significant hysteresis. In efforts to improve MOF gas adsorption on the nanoscale, Zhang and coworkers demonstrated higher CO_2 uptake by ZIF-L nanosheets supported on halloysite nanotube (HNT) membranes compared to samples without HNT.[160] Careful selection of substrates and solid supports are therefore crucial in continued understanding of nanosheet properties.

1.6 Development of new MOFs for next-generation active device architectures

Our work draws from the vast and diverse field of MOF research to develop a series of new molecular frameworks capable of meeting the two important criteria for implementation into active device architectures. We introduce a molecular species, $Mo_2(INA)_4$ (INA = isonicotinate), which acts as the building unit for the modular assembly of extended frameworks. Through solution-phase and vapor-phase synthetic methods we produce four new architectures (**Table 1.1**).

This molecular building unit can assemble into 1D (**Chapter 2**) and 2D (**Chapter 3**) frameworks through solution-phase crystallization methods. Additionally, we can utilize a single-step CVD reaction to grow directly ultra-thin single crystals of a MOF comprised of $Mo_2(INA)_4$ clusters (**Chapter 4**). These single crystals have exceptionally uniform surfaces, are highly oriented, and can be grown down to the single monolayer level. Alternatively, one can mechanically exfoliate from these crystals individual crystalline layers with thicknesses approaching several nanometers. Our work represents the first effort to prepare singly crystalline MOF thin films from the gas phase. Notably, we discovered unique phase and electronic switching properties in our MOFs by monitoring in situ the response of devices we fabricated from single crystals of this MOF (**Chapter 4**). We foresee expanded use of gas-phase methods, including CVD, for the preparation and fundamental investigation of high-

quality MOF thin films. We also see an exciting opportunity for facile integration of these diverse materials into devices, including sensors, actuators, and detectors.

Table 1.1 | Four unique frameworks derived from $Mo_2(INA)_4$

Framework	Synthetic method	Crystal structure
MF–101	solution-phase (DMF)	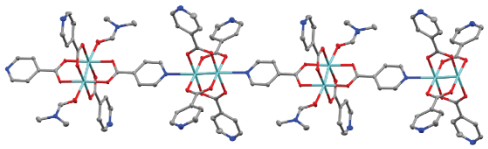
MF–102	solution-phase (DMA)	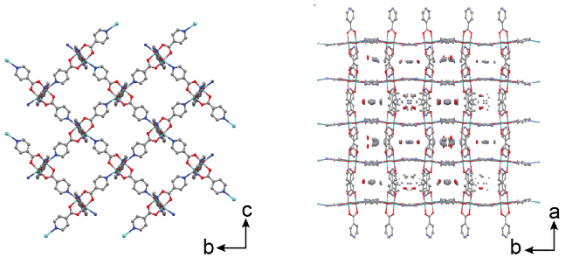
MF–103	solution-phase (DMA + dabco)	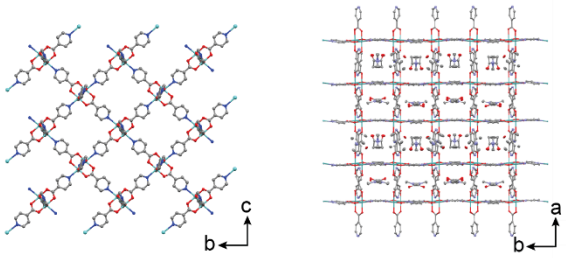
MF–104	vapor-phase	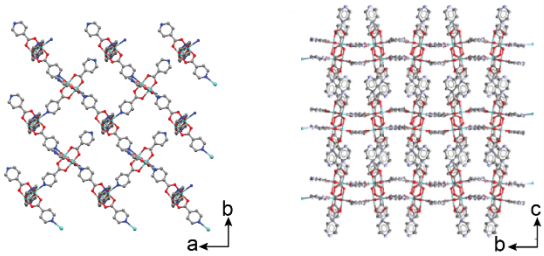

REFERENCES

1. Hendon, C. H., Rieth, A. J., Korzyński, M. D. & Dincă, M. Grand challenges and future opportunities for metal-organic frameworks. *ACS Cent. Sci.* **3**, 554–563 (2017).
2. Knebel, A.; Geppert, B.; Volgmann, D. I.; Stepanov, A. G.; Twiefel, J.; Heitjans, P.; Volkmer,

D.; Caro, J. Defibrillation of soft porous metal-organic frameworks with electric fields. *Science.* **358**, 347–351 (2017).

3. Stavila, V.; Talin, A. A.; Allendorf, M. D. MOF-based electronic and opto-electronic devices. *Chem. Soc. Rev.* **43**, 5994 (2014).
4. Zhou, H.-C.; Kitagawa, S. Metal–Organic Frameworks (MOFs). *Chem. Soc. Rev.* **43**, 5415 (2014).
5. Diercks, C. S.; Yaghi, O. M. The atom, the molecule, and the covalent organic framework. *Science* **355**, 923:1 (2017).
6. Garibay, S. J.; Wang, Z.; Tanabe, K. K.; Cohen, S. M. Postsynthetic Modification: A Versatile Approach Toward Multifunctional Metal-Organic Frameworks. *Inorg. Chem.* **48**, 7341 (2009).
7. Ziebel, M. E.; Darago, L. E.; Long, J. R. Control of Electronic Structure and Conductivity in Two-Dimensional Metal–Semiquinoid Frameworks of Titanium, Vanadium, and Chromium. *J. Am. Chem. Soc.* **140,** 3040 (2018).
8. Xie, L. S.; Sun, L.; Wan, R.; Park, S. S.; DeGayner, J. A.; Hendon, C. H.; Dincă, M. Tunable Mixed-Valence Doping toward Record Electrical Conductivity in a Three-Dimensional Metal–Organic Framework. *J. Am. Chem. Soc.* DOI: 10.1021/jacs.8b03604 (2018).
9. Sumida, K.; Rogow, D. L.; Mason, J. A.; McDonald, T. M.; Bloch, E. D.; Herm, Z. R.; Bae, T.-H.; Long, J. R. Carbon Dioxide Capture in Metal–Organic Frameworks. *Chem. Rev.* **112**, 724 (2012).
10. Hendon, C. H.; Rieth, A. J.; Korzynski, M. D.; Dincă, M. Grand Challenges and Future Opportunities for Metal–Organic Frameworks. *ACS Cent. Sci.* **3**, 554 (2017).
11. Bisbey, R. P.; Dichtel, W. R. Covalent Organic Frameworks as a Platform for Multidimensional Polymerization. *ACS Cent. Sci.* **3**, 533 (2017).
12. Ko, M., Mendecki, L. & Mirica, K. A. Conductive two-dimensional metal-organic

frameworks as multifunctional materials. *Chem. Commun.* **54**, 7873–7891 (2018).

13. Sun, L., Campbell, M. G.; Dincă, M. Electrically conductive porous metal-organic frameworks. *Angew. Chemie Int. Ed.* **55**, 3566–3579 (2016).
14. Medina, D. D., Mähringer, A. & Bein, T. Electroactive metalorganic frameworks. *Isr. J. Chem.* **58**, 1089–1101 (2018).
15. Allendorf, M.D. *et al.* Electronic devices using open framework materials. *Chem. Rev.* **120**, 8581-8640 (2020).
16. Stassen, I. *et al.* An updated roadmap for the integration of metal-organic frameworks with electronic devices and chemical sensors. *Chem. Soc. Rev.* **46**, 3185-3241 (2017).
17. Sato, O. Dynamic molecular crystals with switchable physical properties. *Nat. Chem.* **8**, 644–656 (2016).
18. Solomos, M. A., Claire, F. J. & Kempa, T. J. 2D Molecular Crystal Lattices: Advances in their Synthesis, Characterization, and Application. *J. Mater. Chem. A* **7**, 23537-23562 (2019).
19. Widmer, R. N. *et al.* Pressure promoted low-temperature melting of metal–organic frameworks. *Nat. Mater.* **18**, 370–376 (2019).
20. Sun, L., Park, S. S., Sheberla, D. & Dincă, M. Measuring and reporting electrical conductivity in metal-organic frameworks: Cd_2(TTFTB) as a case study. *J. Am. Chem. Soc.* **138**, 14772–14782 (2016).
21. Evans, A. M. *et al.* Seeded growth of single-crystal two-dimensional covalent organic frameworks. *Science.* **7883**, 1–13 (2018).
22. Colson, J. W. *et al.* Oriented 2D covalent organic framework thin films on single-layer graphene. *Science.* **332**, 228–232 (2011).
23. Kumar, M., Choudhary, M. K. & Rimer, J. D. Transient modes of zeolite surface growth from 3D gel-like islands to 2D single layers. *Nat. Commun.* 1–9 (2018). doi:10.1038/s41467-018-04296-4

24. Li, M. M.; Claire, F. J.; Solomos, M. A.; Tenney, S. M.; Ivanov, S. A.; Siegler, M. A.; Kempa, T. J. Molecular chains of coordinated dimolybdenum isonicotinate paddlewheel clusters. *RSC Adv.* **9**, 16492–16495 (2019).

25. Claire, F. J.; Li, M. M.; Tenney, S. M.; Siegler, M. A.; Wagner, J. S.; Hall, A. S.; Kempa, T J. Hierarchically ordered two-dimensional coordination polymers assembled from redox-active dimolybdenum clusters. *J. Am. Chem. Soc.* **140**, 10673–10676 (2018).

26. Claire, F. J.; Solomos, M. A.; Kim, J.; Wang, G.; Siegler, M. A.; Crommie, M. F.; Kempa, T. J. Structural and electronic switching of a single crystal 2D metal-organic framework prepared by chemical vapor deposition. *Nat. Commun.* **11** (1), 5524 (2020)

27. Tan, C., Cao, X., Wu, X. J., He, Q., Yang, J., Zhang, X., Chen, J., Zhao, W., Han, S., Nam, G. H., Sindoro, M. & Zhang, H. Recent Advances in Ultrathin Two-Dimensional Nanomaterials. *Chem. Rev.* **117**, 6225–6331 (2017).

28. Miró, P., Audiffred, M. & Heine, T. An atlas of two-dimensional materials. *Chem. Soc. Rev.* **43**, 6537–6554 (2014).

29. Duong, D. L., Yun, S. J. & Lee, Y. H. Van der Waals Layered Materials: Opportunities and Challenges. *ACS Nano* **11**, 11803–11830 (2017).

30. Bhimanapati, G. R., Lin, Z., Meunier, V., Jung, Y., Cha, J., Das, S., Xiao, D., Son, Y., Strano, M. S., Cooper, V. R., Liang, L., Louie, S. G., Ringe, E., Zhou, W., Kim, S. S., Naik, R. R., Sumpter, B. G., Terrones, H., Xia, F., *et al.* Recent Advances in Two-Dimensional Materials beyond Graphene. *ACS Nano* **9**, 11509–11539 (2015).

31. Novoselov, K. S., Mishchenko, A., Carvalho, A. & Castro Neto, A. H. 2D materials and van der Waals heterostructures. *Science.* **353**, (2016).

32. Meng, Z., Stolz, R. M., Mendecki, L. & Mirica, K. A. Electrically-transduced chemical sensors based on two-dimensional nanomaterials. *Chem. Rev.* **119**, 478–598 (2019).

33. Mannix, A. J., Kiraly, B., Hersam, M. C. & Guisinger, N. P. Synthesis and chemistry of

elemental 2D materials. *Nat. Rev. Chem.* **1**, 1–15 (2017).

34. Geim, A. K. & Grigorieva, I. V. Van der Waals heterostructures. *Nature* **499**, 419–425 (2013).
35. Huang, N., Wang, P. & Jiang, D. Covalent organic frameworks: A materials platform for structural and functional designs. *Nat. Rev. Mater.* **1**, (2016).
36. Ding, S. Y. & Wang, W. Covalent organic frameworks (COFs): From design to applications. *Chem. Soc. Rev.* **42**, 548–568 (2013).
37. Furukawa, H., Cordova, K. E., O'Keeffe, M. & Yaghi, O. M. The chemistry and applications of metal-organic frameworks. *Science.* **341**, (2013).
38. Li, B., Wen, H. M., Cui, Y., Zhou, W., Qian, G. & Chen, B. Emerging Multifunctional Metal–Organic Framework Materials. *Adv. Mater.* **28**, 8819–8860 (2016).
39. Campbell, M. G., Liu, S. F., Swager, T. M. & Dincă, M. Chemiresistive Sensor Arrays from Conductive 2D Metal-Organic Frameworks. *J. Am. Chem. Soc.* **137**, 13780–13783 (2015).
40. Kitagawa, S., Kitaura, R. & Noro, S. I. Functional porous coordination polymers. *Angew. Chemie - Int. Ed.* **43**, 2334–2375 (2004).
41. Islamoglu, T., Goswami, S., Li, Z., Howarth, A. J., Farha, O. K. & Hupp, J. T. Postsynthetic Tuning of Metal-Organic Frameworks for Targeted Applications. *Acc. Chem. Res.* **50**, 805–813 (2017).
42. Zheng, W., Tsang, C. S., Lee, L. Y. S. & Wong, K. Y. Two-dimensional metal-organic framework and covalent-organic framework: synthesis and their energy-related applications. *Mater. Today Chem.* **12**, 34–60 (2019).
43. Medina, D. D., Sick, T. & Bein, T. Photoactive and Conducting Covalent Organic Frameworks. *Adv. Energy Mater.* **7**, 1–8 (2017).
44. Kreno, L. E., Leong, K., Farha, O. K., Allendorf, M., Van Duyne, R. P. & Hupp, J. T. Metal-organic framework materials as chemical sensors. *Chem. Rev.* **112**, 1105–1125 (2012).

45. Yeo, Z. Y., Chai, S. P., Zhu, P. W. & Mohamed, A. R. An overview: Synthesis of thin films/membranes of metal organic frameworks and its gas separation performances. RSC Adv. 4, 54322–54334 (2014).
46. Fang, X., Zong, B. & Mao, S. Metal–Organic Framework-Based Sensors for Environmental Contaminant Sensing. Nano-Micro Lett. 10, 1–19 (2018).
47. Wang, H., Zeng, Z., Xu, P., Li, L., Zeng, G., Xiao, R., Tang, Z., Huang, D., Tang, L., Lai, C., Jiang, D., Liu, Y., Yi, H., Qin, L., Ye, S., Ren, X. & Tang, W. Recent progress in covalent organic framework thin films: fabrications, applications and perspectives. Chem. Soc. Rev. 48, 488–516 (2019).
48. Peng, Y., Li, Y., Ban, Y., Jin, H., Jiao, W., Liu, Z. & Yang, W. Metal-organic framework nanosheets as building blocks for molecular sieving membranes. Science. 346, 1356–1359 (2014).
49. Lan, G., Li, Z., Veroneau, S. S., Zhu, Y.-Y., Xu, Z., Wang, C. & Lin, W. Photosensitizing Metal–Organic Layers for Efficient Sunlight-Driven Carbon Dioxide Reduction. *J. Am. Chem. Soc.* **140**, 12369–12373 (2018).
50. Schneemann, A., Bon, V., Schwedler, I., Senkovska, I., Kaskel, S. & Fischer, R. A. Flexible metal–organic frameworks. *Chem. Soc. Rev.* **43**, 6062–6096 (2014).
51. Zhao, M., Huang, Y., Peng, Y., Huang, Z., Ma, Q. & Zhang, H. Two-dimensional metal-organic framework nanosheets: Synthesis and applications. *Chem. Soc. Rev.* **47**, 6267–6295 (2018).
52. Li, S., Yang, K., Tan, C., Huang, X., Huang, W. & Zhang, H. Preparation and applications of novel composites composed of metal-organic frameworks and two-dimensional materials. *Chem. Commun.* **52**, 1555–1562 (2016).
53. Ashworth, D. J. & Foster, J. A. Metal-organic framework nanosheets (MONs): A new dimension in materials chemistry. *J. Mater. Chem. A* **6**, 16292–16307 (2018).

54. Das, G., Biswal, B. P., Kandambeth, S., Venkatesh, V., Kaur, G., Addicoat, M., Heine, T., Verma, S. & Banerjee, R. Chemical sensing in two dimensional porous covalent organic nanosheets. *Chem. Sci.* **6**, 3931–3939 (2015).

55. Liu, J., Yu, H., Wang, L., Deng, Z., Naveed, K. ur R., Nazir, A. & Haq, F. Two-dimensional metal-organic frameworks nanosheets: Synthesis strategies and applications. *Inorganica Chim. Acta* **483**, 550–564 (2018).

56. Liu, W., Yin, R., Xu, X., Zhang, L., Shi, W. & Cao, X. Structural Engineering of Low-Dimensional Metal-Organic Frameworks: Synthesis, Properties, and Applications. *Adv. Sci.* 1802373 (2019).

57. Kambe, T., Sakamoto, R., Hoshiko, K., Takada, K., Miyachi, M., Ryu, J. H., Sasaki, S., Kim, J., Nakazato, K., Takata, M. & Nishihara, H. π-Conjugated nickel bis(dithiolene) complex nanosheet. *J. Am. Chem. Soc.* **135**, 2462–2465 (2013).

58. Sakamoto, R., Takada, K., Pal, T., Maeda, H., Kambe, T. & Nishihara, H. Coordination nanosheets (CONASHs): strategies, structures and functions. *Chem. Commun.* **53**, 5781–5801 (2017).

59. Stassen, I., De Vos, D. & Ameloot, R. Vapor-Phase Deposition and Modification of Metal–Organic Frameworks: State-of-the-Art and Future Directions. *Chem. - A Eur. J.* **22**, 14452–14460 (2016).

60. Cliffe, M. J., Castillo-Martínez, E., Wu, Y., Lee, J., Forse, A. C., Firth, F. C. N., Moghadam, P. Z., Fairen-Jimenez, D., Gaultois, M. W., Hill, J. A., Magdysyuk, O. V, Slater, B., Goodwin, A. L. & Grey, C. P. Metal-Organic Nanosheets Formed via Defect-Mediated Transformation of a Hafnium Metal-Organic Framework. *J. Am. Chem. Soc.* **139**, 5397–5404 (2017).

61. Allendorf, M. D., Schwartzberg, A., Stavila, V. & Talin, A. A. A roadmap to implementing metal-organic frameworks in electronic devices: Challenges and critical directions. *Chem. - A Eur. J.* **17**, 11372–11388 (2011).

62. Liu, J. & Wöll, C. Surface-supported metal-organic framework thin films: Fabrication methods, applications, and challenges. *Chem. Soc. Rev.* **46**, 5730–5770 (2017).

63. Ko, M., Mendecki, L. & Mirica, K. A. Conductive two-dimensional metal-organic frameworks as multifunctional materials. *Chem. Commun.* **54**, 7873–7891 (2018).

64. Heinke, L. & Wöll, C. Surface-Mounted Metal–Organic Frameworks: Crystalline and Porous Molecular Assemblies for Fundamental Insights and Advanced Applications. *Adv. Mater.* **1806324**, (2019).

65. Lischka, M., Dong, R., Wang, M., Martsinovich, N., Fritton, M., Grossmann, L., Heckl, W. M., Feng, X. & Lackinger, M. Competitive Metal Coordination of Hexaaminotriphenylene on Cu(111) by Intrinsic Copper Versus Extrinsic Nickel Adatoms. *Chem. - A Eur. J.* **25**, 1975–1983 (2019).

66. Benmansour, S., Abhervé, A., Gómez-Claramunt, P., Vallés-García, C. & Gómez-García, C. J. Nanosheets of Two-Dimensional Magnetic and Conducting Fe(II)/Fe(III) Mixed-Valence Metal-Organic Frameworks. *ACS Appl. Mater. Interfaces* **9**, 26210–26218 (2017).

67. Liao, W. M., Zhang, J. H., Yin, S. Y., Lin, H., Zhang, X., Wang, J., Wang, H. P., Wu, K., Wang, Z., Fan, Y. N., Pan, M. & Su, C. Y. Tailoring exciton and excimer emission in an exfoliated ultrathin 2D metal-organic framework. *Nat. Commun.* **9**, (2018).

68. Luo, Y. H., Chen, C., He, C., Zhu, Y. Y., Hong, D. L., He, X. T., An, P. J., Wu, H. S. & Sun, B. W. Single-Layered Two-Dimensional Metal-Organic Framework Nanosheets as an in Situ Visual Test Paper for Solvents. *ACS Appl. Mater. Interfaces* **10**, 28860–28867 (2018).

69. Ding, Y., Chen, Y. P., Zhang, X., Chen, L., Dong, Z., Jiang, H. L., Xu, H. & Zhou, H. C. Controlled Intercalation and Chemical Exfoliation of Layered Metal-Organic Frameworks Using a Chemically Labile Intercalating Agent. *J. Am. Chem. Soc.* **139**, 9136–9139 (2017).

70. 49. Huang, J., Li, Y., Huang, R. K., He, C. T., Gong, L., Hu, Q., Wang, L., Xu, Y. T., Tian, X. Y., Liu, S. Y., Ye, Z. M., Wang, F., Zhou, D. D., Zhang, W. X. & Zhang, J. P. Electrochemical Exfoliation

of Pillared-Layer Metal–Organic Framework to Boost the Oxygen Evolution Reaction. *Angew. Chemie - Int. Ed.* **57**, 4632–4636 (2018).

71. Kutzscher, C., Gelbert, A., Ehrling, S., Schenk, C., Senkovska, I. & Kaskel, S. Amine assisted top-down delamination of the two-dimensional metal-organic framework $Cu_2(bdc)_2$. *Dalt. Trans.* **46**, 16480–16484 (2017).
72. Ashworth, D. J., Cooper, A., Trueman, M., Al-Saedi, R. W. M., Smith, L. D., Meijer, A. J. H. M. & Foster, J. A. Ultrasonic Exfoliation of Hydrophobic and Hydrophilic Metal–Organic Frameworks To Form Nanosheets. *Chem. - A Eur. J.* **24**, 17986–17996 (2018).
73. Yuan, K., Song, T., Zhu, X., Li, B., Han, B., Zheng, L., Li, J., Zhang, X. & Hu, W. Construction of Large-Area Ultrathin Conductive Metal–Organic Framework Films through Vapor-Induced Conversion. *Small* **15**, 1–6 (2019).
74. Shete, M., Kumar, P., Bachman, J. E., Ma, X., Smith, Z. P., Xu, W., Mkhoyan, K. A., Long, J. R. & Tsapatsis, M. On the direct synthesis of Cu(BDC) MOF nanosheets and their performance in mixed matrix membranes. *J. Memb. Sci.* **549**, 312–320 (2018).
75. Huang, X., Sheng, P., Tu, Z., Zhang, F., Wang, J., Geng, H., Zou, Y., Di, C. A., Yi, Y., Sun, Y., Xu, W. & Zhu, D. A two-dimensional π-d conjugated coordination polymer with extremely high electrical conductivity and ambipolar transport behaviour. *Nat. Commun.* **6**, 1–8 (2015).
76. Rodenas, T., Luz, I., Prieto, G., Seoane, B., Miro, H., Corma, A., Kapteijn, F., Llabrés I Xamena, F. X. & Gascon, J. Metal-organic framework nanosheets in polymer composite materials for gas separation. *Nat. Mater.* **14**, 48–55 (2015).
77. Chen, I.-F., Lu, C.-F. & Su, W.-F. Highly Conductive 2D Metal–Organic Framework Thin Film Fabricated by Liquid–Liquid Interfacial Reaction Using One-Pot-Synthesized Benzenehexathiol. *Langmuir* **34**, (2018)
78. Zhao, M., Wang, Y., Ma, Q., Huang, Y., Zhang, X., Ping, J., Zhang, Z., Lu, Q., Yu, Y., Xu, H., Zhao,

Y. & Zhang, H. Ultrathin 2D Metal-Organic Framework Nanosheets. *Adv. Mater.* **27**, 7372–7378 (2015).

79. Xue, F., Kumar, P., Xu, W., Mkhoyan, K. A. & Tsapatsis, M. Direct Synthesis of 7 nm-Thick Zinc(II)-Benzimidazole-Acetate Metal-Organic Framework Nanosheets. *Chem. Mater.* **30**, 69–73 (2018).
80. Xu, G., Yamada, T., Otsubo, K., Sakaida, S. & Kitagawa, H. Facile 'modular assembly' for fast construction of a highly oriented crystalline MOF nanofilm. *J. Am. Chem. Soc.* **134**, 16524–16527 (2012).
81. Rubio-Giménez, V., Tatay, S., Volatron, F., Martínez-Casado, F. J., Martí-Gastaldo, C. & Coronado, E. High-Quality Metal-Organic Framework Ultrathin Films for Electronically Active Interfaces. *J. Am. Chem. Soc.* **138**, 2576–2584 (2016).
82. Zhuang, J. L., Terfort, A. & Wöll, C. Formation of oriented and patterned films of metal-organic frameworks by liquid phase epitaxy: A review. *Coord. Chem. Rev.* **307**, 391–424 (2016).
83. Haraguchi, T., Otsubo, K. & Kitagawa, H. Emergence of Surface- and Interface-Induced Structures and Properties in Metal–Organic Framework Thin Films. *Eur. J. Inorg. Chem.* **2018**, 1697–1706 (2018).
84. Guo, W., Zha, M., Wang, Z., Redel, E., Xu, Z. & Wöll, C. Improving the Loading Capacity of Metal-Organic Framework Thin Films Using Optimized Linkers. *ACS Appl. Mater. Interfaces* **8**, 24699–24702 (2016).
85. Liu, J., Wächter, T., Irmler, A., Weidler, P. G., Gliemann, H., Pauly, F., Mugnaini, V., Zharnikov, M. & Wöll, C. Electric transport properties of surface-anchored metal-organic frameworks and the effect of ferrocene loading. *ACS Appl. Mater. Interfaces* **7**, 9824–9830 (2015).
86. Liu, J., Paradinas, M., Heinke, L., Buck, M., Ocal, C., Mugnaini, V. & Wöll, C. Film Quality and

Electronic Properties of a Surface-Anchored Metal-Organic Framework Revealed by using a Multi-technique Approach. *ChemElectroChem* **3**, 713–718 (2016).

87. Van Gough, D., Lambert, T. N., Wheeler, D. R., Rodriguez, M. A., Brumbach, M. T., Allendorf, M. D. & Spoerke, E. D. Controlled nucleation and growth of pillared paddlewheel framework nanostacks onto chemically modified surfaces. *ACS Appl. Mater. Interfaces* **6**, 1509–1514 (2014).
88. Stavila, V., Volponi, J., Katzenmeyer, A. M., Dixon, M. C. & Allendorf, M. D. Kinetics and mechanism of metal–organic framework thin film growth: systematic investigation of HKUST-1 deposition on QCM electrodes. *Chem. Sci.* **3**, 1531 (2012).
89. Talin, A. A., Centrone, A., Ford, A. C., Foster, M. E., Stavila, V., Haney, P., Kinney, R. A., Szalai, V., Gabaly, F. El, Yoon, H. P., Léonard, F. & Allendorf, M. D. Tunable Electrical Conductivity in Metal-Organic Framework Thin-Film Devices. *Science.* **343**, 66–70 (2014).
90. Wannapaiboon, S., Sumida, K., Dilchert, K., Tu, M., Kitagawa, S., Furukawa, S. & Fischer, R. A. Enhanced properties of metal-organic framework thin films fabricated: Via a coordination modulation-controlled layer-by-layer process. *J. Mater. Chem. A* **5**, 13665–13673 (2017).
91. Stoddart, J. F., Gong, X., Wang, G., Cheng, C., Kung, C.-W., Facchetti, A., Han, J.-M., Sue, A. C.-H., Marks, T. J., Liu, Z., Cai, K., Farha, O. K., Botros, Y. Y., Shi, Y., Li, P., Chen, H., Guo, Q.-H. & Shen, D. Epitaxial Growth of γ-Cyclodextrin-Containing Metal–Organic Frameworks Based on a Host–Guest Strategy. *J. Am. Chem. Soc.* **140**, 11402–11407 (2018).
92. Lu, G., Farha, O. K., Zhang, W., Huo, F. & Hupp, J. T. Engineering ZIF-8 thin films for hybrid MOF-based devices. *Adv. Mater.* **24**, 3970–3974 (2012).
93. Serp, P., Kalck, P. & Feurer, R. Chemical vapor deposition methods for the controlled preparation of supported catalytic materials. *Chem. Rev.* **102**, 3085–3128 (2002).
94. Cai, Z., Liu, B., Zou, X. & Cheng, H. Chemical Vapor Deposition Growth and Applications of

Two- Dimensional Materials and Their Heterostructures. *Chem. Rev.* **118**, 6091–6133 (2018).

95. Lemaire, P. C., Zhao, J., Williams, P. S., Walls, H. J., Shepherd, S. D., Losego, M. D., Peterson, G. W. & Parsons, G. N. Copper Benzenetricarboxylate Metal-Organic Framework Nucleation Mechanisms on Metal Oxide Powders and Thin Films formed by Atomic Layer Deposition. *ACS Appl. Mater. Interfaces* **8**, 9514–9522 (2016).
96. Ahvenniemi, E. & Karppinen, M. Atomic/molecular layer deposition: A direct gas-phase route to crystalline metal-organic framework thin films. *Chem. Commun.* **52**, 1139–1142 (2016).
97. Ahvenniemi, E. & Karppinen, M. In Situ Atomic/Molecular Layer-by-Layer Deposition of Inorganic-Organic Coordination Network Thin Films from Gaseous Precursors. *Chem. Mater.* **28**, 6260–6265 (2016).
98. Ahvenniemi, E. & Karppinen, M. ALD/MLD processes for Mn and Co based hybrid thin films. *Dalt. Trans.* **45**, 10730 (2016).
99. Salmi, L. D., Heikkilä, M. J., Puukilainen, E., Sajavaara, T., Grosso, D. & Ritala, M. Studies on atomic layer deposition of MOF-5 thin films. *Microporous Mesoporous Mater.* **182**, 147–154 (2013).
100. Stassen, I., Campagnol, N., Fransaer, J., Vereecken, P., De Vos, D. & Ameloot, R. Solvent-free synthesis of supported ZIF-8 films and patterns through transformation of deposited zinc oxide precursors. *CrystEngComm* **15**, 9308–9311 (2013).
101. Stassen, I., Styles, M., Grenci, G., Van Gorp, H., Vanderlinden, W., De Feyter, S., Falcaro, P., De Vos, D., Vereecken, P. & Ameloot, R. Chemical vapour deposition of zeolitic imidazolate framework thin films. *Nat. Mater.* **15**, 304–310 (2016).
102. Au, V. K.-M., Nakayashiki, K., Huang, H., Suginome, S., Sato, H. & Aida, T. Stepwise Expansion of Layered Metal–Organic Frameworks for Nonstochastic Exfoliation into

Porous Nanosheets. *J. Am. Chem. Soc.* **141**, (2018).

103. Wang, Z., Liu, J., Lukose, B., Gu, Z., Weidler, P. G., Gliemann, H., Heine, T. & Wöll, C. Nanoporous designer solids with huge lattice constant gradients: Multiheteroepitaxy of metal-organic frameworks. *Nano Lett.* **14**, 1526–1529 (2014).

104. 102. Stassen, I., Styles, M., Van Assche, T., Campagnol, N., Fransaer, J., Denayer, J., Tan, J. C., Falcaro, P., De Vos, D. & Ameloot, R. Electrochemical film deposition of the zirconium metal-organic framework UiO-66 and application in a miniaturized sorbent trap. *Chem. Mater.* **27**, 1801–1807 (2015).

105. 103. Colson, J. W., Woll, A. R., Mukherjee, A., Levendorf, M. P., Spitler, E. L., Shields, V. B., Spencer, M. G., Park, J. & Dichtel, W. R. Oriented 2D Covalent Organic Framework Thin Films on Single-Layer Graphene. *Science.* **332**, 228–232 (2011).

106. 104. Sheets, F. Highly Crystalline Nanofilm by Layering of Porphyrin MetalÀOrganic. *J. Am. Chem. Soc.* **2**, 5640–5643 (2011).

107. Ayala, A., Tarver, J. D., Hurst, K. E., Brown, C. M., Parilla, P. A., Gennett, T., Jiang, H. Z. H., Kapelewski, M. T., Long, J. R., Runčevski, T. & FitzGerald, S. A. Record High Hydrogen Storage Capacity in the Metal–Organic Framework Ni 2 (m -dobdc) at Near-Ambient Temperatures . *Chem. Mater.* **30**, 8179–8189 (2018).

108. Zhao, Y., Jiang, L., Shangguan, L., Mi, L., Liu, A. & Liu, S. Synthesis of porphyrin-based two-dimensional metal-organic framework nanodisk with small size and few layers. *J. Mater. Chem. A* **6**, 2828–2833 (2018).

109. Pfeffermann, M., Dong, R., Graf, R., Zajaczkowski, W., Gorelik, T., Pisula, W., Narita, A., Müllen, K. & Feng, X. Free-Standing Monolayer Two-Dimensional Supramolecular Organic Framework with Good Internal Order. *J. Am. Chem. Soc.* **137**, 14525–14532 (2015).

110. Chandra, S., Kandambeth, S., Biswal, B. P., Lukose, B., Kunjir, S. M., Chaudhary, M., Babarao, R., Heine, T. & Banerjee, R. Chemically stable multilayered covalent organic

nanosheets from covalent organic frameworks via mechanical delamination. *J. Am. Chem. Soc.* **135**, 17853–17861 (2013).

111. Berlanga, I., Ruiz-González, M. L., González-Calbet, J. M., Fierro, J. L. G., Mas-Ballesté, R. & Zamora, F. Delamination of layered covalent organic frameworks. *Small* **7**, 1207–1211 (2011).

112. Medina, D. D., Werner, V., Auras, F., Tautz, R., Dogru, M., Schuster, J., Linke, S., Döblinger, M., Feldmann, J., Knochel, P. & Bein, T. Oriented thin films of a benzodithiophene covalent organic framework. *ACS Nano* **8**, 4042–4052 (2014).

113. Li, G., Zhang, K. & Tsuru, T. Two-Dimensional Covalent Organic Framework (COF) Membranes Fabricated via the Assembly of Exfoliated COF Nanosheets. *ACS Appl. Mater. Interfaces* **9**, 8433–8436 (2017).

114. Hoppe, B., Hindricks, K. D. J., Warwas, D. P., Schulze, H. A., Mohmeyer, A., Pinkvos, T. J., Zailskas, S., Krey, M. R., Belke, C., König, S., Fröba, M., Haug, R. J. & Behrens, P. Graphene-like metal-organic frameworks: Morphology control, optimization of thin film electrical conductivity and fast sensing applications. *CrystEngComm* **20**, 6458–6471 (2018).

115. Zhao, S., Wang, Y., Dong, J., He, C. T., Yin, H., An, P., Zhao, K., Zhang, X., Gao, C., Zhang, L., Lv, J., Wang, J., Zhang, J., Khattak, A. M., Khan, N. A., Wei, Z., Zhang, J., Liu, S., Zhao, H., *et al.* Ultrathin metal-organic framework nanosheets for electrocatalytic oxygen evolution. *Nat. Energy* **1**, 1–10 (2016).

116. Lahiri, N., Lotfizadeh, N., Tsuchikawa, R., Deshpande, V. V & Louie, J. Hexaaminobenzene as a building block for a family of 2D coordination polymers. *J. Am. Chem. Soc.* **139**, 19–22 (2017).

117. Kumar, S., Lee, J. A., Maheshwari, S., Mittal, A., Sung, C., Cococcioni, M., Francis, L. F., Mccormick, A. V, Mkhoyan, K. A. & Tsapatsis, M. Dispersible Exfoliated Zeolite Nanosheets and Their Application as a Selective Membrane. *Science.* **734**, 72–76 (2011).

118. Garai, B., Mallick, A., Das, A., Mukherjee, R. & Banerjee, R. Self-Exfoliated Metal-Organic Nanosheets through Hydrolytic Unfolding of Metal-Organic Polyhedra. *Chem. - A Eur. J.* **23**, 7361–7366 (2017).

119. Berlanga, I., Ruiz-González, M. L., González-Calbet, J. M., Fierro, J. L. G., Mas-Ballesté, R. & Zamora, F. Delamination of layered covalent organic frameworks. *Small* **7**, 1207–1211 (2011).

120. Zhan, G. & Zeng, H. C. Synthesis and Functionalization of Oriented Metal – Organic-Framework Nanosheets : Toward a Series of 2D Catalysts. *Adv. Funct. Mater.* **26**, 3268–3281 (2016).

121. He, T., Ni, B., Zhang, S., Gong, Y., Wang, H., Gu, L. & Zhuang, J. Ultrathin 2D Zirconium Metal – Organic Framework Nanosheets : Preparation and Application in Photocatalysis. *Small* **14**, 1–6 (2018).

122. Dmitriev, A., Spillmann, H., Lin, N., Barth, J. V. & Kern, K. Modular assembly of two-dimensional metal-organic coordination networks at a metal surface. *Angew. Chemie - Int. Ed.* **42**, 2670–2673 (2003).

123. Amo-Ochoa, P., Welte, L., González-Prieto, R., Sanz Miguel, P. J., Gómez-García, C. J., Mateo-Martí, E., Delgado, S., Gómez-Herrero, J. & Zamora, F. Single layers of a multifunctional laminar Cu(i,ii) coordination polymer. *Chem. Commun.* **46**, 3262–3264 (2010).

124. Xu, L., Zhou, X., Tian, W. Q., Gao, T., Zhang, Y. F., Lei, S. & Liu, Z. F. Surface-confined single-layer covalent organic framework on single-layer graphene grown on copper foil. *Angew. Chemie - Int. Ed.* **53**, 9564–9568 (2014).

125. Chen, C., Joshi, T., Li, H., Chavez, A. D., Pedramrazi, Z., Liu, P. N., Li, H., Dichtel, W. R., Bredas, J. L. & Crommie, M. F. Local Electronic Structure of a Single-Layer Porphyrin-Containing Covalent Organic Framework. *ACS Nano* **12**, 385–391 (2018).

126. Kung, C. W., Otake, K., Buru, C. T., Goswami, S., Cui, Y., Hupp, J. T., Spokoyny, A. M. & Farha, O. K. Increased Electrical Conductivity in a Mesoporous Metal-Organic Framework Featuring Metallacarboranes Guests. *J. Am. Chem. Soc.* **140**, 3871–3875 (2018).

127. Yao, M. S., Lv, X. J., Fu, Z. H., Li, W. H., Deng, W. H., Wu, G. D. & Xu, G. Layer-by-Layer Assembled Conductive Metal–Organic Framework Nanofilms for Room-Temperature Chemiresistive Sensing. *Angew. Chemie - Int. Ed.* **56**, 16510–16514 (2017).

128. Kambe, T., Sakamoto, R., Kusamoto, T., Pal, T., Fukui, N., Hoshiko, K., Shimojima, T., Wang, Z., Hirahara, T., Ishizaka, K., Hasegawa, S., Liu, F. & Nishihara, H. Redox control and high conductivity of nickel bis(dithiolene) complex π-nanosheet: A potential organic two-dimensional topological insulator. *J. Am. Chem. Soc.* **136**, 14357–14360 (2014).

129. Wu, Y., Moorhouse, S. J. & O'Hare, D. Time-Resolved in Situ Diffraction Reveals a Solid-State Rearrangement during Solvothermal MOF Synthesis. *Chem. Mater.* **27**, 7236–7239 (2015).

130. Cravillon, J., Schrçder, C. A., Nayuk, R., Gummel, J., Huber, K. & Wiebcke, M. Fast Nucleation and Growth of ZIF-8 Nanocrystals Monitored by Time-. 8067–8071 (2011).

131. Biener, M. M., Biener, J., Schalek, R. & Friend, C. M. Growth of nanocrystalline on Au (111) studied by in situ scanning tunneling microscopy tunneling microscopy. *J. Chem. Phys.* **121**, 12010–12016 (2004).

132. Dave, S. H., Gong, C., Robertson, A. W., Warner, J. H. & Grossman, C. Chemistry and Structure of Graphene Oxide via Direct Imaging. *ACS Nano* **10**, 7515–7522 (2016).

133. Mandemaker, L. D. B., Filez, M., Delen, G., Tan, H., Zhang, X., Lohse, D. & Weckhuysen, B. M. Time-Resolved in Situ Liquid-Phase Atomic Force Microscopy and Infrared Nanospectroscopy during the Formation of Metal-Organic Framework Thin Films. *J. Phys. Chem. Lett.* **9**, 1838–1844 (2018).

134. Zhao, J., Kalanyan, B., Barton, H. F., Sperling, B. A., Parsons, G. N., Carolina, N. & States,

U. In Situ Time-Resolved Attenuated Total Re fl ectance Infrared Spectroscopy for Probing Metal – Organic Framework Thin Film Growth. *Chem. Mater.* **29**, 8804–8810 (2017).

135. Xia, W., Mahmood, A., Zou, R. & Xu, Q. Metal-organic frameworks and their derived nanostructures for electrochemical energy storage and conversion. *Energy Environ. Sci.* **8**, 1837–1866 (2015).

136. Park, J. G., Aubrey, M. L., Oktawiec, J., Chakarawet, K., Darago, L. E., Grandjean, F., Long, G. J. & Long, J. R. Charge Delocalization and Bulk Electronic Conductivity in the Mixed-Valence Metal-Organic Framework Fe(1,2,3-triazolate)2(BF4)x. *J. Am. Chem. Soc.* **140**, 8526–8534 (2018).

137. Silva, P., Vilela, S. M. F., Tomé, J. P. C. & Almeida Paz, F. A. Multifunctional metal–organic frameworks: from academia to industrial applications. *Chem. Soc. Rev.* **44**, 6774–6803 (2015).

138. Feng, D., Lei, T., Lukatskaya, M. R., Park, J., Huang, Z., Lee, M., Shaw, L., Chen, S., Yakovenko, A. A., Kulkarni, A., Xiao, J., Fredrickson, K., Tok, J. B., Zou, X., Cui, Y. & Bao, Z. Robust and conductive two-dimensional metal-organic frameworks with exceptionally high volumetric and areal capacitance. *Nat. Energy* **3**, 30–36 (2018).

139. Xie, L. S., Sun, L., Wan, R., Park, S. S., DeGayner, J. A., Hendon, C. H., Dincă, M., Dincă, M., DeGayner, J. A., Hendon, C. H., Wan, R., Park, S. S. & Xie, L. S. Tunable Mixed-Valence Doping toward Record Electrical Conductivity in a Three-Dimensional Metal-Organic Framework. *J. Am. Chem. Soc.* **140**, 7411–7414 (2018).

140. Clough, A. J., Skelton, J. M., Downes, C. A., De La Rosa, A. A., Yoo, J. W., Walsh, A., Melot, B. C. & Marinescu, S. C. Metallic Conductivity in a Two-Dimensional Cobalt Dithiolene Metal-Organic Framework. *J. Am. Chem. Soc.* **139**, 10863–10867 (2017).

141. Blood-Forsythe, M. A., Wade, C. R., Aspuru-Guzik, A., Dincă, M., Brozek, C. K., Sheberla, D., Sun, L. & Er, S. High Electrical Conductivity in Ni_3 (2,3,6,7,10,11-

hexaiminotriphenylene)$_2$, a Semiconducting Metal–Organic Graphene Analogue . *J. Am. Chem. Soc.* **136**, 8859–8862 (2014).

142. Chandra, S., Roy Chowdhury, D., Addicoat, M., Heine, T., Paul, A. & Banerjee, R. Molecular Level Control of the Capacitance of Two-Dimensional Covalent Organic Frameworks: Role of Hydrogen Bonding in Energy Storage Materials. *Chem. Mater.* **29**, 2074–2080 (2017).

143. Dong, R., Han, P., Arora, H., Ballabio, M., Karakus, M., Zhang, Z., Shekhar, C., Adler, P., Petkov, P. S., Erbe, A., Mannsfeld, S. C. B., Felser, C., Heine, T., Bonn, M., Feng, X. & Cánovas, E. High-mobility band-like charge transport in a semiconducting two-dimensional metal–organic framework. *Nat. Mater.* **17**, 1027–1032 (2018).

144. Sheberla, D., Bachman, J. C., Elias, J. S., Sun, C. J., Shao-Horn, Y. & Dincă, M. Conductive MOF electrodes for stable supercapacitors with high areal capacitance. *Nat. Mater.* **16**, 220–224 (2017).

145. Rana, S., Rajendra, R., Dhara, B. & Jha, P. K. Highly Hydrophobic and Chemically Rectifiable Surface- Anchored Metal-Organic Framework Thin-Film Devices. 1–8 (2016).

146. Han, L. J., Zheng, D., Chen, S. G., Zheng, H. G. & Ma, J. A Highly Solvent-Stable Metal–Organic Framework Nanosheet: Morphology Control, Exfoliation, and Luminescent Property. *Small* **14**, 1–7 (2018).

147. 157. Xu, H., Gao, J., Qian, X., Wang, J., He, H., Cui, Y., Yang, Y., Wang, Z. & Qian, G. Metal-organic framework nanosheets for fast-response and highly sensitive luminescent sensing of Fe^{3+}. *J. Mater. Chem. A* **4**, 10900–10905 (2016).

148. Campbell, M. G. & Dincă, M. Metal–organic frameworks as active materials in electronic sensor devices. *Sensors (Switzerland)* **17**, 1–11 (2017).

149. Smith, M. K. & Mirica, K. A. Self-Organized Frameworks on Textiles (SOFT): Conductive Fabrics for Simultaneous Sensing, Capture, and Filtration of Gases. *J. Am.*

Chem. Soc. **139**, 16759–16767 (2017).

150. Smith, M. K., Jensen, K. E., Pivak, P. A. & Mirica, K. A. Direct Self-Assembly of Conductive Nanorods of Metal-Organic Frameworks into Chemiresistive Devices on Shrinkable Polymer Films. *Chem. Mater.* **28**, 5264–5268 (2016).

151. Meng, Z., Aykanat, A. & Mirica, K. A. Welding Metallophthalocyanines into Bimetallic Molecular Meshes for Ultrasensitive, Low-Power Chemiresistive Detection of Gases. *J. Am. Chem. Soc.* **141**, 2046–2053 (2018).

152. Tchalala, M. R., Belmabkhout, Y., Adil, K., Chappanda, K. N., Cadiau, A., Bhatt, P. M., Salama, K. N. & Eddaoudi, M. Concurrent Sensing of CO2 and H2O from Air Using Ultramicroporous Fluorinated Metal-Organic Frameworks: Effect of Transduction Mechanism on the Sensing Performance. *ACS Appl. Mater. Interfaces* **11**, 1706–1712 (2019).

153. Campbell, M. G., Sheberla, D., Liu, S. F., Swager, T. M. & Dincă, M. Cu3(hexaiminotriphenylene)2: An electrically conductive 2D metal-organic framework for chemiresistive sensing. *Angew. Chemie - Int. Ed.* **54**, 4349–4352 (2015).

154. Li, Z., Qiu, L., Wang, W., Xu, T., Wu, Y. & Jiang, X. Fabrication of nanosheets of a fluorescent metal – organic framework [Zn(BDC)(H_2O)]n(BDC = 1,4-benzenedicarboxylate): Ultrasonic synthesis and sensing of ethylamine. *Inorg. Chem. Commun.* **11**, 1375–1377 (2008).

155. Chandrasekhar, P., Mukhopadhyay, A., Savitha, G. & Moorthy, J. N. Orthogonal self-assembly of a trigonal triptycene triacid: signaling of exfoliation of porous 2D metal-organic layers by fluorescence and selective CO_2 capture by the hydrogen-bonded MOF. *J. Mater. Chem. A* **5**, 5402–5412 (2017).

156. Pham, M. H., Vuong, G. T., Fontaine, F. G. & Do, T. O. Rational synthesis of metal-organic framework nanocubes and nanosheets using selective modulators and their morphology-

dependent gas-sorption properties. *Cryst. Growth Des.* **12**, 3091–3095 (2012).

157. Lo, Y., Lam, C. H., Chang, C. W., Yang, A. C. & Kang, D. Y. Polymorphism/pseudopolymorphism of metal-organic frameworks composed of zinc(II) and 2-methylimidazole: Synthesis, stability, and application in gas storage. *RSC Adv.* **6**, 89148–89156 (2016).

158. Kim, D., Kim, D. W., Hong, W. G. & Coskun, A. Graphene/ZIF-8 composites with tunable hierarchical porosity and electrical conductivity. *J. Mater. Chem. A* **4**, 7710–7717 (2016).

159. Kumar, R., Jayaramulu, K., Maji, T. K. & Rao, C. N. R. Growth of 2D sheets of a MOF on graphene surfaces to yield composites with novel gas adsorption characteristics. *Dalt. Trans.* **43**, 7383–7386 (2014).

160. Li, H., Hou, J., Bennett, T. D., Liu, J. & Zhang, Y. Templated growth of vertically aligned 2D metal-organic framework nanosheets. *J. Mater. Chem. A* **7**, 5811–5818 (2019).

CHAPTER TWO

Dimolybdenum isonicotinate paddlewheel cluster as a molecular building unit for metal–organic frameworks

---

This work was co-authored with the following authors and is published under the following citation:

F. James Claire,[a] Minyuan M. Li,[a,b] Marina A. Solomos,[a] Stephanie M. Tenney,[a,c] Sergei A. Ivanov,[b] Maxime A. Siegler,[a] and Thomas J. Kempa*[a,d]

a. Department of Chemistry, Johns Hopkins University, Baltimore, MD 21218, USA

b. Center for Integrated Nanotechnologies, Los Alamos National Laboratory, Albuquerque, NM 87185, USA

c. Department of Chemistry and Biochemistry, University of California, Los Angeles, Los Angeles, CA 90095

d. Department of Materials Science & Engineering, Johns Hopkins University, Baltimore, MD 21218, USA.

RSC Adv., **2019**, 9, 16492–16495

Supplementary information for this chapter can be found in Appendix B.

2.1 Introduction

In our efforts to address some of the current challenges in design and synthesis of MOFs for integration into active/responsive devices, we introduced a novel building unit for direct extended framework assembly. One strategy that has been used recently to produce electrochemically- and electronically-active MOFs is the integration of redox-active entities within the framework. These entities can facilitate charge delocalization and thereby engender long-range electronic transport pathways. We drew our attention to di-metallic tetracarboxylate clusters with metal–metal multiple bonds because of their tendency to form Class III Robin-Day mixed-valence complexes.[1–3] These four-fold symmetric paddlewheel clusters exhibit redox behavior, and there is spectroscopic evidence for electronic communication within small supramolecular units of these clusters joined by organic or organometallic linkers.[4–9] By comparison, the assembly of these clusters into extended solids and an interrogation of their resulting properties is less developed. Obtaining well-defined and structurally robust coordination polymers and MOFs from these clusters can also be challenging.[10–14]

Our molecular building unit is a four-fold symmetric paddlewheel molecule comprised of two quadruply-bonded molybdenum atoms surrounded by four isonicotinate (INA) ligands coordinated through the carboxylate moiety to both Mo atoms. There are a few important features of this molecule that suggest this material is a promising building block for responsive and active devices:

The first feature is that our molecular building unit contains both the metal and the organic components of a metal-organic framework. The synthesis of the $Mo_2(INA)_4$ paddlewheel unit and the formation of an extended coordination polymer architecture can occur in discrete steps allowing the $Mo_2(INA)_4$ unit to exist in a molecular form analogous to a monomer in typical organic polymer chemistry. In most standard MOF or coordination

polymer syntheses, the metal ion component and organic ligands are combined *in situ* to produce a framework. In our case, $Mo_2(INA)_4$ is synthesized as a molecular species containing all necessary components to be assembled into an extended framework. This affords an added layer of control over the architecture to be assembled. The second feature is the heterotopic isonicotinate ligand which can coordinate equatorially to the Mo atoms via the carboxylate and axially through the unpaired nitrogen electrons. This provides the opportunity for a variety of binding combinations in the modular assembly of new framework architectures. A paddlewheel unit can bind to neighboring units through both, one, or none of its axial Mo sites, each binding mode producing a unique extended framework structure. Because of these two features, the $Mo_2(INA)_4$ paddlewheel will act as a modular building unit to readily self-assemble into unique extended architectures.

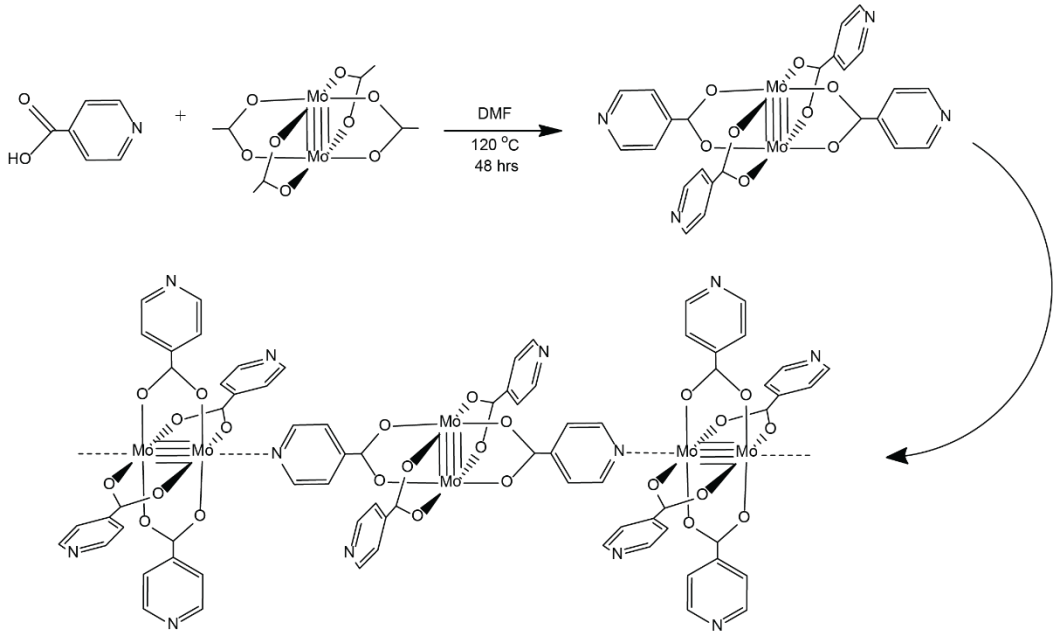

Scheme 2.1 | Synthesis of $Mo_2(INA)_4$ molecular cluster. Ligand exchange reaction of molybdenum acetate with isonicotinic acid in DMF followed by a crystallization of $Mo_2(INA)_4$ to form the coordination polymer.

The final important feature is the Mo_2 quadruply-bonded motif which has been shown in many other molecular and supramolecular species to be redox-active and to display Class

III Robin-Day mixed-valency. The mixed-valency could support long-range through-framework charge transport and tuning the redox state opens the possibility for producing responsive materials. Together, these features make $Mo_2(INA)_4$ molecular clusters a promising candidate for assembly into responsive coordination polymer materials.

2.2 Synthesis of $Mo_2(INA)_4$ molecular cluster

The molecular building unit, $Mo_2(INA)_4$, is synthesized via the ligand exchange reaction of $Mo_2(OAc)_4$ with isoniticotinic acid (**Scheme 2.1**). This reactions refluxes for 2 days and a red polycrystalline precipitate forms as the molecular building units coordinate into an extended framework structure. Electrospray ionization mass spectrometry of a solution of this red precipitate in dimethylsulfoxide (DMSO) and acetonitrile reveals peaks centered around m/z = 681 with isotopic patterning (**Figure 2.1**). ^{1}H NMR analysis shows the aromatic proton shifts for the coordinated INA ligands at 9.00 ppm and 8.22 ppm (**Figure 2.1**). We observe the ratio of INA ligands to coordinated DMF molecules to be 4 to 1; there is one coordinated solvent molecule per paddlewheel unit, or, two solvent molecules coordinated to every other paddlewheel unit. These data confirm that the crystalline product of the reaction outlined in **Scheme 1** is comprised of the $Mo_2(INA)_4$ cluster.

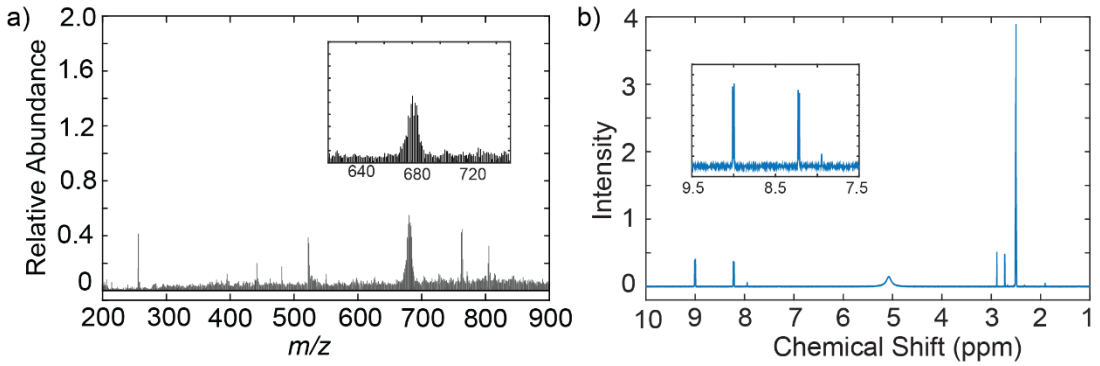

Figure 2.1 | (a) Mass spectrum of $Mo_2(INA)_4$ dissolved in DMSO/ACN reveals a cluster of peaks centered at a molecular ion of 681 m/z. A distribution of peaks about this value is anticipated due to the relative abundance of several isotopes associated with the atoms within the $Mo_2(INA)_4$ cluster. (b) ^{1}H NMR spectrum of 1D coordination polymer after acid digestion. Two unique aromatic

hydrogen atoms are observed in the INA ligands (δ 9.00 ppm, 2H, d, integrated to 8.14; δ 8.22 ppm, 2H, d, integrated to 8.13). Coordinated DMF (δ 7.95 ppm, 1H, integrated to 1.00; δ 2.89 ppm, 3H, integrated to 3.27; δ 2.73 ppm, 3H, integrated to 3.26) with an ratio of DMF to INA of 1 to 4.07. Peaks for water and DMSO are observes at 5.08 ppm and 2.50 ppm, respectively.

2.3 Analysis of 1D coordination polymer (MF–101) architecture and stability

Crystallization of $Mo_2(INA)_4$ molecular clusters from a DMF solution induces assembly into an extended modular framework, MF–101. Large single crystals of MF–101 were obtained by stirring the aforementioned reaction (**Scheme 1.1**) at 60 rpm. The structure of these single crystals was determined by X-ray crystallography (**Figure 2.2**). The crystal structure of MF–101 contains one-dimensional (1D) chains comprised of $Mo_2(INA)_4$ clusters that alternately bind through axial and equatorial binding sites. One DMF solvent molecule is coordinated to each of two Lewis acidic axial Mo sites on every other cluster. This coordination motif is supported by proton NMR data. The Mo–Mo bond lengths in the two clusters are 2.1219(5) Å and 2.1189(5) Å. These distances are within the anticipated range of lengths for Mo–Mo quadruple bonds (2.06–2.17) Å (as described by Murillo *et al.*)[15,16] and consistent with axial coordination of a strongly donating ligand such as pyridine. Furthermore, we observe a Raman band at 383 cm^{-1} (**Figure A1**), which is relatively weaker than that anticipated for axially under-coordinated Mo_2 complexes, and treat this observation as further evidence for the axial donation effect. We note that the Mo_2 centers within each molecular chain are coordinatively saturated and do not bond to pyridines from neighboring chains (**Figure 2.2**).

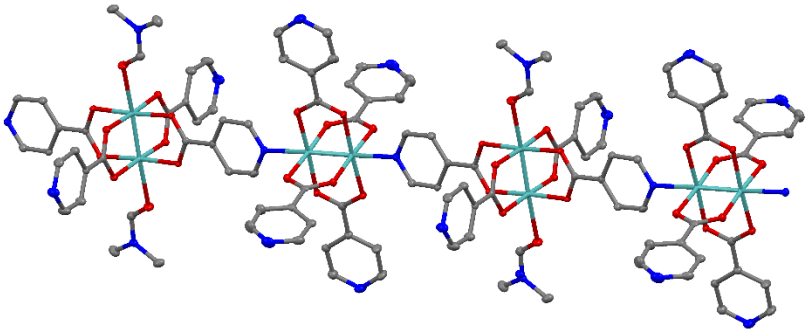

Figure 2.2 | Structure of the 1D coordination polymer, MF–101, showing the paddlewheel units that alternately bond through axial Mo (cyan) and equatorial N (blue) binding sites. Ellipsoids are show at 50% probability level. Disorder and H atoms have been omitted for clarity.

We next characterized the phase purity, stability, and porosity of bulk samples of MF–101. First, powder X-ray diffraction (pXRD) patterns collected from products precipitated across a range of stir rates (60–300 rpm) match well with the pXRD pattern simulated from the single-crystal XRD data discussed above (Figure 2.3). These data suggest that a single common crystal phase is produced regardless of stir rate, though stir rates <100 rpm are conducive to the formation of high-quality single crystals. Second, Fourier transform infrared (FT-IR) spectroscopy data show no evidence of H-INA or $Mo_2(OAc)_4$ in the bulk crystalline powder (**Figure 2.4a**), suggesting good purity of our bulk samples. Third, thermogravimetric analysis shows a mass loss of 10.1% between 190 °C and 252 °C that can be attributed to the loss of coordinated DMF molecules, which account for 9.7% of MF–101 (**Figure 2.4b**). Upon further heating, the sample rapidly loses mass above 350 °C and likely degrades. Finally, nitrogen gas adsorption measurements on the crystalline powder yield a Brunauer–Emmett–Teller (BET) surface area of 325.8 $m^2\ g^{-1}$ (**Figure A2**). We note that this modest BET surface area is reasonable given the tight packing of the 1D chains of MF–101 (**Figure A3**).

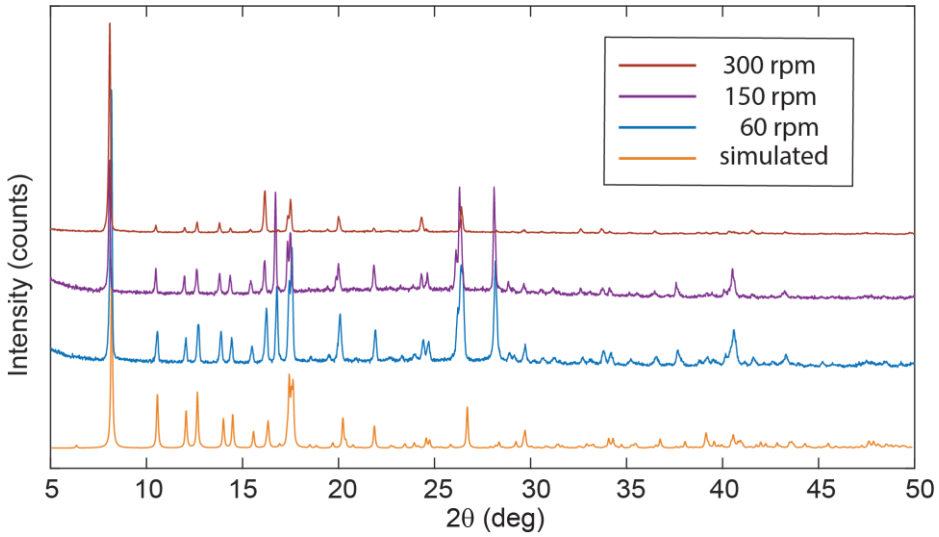

Figure 2.3 | Powder X-ray diffraction scans of MF–101 synthesized at various reaction stir rates. The synthesis of MF–101 was performed with stir rates of 300 rpm (red), 150 rpm (purple), and 60 rpm (blue) to determine the effect of solution agitation on crystal structure of the crystalline powder product. When the reaction is performed at 300 rpm, all of the product recovered is in polycrystalline powder form. At 60 rpm, the reaction produces large single crystals as well as powder product. A simulated pXRD pattern was calculated from the single crystal structure of the 1D coordination polymer (orange).

The conditions described above produce a 1D coordinated chain of $Mo_2(INA)_4$, though the physical and structural state of the synthesized material is dependent on the solvent environment. When fully dissolved, the material reverts back to its molecular form. When the solvent environment is changed (solvent removal, crystallization, etc.) the monomer units self-assemble into extended frameworks. This is observed in the ESI-MS data collected from a fully-dissolved solution and is further emphasized through UV–Vis spectroscopic analysis along with density-functional theory calculations.

2.4 Density functional theory calculations of electronic transitions of $Mo_2(INA)_4$ monomer and dimer

A diffuse reflectance UV–Vis spectrum collected from a powder sample of MF–101 exhibits a broad absorption feature between 400 and 600 nm (**Figure 2.5**). The UV–Vis

absorption spectrum of a solution sample of MF–101 dissolved in DMF exhibits a significant feature centered at 470 nm. We ascribe the modest absorption shoulder at 570 nm to absorption by remnant 1D coordinated chains. We used computational methods[17,18] to examine orbital interactions and electronic transitions that may be responsible for the absorption features identified above. Single point energies and molecular orbitals were calculated from coordinates taken directly from the single-crystal structure of MF–101. The B3LYP functional was used with the 6-31g* basis set for H, C, N, O and the Stuttgart/Dresden effective core potential for Mo. In the ground state, the first four highest-energy occupied molecular orbitals are all metal-centered, with discrete energy levels, localized electron density, and little sharing between the two coordinatively distinct clusters (**Figure A4**). These computational results suggest that charge (e.g. introduced from an external circuit or generated chemically *in situ*) would likely remain localized on the individual clusters comprising MF–101.

We performed time-dependent DFT (TD-DFT) calculations to identify possible optical transitions in MF–101. We did so by considering the electronic structure of a single $Mo_2(INA)_4$ cluster coordinated by a DMF molecule at both axial sites, and of two $Mo_2(INA)_4$ clusters having the same coordination environment as observed in the crystal structure of MF–101. Henceforth we will refer to the former as the monomer and the latter as the dimer. For the monomer, calculations identify a 2.44 eV (508 nm) transition primarily between a HOMO of Mo_2 δ character and a ligand-based π* LUMO, which is nearly degenerate with several higher lying LUMO orbitals (**Figures 2.6** and **A5**). The character of this transition is typical of the metal–ligand charge transfer (MLCT) transitions reported in analogous transition-metal complexes. We note that the calculated HOMO–LUMO transition energy for the monomer is in reasonable agreement with the 470 nm feature observed in the absorption spectrum of the

solution sample of MF–101 dissolved in DMF. On the basis of these data we can assign the aforementioned 470 nm feature to absorption by the isolated monomer.

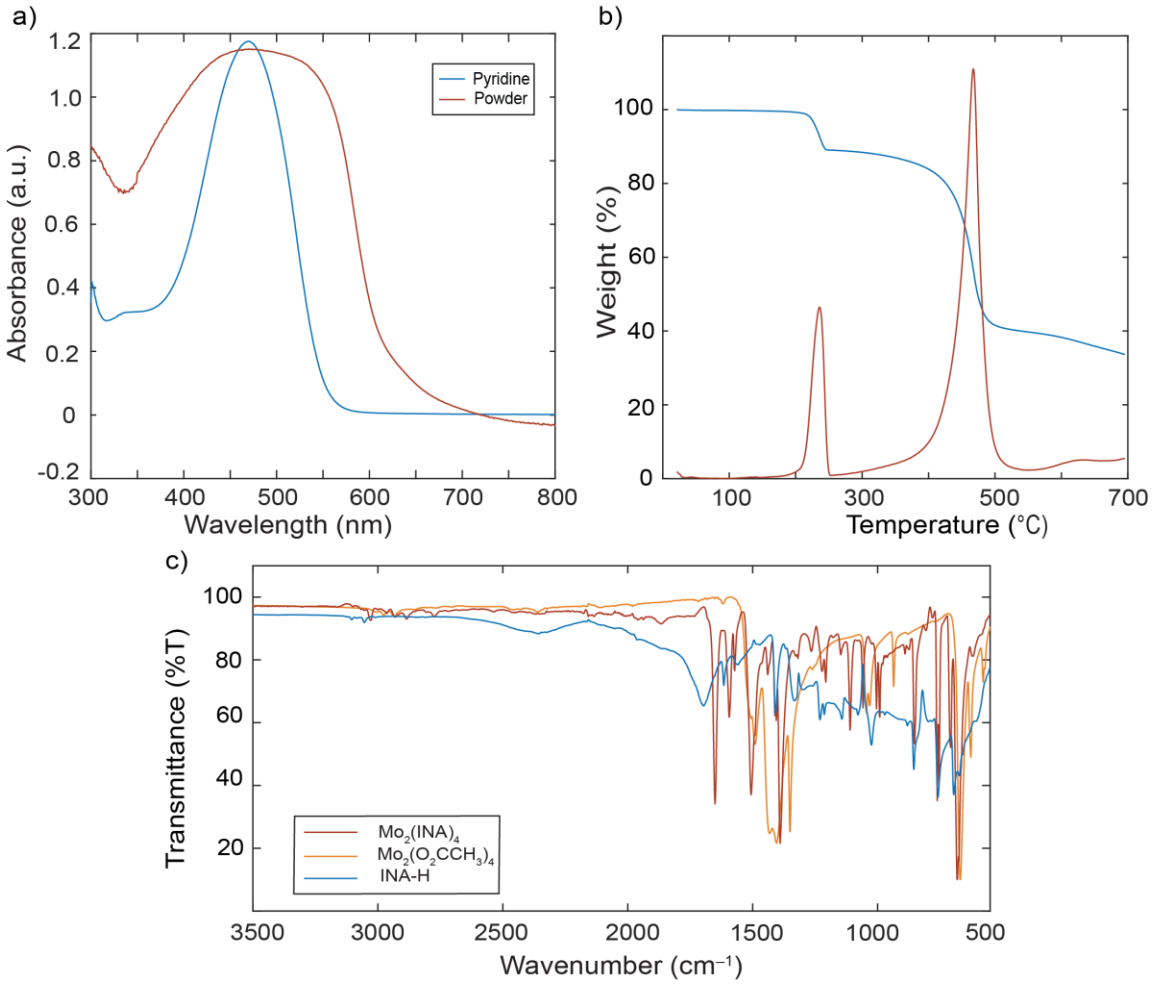

Figure 2.4 | (a) UV–Vis spectra of 1D coordination polymer in powder form (red) and dissolved in DMF (blue). (b) Thermogravimetric analysis of MF–101. The weight loss curve (blue) and its derivative (orange) show a sharp mass loss of 10.1 % between 190 °C and 252 °C, which likely corresponds to the loss of coordinated DMF (9.7 %). The coordination polymer began to rapidly lose mass above 350 °C, a likely sign of degradation. (c) Infrared spectra of MF–101 (red) and reaction starting materials (isonicotinic acid, green; molybdenum acetate, blue).

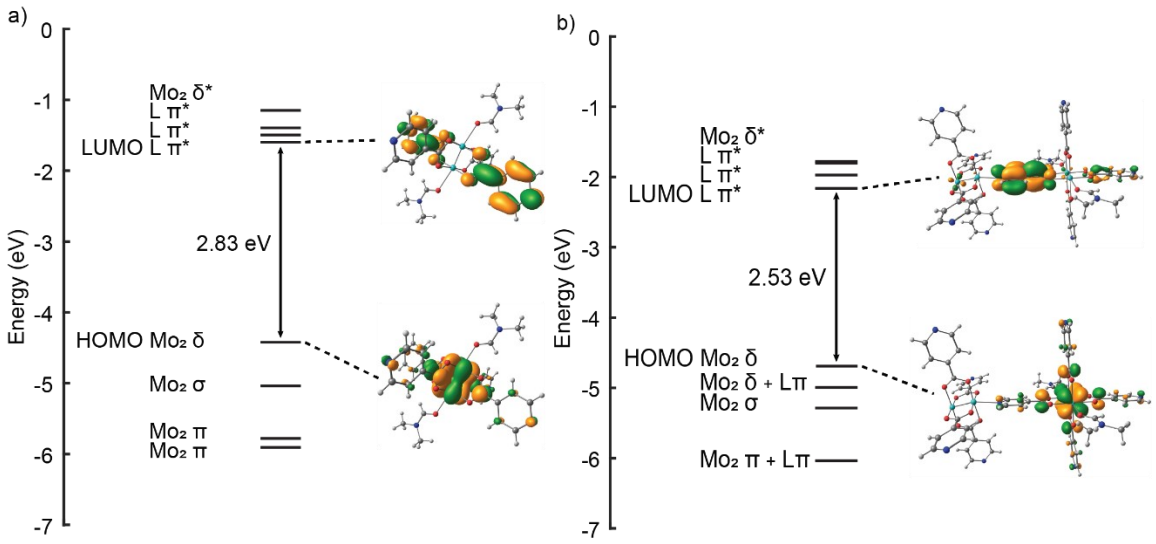

Figure 2.5 | DFT calculated HOMO and LUMO orbitals of a. monomer and b. dimer. The calculated HOMO–LUMO transition energies are 2.83 eV for the monomer and 2.53 eV for the dimer. These transition energy calculations support the observed UV-vis absorbances.

Turning our attention to the dimer, TD-DFT calculations identify a 2.19 eV (566 nm) transition primarily between a HOMO of Mo_2 δ character and a ligand-based π* LUMO orbital (**Figures 2.5** and **A6**). We also note two higher energy MLCT transitions primarily from HOMO to LUMO+5 and from HOMO+1 to LUMO+1 with energies of 2.59 eV (479 nm) and 2.61 eV (475 nm), respectively (**Figure A6**). Notably, while the two higher energy MLCT transitions involve LUMO orbitals located on the INA ligands perpendicular to the dimer axis, the lower energy MLCT transition at 2.19 eV involves a LUMO orbital of the INA ligand along the dimer axis. The calculated dimer transition energies cover much of the broad absorption envelope observed in the spectrum of the powder of MF–101. In particular, the low energy MLCT transition at 566 nm calculated for the dimer likely accounts for the significant absorption at wavelengths greater than 500 nm (**Figure 2.6**). These data suggest the dimer is a good simulant of the electronic properties of MF–101. This is a reasonable expectation given that the coordination polymer framework can be viewed, from a structural standpoint, as a linear polymer chain of the dimers. We can conclude that our 1D coordination polymer

has an electronic structure comprised of dimer-like MLCT states arising from a lifting of the degeneracy of monomer orbitals due to their altered symmetry in the 1D chain.

2.5 Electron paramagnetic resonance spectroscopy of MF–101

Our results show that the alternating coordination environment along the backbone of our 1D coordination polymer gives rise to a unique chain topology with a distinct electronic structure and function. Further evidence for the functionally distinct nature of MF–101 over the monomer is provided by X-band electron paramagnetic resonance (EPR) spectroscopy. An EPR spectrum collected from a powder sample of MF–101 at 20 K reveals an EPR active system with weak hyperfine structure owing to ^{95}Mo and ^{97}Mo isotopes, which have $I = 5/2$ nuclear spin (**Figure 2.6**). This spectrum is qualitatively similar to spectra reported for EPR active Mo_2^{V} species in transition metal alkoxide-bridged dimolybdenum clusters.[23] This suggests the presence of Mo^{II} and Mo^{III} centers in MF–101 that may have formed during partial oxidation of the powder sample. It is anticipated that the hole is equally present on both Mo atoms as expected from the Class III Robin-Day classification of such systems. We simulated the experimental EPR spectrum by modelling our 1D coordination polymer system as a single axial paramagnet and obtained g values of $g_{\parallel} = 1.895$ and $g_{\perp} = 1.935$ and a perpendicular hyperfine coupling constant $A_{\perp}$ of 3.9 mT (**Figures 2.6** and **A7**).[19] The hyperfine coupling observed for MF–101 is consistent with values reported for systems containing isolated Mo_2^{V} ions.[6] Moreover, the fact that a single paramagnet model was sufficient to simulate the EPR spectrum suggests that the two distinct coordination environments are fairly similar electronically. Though our EPR data provide evidence for charge localization on Mo_2 centers, we cannot exclude the possibility for photo-induced intra-chain (or indeed inter-chain) charge transport arising from population of the low energy LUMO orbital on each bridging INA ligand.

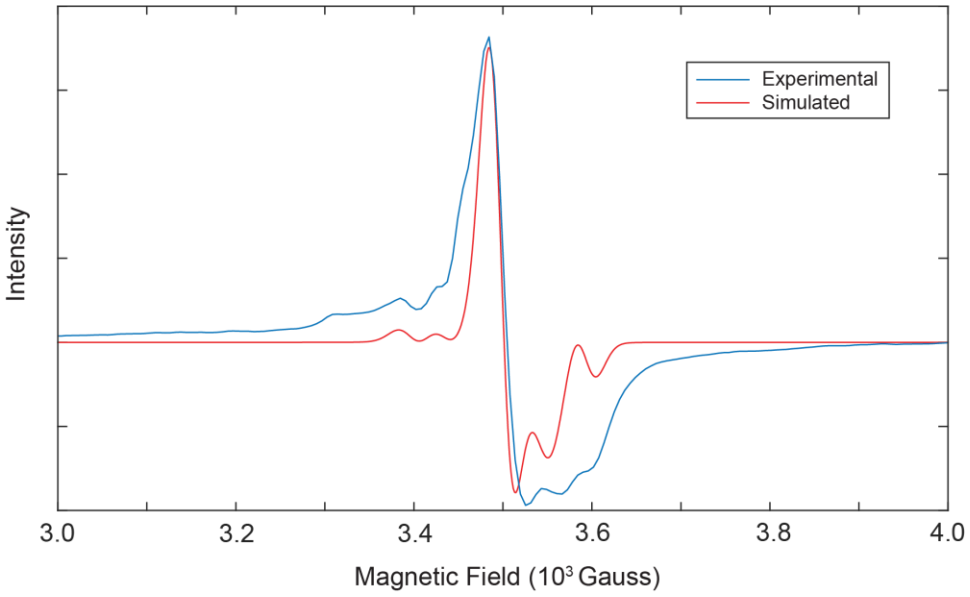

Fig. 2.6: Experimental electron paramagnetic resonance spectrum of MF–101 collected at 20 K (blue) and 9.44 GHz. In EasySpin, a fifth-order background correction was applied, and the system was modeled as an axial paramagnet with $g_{\parallel}$ = 1.895 and $g_{\perp}$ = 1.935 (red).

2.6 Conclusions

The work discussed in this chapter lays the foundation for assembly of new coordination polymers and MOFs of varying dimensionality from discrete molecular building units that have the potential to support through-framework charge transport due to mixed-valence mechanisms. The $Mo_2(INA)_4$ paddlewheel has been shown to assemble into an extended framework dependent on the solvent environment and the framework has interesting properties distinct from those of the molecular cluster. In the next chapters, I will discuss how we exploited the modularity of the $Mo_2(INA)_4$ molecular cluster to produce a series of new MOF architectures with their own unique properties.

REFERENCES

1. Cotton, F. A.; Donahue, J. P.; and Murillo, C. A.; The simplest supramolecular complexes containing pairs of Mo(2)(formamidinate)(3) units linked with various dicarboxylates: preparative methods, structures, and electrochemistry. *Inorg. Chem. Commun.*, **5**, 59–63 (2002).
2. Patmore, N. J. in *Organometallic Chemistry*, Royal Society of Chemistry, Cambridge, 2010, pp. 77–92.
3. Cotton, F. A.; Lin, C.; and Murillo, C. A.; Supramolecular Arrays Based on Dimetal Building Units. *Acc. Chem. Res.*, **34**, 759–771 (2001).
4. Chisholm, M. H.; and Macintosh, A. M.; Linking Multiple Bonds between Metal Atoms: Clusters, Dimers of "Dimers", and Higher Ordered Assemblies. *Chem. Rev.*, 2005, **105**, 2949–2976 (2005).
5. Chisholm, M. H.; Metal to metal multiple bonds in ordered assemblies. *Proc. Natl. Acad. Sci.*, **104**, 2563–2570 (2007).
6. Cotton, F. A.; Dalal, N. S.; Liu, C. Y.; Murillo, C. A.; Micah North, A. J.; Wang, X.; Fully Localized Mixed-Valence Oxidation Products of Molecules Containing Two Linked Dimolybdenum Units: An Effective Structural Criterion *J. Am. Chem. Soc.*, **125**, 12945–12952 (2003).
7. Chisholm, M. H.; Lear, B. J.; $M_2\delta$ to ligand π-conjugation: testbeds for current theories of mixed valence in ground and photoexcited states of molecular systems *Chem. Soc. Rev.*, **40**, 5254 (2011).
8. Kubiak, C. P.; Inorganic Electron Transfer: Sharpening a Fuzzy Border in Mixed Valency and Extending Mixed Valency across Supramolecular Systems. *Inorg. Chem.*, **52**, 5663–5676 (2013).
9. Chisholm, M. H.; Dann, A. S.; Dielmann, F.; Gallucci, J. C.; Patmore, N. J.; Ramnauth, R.; Scheer, M. Dimolybdenum Bis-2,4,6-triisopropyl-benzoate Bis-4-isonicotinate: A Redox

Active Analogue of 4,4′-Bipyridine with Ambivalent Properties *Inorg. Chem.*, **47**, 9248–9255 (2008).

10. Cotton, F. A.; Jin, J.-Y.; Li, Z.; Liu, C. Y.; Murillo, C. A.; A deliberate approach for the syntheses of heterometallic supramolecules containing dimolybdenum $Mo_2$4+ species coordinated to other metal units. *Dalt. Trans.*, 2328-2335 (2007).
11. Hsu, W.; Li, Y.-S.; He, H.-Y.; Chen, K.-T.; Wu, H.-S.; Proserpio, D. M.; Chen, J.-D.; Wang, J.-C.; Stepwise formation of heteronuclear coordination networks based on quadruple-bonded dimolybdenum units containing formamidinate ligands. *CrystEngComm*, **16**, 7385–7388 (2014).
12. Cai, X.-M.; Höhne, D.; Köberl, M.; Cokoja, M.; Pöthig, A.; Herdtweck, E.; Haslinger, S.;. Herrmann, W. A; Kühn, F. E. Synthesis and Characterization of Dimolybdenum(II) Complexes Connected by Carboxylate Linkers *Organometallics*, **32**, 6004–6011 (2013).
13. Ke, Y.; Collins, D. J.; Zhou, H.-C.; Synthesis and Structure of Cuboctahedral and Anticuboctahedral Cages Containing 12 Quadruply Bonded Dimolybdenum Units *Inorg. Chem.*, **44**, 4154–4156 (2005).
14. Robin, A. Y.; Fromm, K. M.; Coordination polymer networks with O- and N-donors: What they are, why and how they are made. *Coord. Chem. Rev.*, **250**, 2127–2157 (2006).
15. Cotton, F. A.; Daniels, L. M.; Hillard, E. A.; Murillo, C. A.; The Lengths of Molybdenum to Molybdenum Quadruple Bonds: Correlations, Explanations, and Corrections *Inorg. Chem.*, **41**, 2466–2470 (2002).
16. Cotton, F. A.; Norman, J. G.; Molybdenum(II) trifluoroacetate dimer. Bispyridine adduct *J. Am. Chem. Soc.*, **94**, 5697–5702 (1972).
17. Miehlich, B.; Savin, A.; Stoll, H.; Preuss, H.; Results obtained with the correlation energy density functionals of becke and Lee, Yang and Parr *Chem. Phys. Lett.*, **157**, 200–206 (1989).

18. Alberding, B. G.; Chisholm, M. H.; Gallucci, J. C.; Ghosh Y.; Gustafson, T. L.; Electron delocalization in the S1 and T1 metal-to-ligand charge transfer states of trans-substituted metal quadruply bonded complexes *Proc. Natl. Acad. Sci. U. S. A.*, **108**, 8152–6 (2011).
19. Mabbs, F. E.; Collison, D.; *Electron Paramagnetic Resonance of d Transition Metal Compounds*, Elsiever Science Publishers, Amsterdam, The Netherlands, 1992.

CHAPTER THREE

Two-dimensional MOFs assembled from redox-active $Mo_2(INA)_4$ modular building unit

---

This work was co-authored with the following authors and is published under the following citation:

F. James Claire,[a] Minyuan M. Li,[a] Stephanie M. Tenney,[a] Maxime A. Siegler,[a] Justine S. Wagner,[b] Anthony S. Hall,[b] and Thomas J. Kempa*[a,b]

a. Department of Chemistry, Johns Hopkins University, Baltimore, MD 21218, USA

b. Department of Materials Science & Engineering, Johns Hopkins University, Baltimore, MD 21218, USA.

J. Am. Chem. Soc. **2018**, 140, 34, 10673–10676

Supplementary information for this chapter can be found in Appendix B.

3.1 Introduction

In the last chapter, we introduced the molecular building unit, $Mo_2(INA)_4$, which was assembled into our first modular framework, MF–101, through a solution-phase crystallization process. We can further elucidate the intrinsic and responsive properties of $Mo_2(INA)_4$-based frameworks by developing novel architectures from our unique modular building unit.

The $Mo_2(INA)_4$ paddlewheel structure includes multiple Lewis acidic and Lewis basic sites which allow for a variety of binding modes. In the 1D linear framework, the coordination occurs at the axial Mo sites of one paddlewheel unit and at two *trans* INA nitrogen atoms of neighboring units. In this binding mode, the axial sites of every second $Mo_2(INA)_4$ cluster remain uninvolved in the extended coordination framework; solvent molecules coordinate to these sites rather than neighboring $Mo_2(INA)_4$ units. By removing these solvent molecules, we can create new coordination sites orthogonal to the 1D linear chain, opening the possibility of producing MOFs with higher dimensionality. In this chapter, we introduce a pair of two-dimensional (2D) frameworks assembled from $Mo_2(INA)_4$ modular building units, MF–102 and MF–103.

3.2 Assembly and structural analysis of 2D metal-organic frameworks

We discovered that recrystallizing the 1D coordination polymer, MF–101, in DMA removes the coordinated solvent molecules from the $Mo_2(INA)_4$ clusters and yields a dark red crystalline material consisting of layers 2D MOF sheets. In this new MOF structure, each paddlewheel unit is coordinated to neighboring units through two trans INA nitrogen atoms and two axial Mo sites (**Figure 3.1**). Rather than directly coordinating to the framework as the DMF molecules did,[1] the DMA molecules reside between the layers of the MOF within rectangular pores. We observe that the solvent environment plays a role in the exact

structure of the 2D MOF assembly, producing unique pore structures under certain conditions.

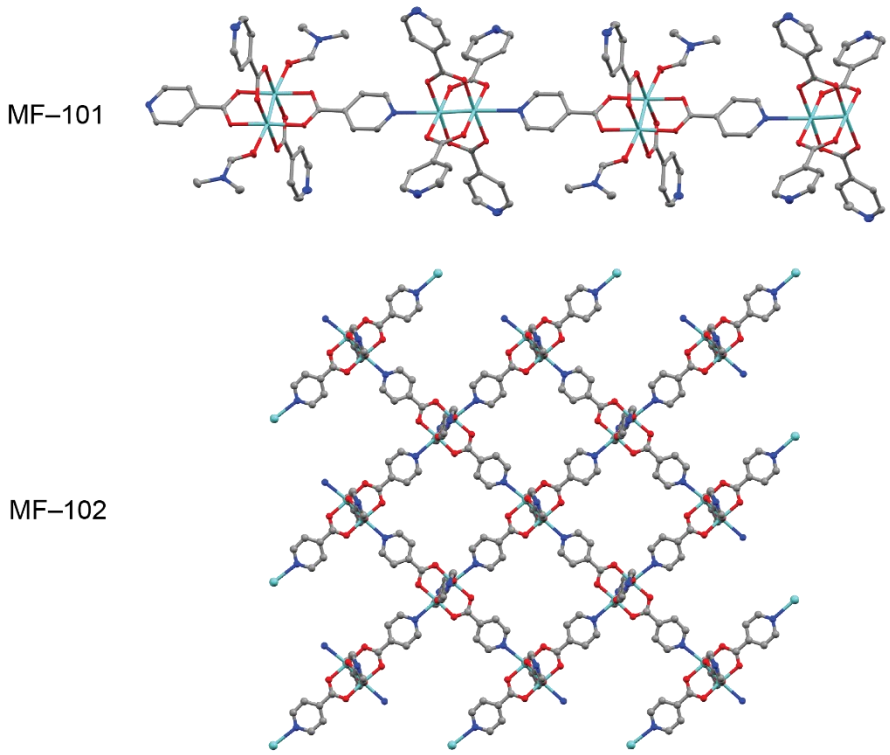

Figure 3.1 | 1D coordination polymer structure contains DMF molecules coordinated to axial Mo site in alternating paddlewheel clusters (top). In the 2D MOF structure all axial Mo sites coordinate to neighboring paddlewheel units through the INA nitrogen atom (bottom).

To assemble 2D MOFs from the $Mo_2(INA)_4$ molecular cluster, we performed recrystallizations from solutions containing $Mo_2(INA)_4$ and either pure dimethylacetamide (DMA) or DMA and 1,4-diazabicyclo[2.2.2]octane (DABCO). Recrystallization at room temperature over the course of two days yielded dark red single crystals from DMA solutions (MF–102) and from DMA and DABCO solutions (MF–103). Crystal structures obtained from single crystal X-ray diffraction (XRD) experiments (**Table B1**) conducted at 110 K on MF–102 and on MF–103 (**Figure 3.2**) identify several salient features of the new $Mo_2(INA)_4$ frameworks we have assembled. First, the paddlewheel units remain intact after the

recrystallization process with the Mo–Mo bond distances in MF–102 and MF–103 being 2.1211(4) Å and 2.1227(3) Å, respectively. These distances are within 2% of the Mo–Mo bond distances typically observed in quadruply bonded di-Mo cores coordinated by three-atom bridging ligands such as carboxylates.[2] Second, each Mo is bonded to the pyridyl N of the INA ligand of an adjacent node with Mo–N bond distances within MF–102 and MF–103 ranging between 2.546(3) and 2.586(3) Å. These coordination bonds give rise to a 2D lattice of $Mo_2(INA)_4$ nodes (**Figure B1**). Finally, packing diagrams viewed down the *c* axis of both MF–102 and MF–103 (**Figure 3.2**) show that the crystals (space groups, MF–102: $P2/c$ and MF–103: $P2_1/c$) are significantly porous and composed of the 2D lattices stacked commensurately on top of one another. Together, these data show successful assembly of a 2D MOF composed of $Mo_2(INA)_4$ clusters joined into a 2D lattice[3,4] through Mo–N covalent bonds.

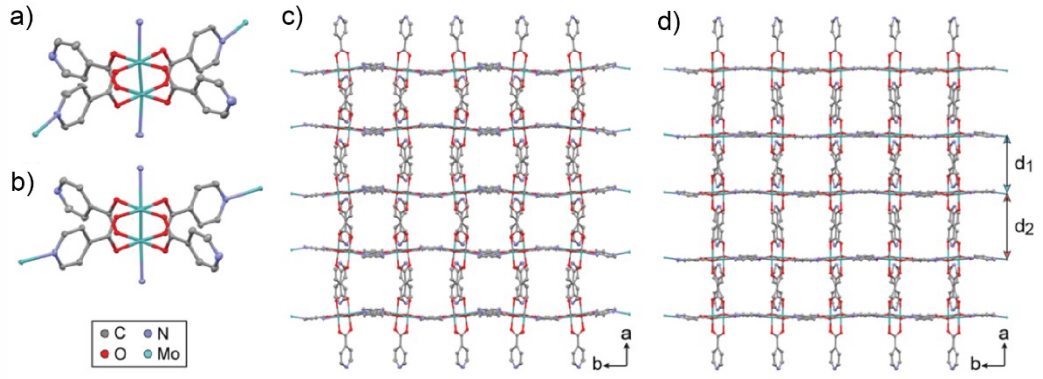

Figure 3.2 | (a) crystal structure of the (a) Crystal structure of the $Mo_2(INA)_4$ cluster used to assemble MF–102 whose crystal packing is shown in 'c'. (b) Crystal structure of the $Mo_2(INA)_4$ cluster used to assemble MF–103 whose crystal packing is shown in 'd'. (c) Crystal packing structure of I viewed down the c axis. (d) Crystal packing structure of MF–103 viewed down the c axis. Hydrogen atoms, lattice solvent molecules and disorder have been omitted for clarity. Displacement ellipsoids are given at 50% probability.

A detailed analysis of the structures of MF–102 and MF–103 identifies several features of our 2D material that are sensitive to recrystallization condition. The (100) lattice planes of MF–102 and MF–103, are comprised of slightly distorted square sub-cells containing 4 covalently bonded $Mo_2(INA)_4$ nodes (Figure B1). The in-plane diagonals of these

sub-cells are 14.015 Å and 12.991 Å, and 14.313 Å and 12.809 Å for MF–102 and MF–103, respectively. Furthermore, while the (100) lattice planes in MF–102 are separated by an average interplanar spacing of 8.190 Å, those in MF–103 regularly alternate between two distinct *d* spacings of d_1 = 7.854 Å and d_2 = 8.565 Å (**Figure 3.2**). In the structure of MF–102, the lattice DMA solvent molecules show significant disorder in their packing orientation and pore occupancy (**Figure B2**). In the structure of MF–103, the lattice DMA solvent molecules orient parallel (perpendicular) to the (100) lattice planes in the interplanar space having a thickness d_1 (d_2) (**Figure B2**). Previously, DABCO has been integrated into MOFs as a pillaring molecule intended to organize square-grid layered structures into 3D open frameworks.[5] Notably, crystal structures and acid digestions of bulk crystalline samples of MF–103 verify that no DABCO is present in MF–103 (**Figure B3**). These data suggest that though DABCO does not integrate into MF–103 it does appear to be responsible not only for the improved ordering of the crystal, but also the intriguing alternate ordering of interplanar spacing between the lattices.

3.3 Surface area and CO_2 adsorption measurements of MF–102

Having established the long-range crystalline order of 2D MOFs prepared from $Mo_2(INA)_4$ precursor, we set out to assess their porous characteristics through Brunauer-Emmett-Teller (BET) analysis. BET analysis of CO_2 adsorption and desorption for isotherms collected at 195 K on MF–102 reveals several unique features (**Figure 3.3**). The adsorption data exhibit three distinct regions (*A*: 0–0.3 p/p_0; *B*: 0.3–0.5 p/p_0; *C*: 0.5–0.9 p/p_0) and can be broadly classified as belonging to a Type VI isotherm.[6] These data suggest that CO_2 at 195 K infiltrates a distribution of micropores and mesopores within MF–102. Further analysis shows only two distinct transitions within the desorption data and a significant hysteresis loop between adsorption and desorption data. These features suggest that infiltrated CO_2

undergoes capillary condensation within the distribution of pores in MF–102, and then undergoes desorption *via* a mechanism incommensurate with that associated with its adsorption.[7] We note that calculation of pore surface areas for complex isotherms, such as this one, that exhibit a number of distinct features is not trivial. Nevertheless, specific BET and Langmuir pore surface areas calculated from the adsorption isotherm within the 0.05–0.3 p/p_0 region (**Figure 3.3**) and at saturation (0.95 p/p_0)[8] are 18.6 m^2/g and 505.1 m^2/g, respectively (**Figure B4**). Notably, pXRD data of MF–102 taken after BET analysis show that the crystal structure of MF–102 is well retained (**Figure B5**).

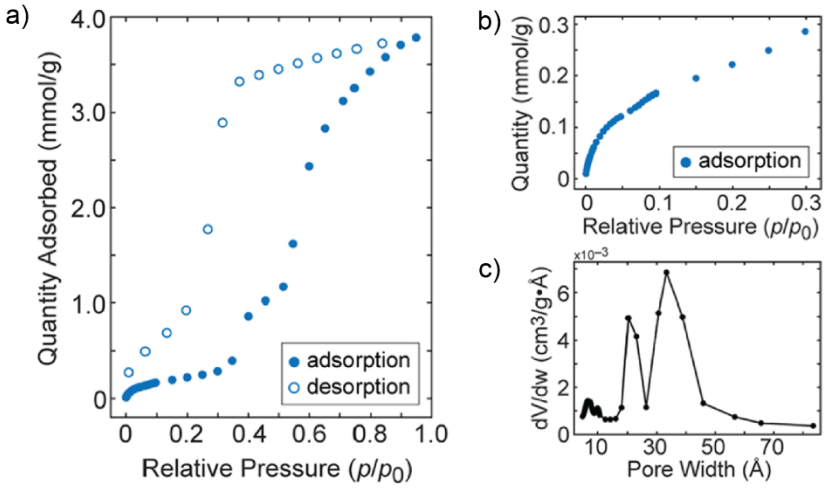

Figure 3.3 | (a) The adsorption and desorption portions of the CO_2 isotherm collected at 195 K on MF–102. (b) Expanded view of the CO_2 adsorption isotherm shown in 'a' to emphasize the 0–0.3 p/p_0 region, which is used to calculate the BET pore surface area. (c) Differential pore volume (dV/dw) data identifying the pore sizes in MF–102 that are predominantly filled by CO_2.

A plot of differential pore volume as a function of pore width was obtained through analysis of the adsorption data with the Horvath-Kawazoe model (**Figure 3.3**). The pore distribution data identify two narrow peaks associated with pore widths of 7 Å and 10 Å, and two broad peaks associated with pore widths of 20 Å and 33 Å. The former two peaks can be associated with CO_2 uptake by the ~13–14 Å pores formed by the square sub-cells comprising the 2D planes of MF–102 (**Figure B2**), while the latter two peaks may be associated with CO_2

uptake by pores in the interplanar space between 2D layers. Integration of the differential pore width data shows that 84% of the total adsorbed CO_2 is sequestered by pores > 20 Å in width. The unique CO_2 uptake and storage properties of MF–102 are likely a consequence of the hierarchical structure of our material. In particular, it is possible that the crystal expands about the interplanar space to accommodate more CO_2 storage at higher relative pressures. Investigation into the structural expansion and CO_2 adsorption in MF–102 is ongoing. We intend to elucidate the mechanism of gas adsorption and layer expansion via neutron scattering experiments.

3.4 Cyclic voltammetry of MF–102

Finally, the redox properties of MF–102 were assessed through cyclic voltammetry (CV) and electrokinetic analysis of CV data taken at multiple scan rates. CV data of MF–102 taken at a scan rate (ν) of 50 mV/s in acetonitrile, 0.1 M tetrabutylammonium hexafluorophosphate (TBA PF_6) and 20 mM 1-butyl-3-methylimidazolium tetrafluoroborate (BMIM BF_4) identify several features (**Figure 3.4**). First, a small anodic wave is apparent between –100 mV and +100 mV (*vs.* the Fc/Fc^+ redox couple) in CVs collected at ν = 50 mV/s and ν = 5 mV/s (**Figure 3.4**). Previously reported CV data of molecular dimers of quadruply bonded di-Mo clusters have identified oxidation waves at –90 mV[10] and +100 mV[11] relative to Fc/Fc^+ that were attributed to $[(^tBuCO_2)_3Mo_2]_2(\mu\text{-}O_2C\text{–}C_{10}H_6\text{–}CO_2)^{0/+1}$ and $[(^tBuCO_2)_3Mo_2]_2(\mu\text{-}O_2C\text{–}C_6F_4\text{–}CO_2)^{0/+1}$ couples, respectively. Therefore, we assign the modest anodic peak between –100 and +100 mV in CVs of MF–102 to the $[Mo_2(INA)_4]^{0/+1}$ couple.

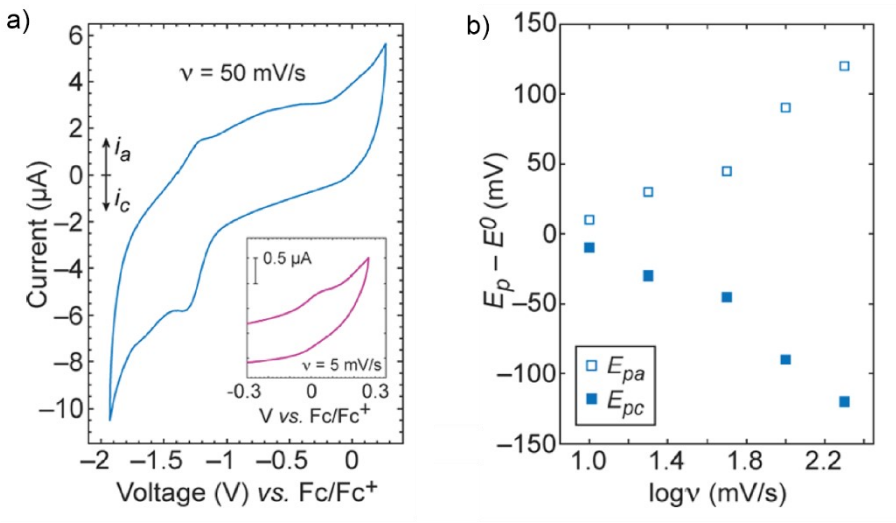

Figure 3.4 | (a) Cyclic voltammogram of MF–102 in acetonitrile, TBA PF_6, and BMIM BF_4 collected at a scan rate of 50 mV/s. Inset: Expanded view of anodic wave in CV of MF–102 at ν = 5 mV/s. (b) Trumpet plot assembled from data of cathodic (E_{pc}) and anodic (E_{pa}) peak potentials as a function of scan rate (Figure B7). All potentials are referenced to Fc/Fc^+.

Second, a quasi-reversible (i_{pa}/i_{pc} = 0.26) redox wave with $E_{1/2}$ = –1.275 V is apparent, and multiple CV scans taken at ν = 50 mV/s show retention of this redox wave (**Figure B6**). The cathodic and anodic peak potentials associated with this feature are E_{pc} = –1.32 V and E_{pa} = –1.23 V, respectively, and their separation implies a one-electron process. We note that reduction of a range of isonicotinates was previously reported[12] to occur at –2.2 V versus Ag/Ag^+ (~ –2.6 V vs. Fc/Fc^+), which is well outside of our scanned potential range. We consequently rule out the possibility that cathodic features in our reported CVs of MF–102 are due to reduction of INA ligand. Therefore, we assign the cathodic peak at –1.32 V to one-electron reduction and associate the redox wave at $E_{1/2}$ = –1.275 V with the $[Mo_2(INA)_4]^{0/-1}$ couple. A subsequent electrokinetic analysis was used to determine the rate of electron transfer associated with this couple. CVs of MF–102 were collected at scan rates ν = 5, 10, 20, 50, 100, and 200 mV/s (**Figure B7**). These data show an increase, as a function of increasing scan rate, in the splitting of the cathodic and anodic peak potentials associated with this couple. This observation is consistent with the onset of electrochemical irreversibility as the

electrode reaction becomes dominated by the kinetics of electron transfer at the electrode. Using these data, a plot of the difference between the cathodic or anodic peak potential and the mid-point potential for the $[Mo_2(INA)_4]^{0/-1}$ couple versus the logarithm of the scan rate was prepared (**Figure 3.4**). A Laviron analysis[13] of these data furnishes a standard heterogeneous electron transfer (ET) rate constant $k_s = 1.49\ s^{-1}$ for the $[Mo_2(INA)_4]^{0/-1}$ couple, assuming a one-electron process and a transfer coefficient $\alpha = 0.5$ (**Figure B8**). This rate is comparable to rates reported for ET kinetics of quinones attached to electrodes *via* self-assembled monolayers. Collectively, the foregoing electrochemical analyses identify that our 2D MOF, MF–102, is redox-active.

3.5 Conclusions

This work demonstrates the modularity of the $Mo_2(INA)_4$ molecular cluster as a precursor for MOF assembly. Changing the solvent environment changed the coordination among neighboring $Mo_2(INA)_4$ clusters to produce new 2D frameworks. The 1D coordination polymer, MF–101, had an alternating coordination pattern with the axial Mo sites of every second paddlewheel cluster coordinated to solvent molecules. Removing the coordinated solvent molecules allows for a uniform coordination environment for each paddlewheel cluster to form 2D coordinated sheets, MF–102 and MF–103.

We show that the 2D MOF displays redox activity, rendering it a compelling material for integration into device architectures. Anomalous adsorption of CO_2 within the layered architecture shows that MF–102 has a flexible and responsive structure. In combination, the intrinsic redox activity and structural responsivity of MF–102 show that frameworks assembled from the modular building unit $Mo_2(INA)_4$ are promising candidates for implementation into active devices. In the next chapter, we will introduce a novel synthetic method for our modular frameworks and test their responsive properties within devices.

REFERENCES

1. Li, M. M.; Claire, F. J.; Solomos, M. A.; Tenney, S. M.; Ivanov, S. A.; Siegler, M. A.; Kempa, T. J. Molecular chains of coordinated dimolybdenum isonicotinate paddlewheel clusters. *RSC Adv.* **9**, 16492–16495 (2019).
2. Cotton, F. A.; Mester, Z. C.; Webb, T. R.*;* Dimolybdenum Tetraacetate. *Acta. Crystallogr*. Sect. B, B30, 2768 (1974).
3. Wasielewski, M. R.; Wu, Y.-L.; Bobbitt, N. S.; Logsdon, J.; Powers-Riggs, N.; Nelson, J.; Liu, X.; Wang, T.; Snurr, R.; Hupp, J.; Farha, O.; Hersam, M. Tunable Crystallinity and Charge Transfer in Two-Dimensional G-Quadruplex Organic Frameworks. *Angew. Chem. Int. Ed.* **57**, 3985 (2018).
4. Schneemann, A.; Vervoorts, P.; Hante, I.; Tu, M.; Wannapaiboon, S.; Sternemann, C.; Paulus, M.; Wieland, D. C. F.; Henke, S.; Fischer, R. A. Different Breathing Mechanisms in Flexible Pillared-Layered Metal–Organic Frameworks: Impact of the Metal Center. *Chem. Mater*. **30**, 1667 (2018).
5. Dybtsev, D. N.; Chun, H.; Kim, K. *Angew. Chem. Int. Ed*. **43**, 5033 (2004).
6. Sing, K. S. W. Rigid and Flexible: A Highly Porous Metal–Organic Framework with Unusual Guest-Dependent Dynamic Behavior. *Pure Appl. Chem.* **57**, 603 (1985).
7. Fletcher, A. J.; Thomas, M.; Rosseinsky, M. J. Flexibility in metal-organic framework materials: Impact on sorption properties. *J. Solid State Chem.* **178**, 2491 (2005).
8. Taylor, M. K.; Runcevski, T.; Oktawiec, J.; Gonzalez, M. I.; Siegelman, R. L.; Mason, J. A.; Ye, J.; Brown, C. M.; Long, J. F. Tuning the Adsorption-Induced Phase Change in the Flexible Metal–Organic Framework Co(bdp). *J. Am. Chem. Soc.* **138**, 15019 (2016).
9. Alhamami, M.; Doan, H.; Cheng, C.-H. A Review on Breathing Behaviors of Metal-Organic-Frameworks (MOFs) for Gas Adsorption. *Materials,* **7**, 3198 (2014).

10. Barybin, M. V.; Chisholm, M. H.; Dalal, N. S.; Holovics, T. H.; Patmore, N. J.; Robinson, R. E.; Zipse, D. J.; Long-Range Electronic Coupling of MM Quadruple Bonds (M = Mo or W) via a 2,6-Azulenedicarboxylate Bridge. *J. Am. Chem. Soc.* **127**, 15182 (2005).
11. Chisholm, M. H.; Feil, F.; Hadad, C. M.; Patmore, N. J.; Electronically Coupled MM Quadruply-Bonded Complexes (M = Mo or W) Employing Functionalized Terephthalate Bridges: Toward Molecular Rheostats and Switches. *J. Am. Chem. Soc.* **127**, 18150 (2005).
12. Sevov, C. S.; Brooner, R. E. M.; Chénard, E.; Assary, R. S.; Moore, J. S.; Rodrîguez-Lopez, J.; Sanford, M. S.; Evolutionary Design of Low Molecular Weight Organic Anolyte Materials for Applications in Nonaqueous Redox Flow Batteries. *J. Am. Chem. Soc.* **137**, 14465 (2015).
13. Laviron, E.; Roullier, L.; General expression of the linear potential sweep voltammogram for a surface redox reaction with interactions between the adsorbed molecules: Applications to modified electrodes. *J. Electroanal. Chem*. **115**, 65 (1980).

CHAPTER FOUR

Structural and electronic switching of a single-crystal 2D metal–organic framework prepared by chemical vapor deposition

---

This work was co-authored with the following authors and is published under the following citation:

F. James Claire[1], Marina A. Solomos[1], Jungkil Kim[1], Gaoqiang Wang[2,3], Maxime A. Siegler[1], Michael F. Crommie[2,3,4], and Thomas J. Kempa[1,5]*

[1]Department of Chemistry, Johns Hopkins University, Baltimore, MD, USA.

[2]Department of Physics, University of California Berkeley, Berkeley, California, USA

[3]Materials Sciences Division, Lawrence Berkeley National Laboratory, Berkeley, California, USA

[4]Kavli Energy NanoSciences Institute at the University of California Berkeley and the Lawrence Berkeley National Laboratory, Berkeley, California, USA

[5]Department of Materials Science and Engineering, Johns Hopkins University, Baltimore, MD, USA.

Nat. Commun., **2020**, 11, 5524–5531

Supplementary information for this chapter can be found in Appendix C.

4.1 Introduction

In previous chapters, we showed how solvent molecules play a role in the formation of MOF architectures from $Mo_2(INA)_4$ molecular building units. DMF molecules coordinate directly to the 1D linear structure (MF–101) and the DMA molecules reside within the interlayer spacing of 2D structures (MF–102, MF–103).[1,2] However, we can also convert the $Mo_2(INA)_4$ monomer unit into an extended framework structure in a completely solvent free environment.

In this chapter, we will show how we can use chemical vapor deposition (CVD) to produce high-quality MOF single crystals for implementation into devices. Vapor-phase deposition methods are a viable alternative for MOF crystal growth with the potential to overcome some of the aforementioned challenges related to solution-based approaches[3–5]. Used extensively for synthesis of thin films and low-dimensional materials such as graphene, transition metal dichalcogenides, and semiconductor nanowires, gas-phase synthesis was adapted for growth of MOF materials as recently as 2013[6]. Since then, researchers have demonstrated the multistep molecular layer deposition (MLD) of films of UiO-66[7] and copper (II) terephthalate[8], and the conversion of zinc-oxide films to ZIF-8 upon exposure to 2-methylimidazole vapors[9]. While these studies mark notable progress in the use of gas-phase methods for MOF deposition, many challenges remain. First, the multi-step reactions prevalent in these studies increase synthetic overhead and require careful management of intermediates, byproducts, and multiple processing conditions. Second, the coordinated frameworks obtained from these reactions are either amorphous or polycrystalline, and, in many cases, require conversion from a bulk phase. Finally, though often motivated by the desire to incorporate these materials in devices, these studies rarely report device transport measurements. The development of conductive MOFs through judicious selection of metal nodes, incorporation of redox-active ligands, and inclusion of guest species has resulted in

conductivity values as high as 2500 S cm^{-1} [10–17]. Nevertheless, the integration of many candidate MOFs into high performance active devices has been challenging partly due to their poor crystallization characteristics and low stabilities over time. Moreover, concerns over chemical contamination, contact corrosion, and other incompatibilities underscore the issues associated with relying on solution-based methods for integration of MOFs with microelectronic devices. Our method of modular framework assembly using the $Mo_2(INA)_4$ building unit allows us to approach vapor-phase synthesis of MOFs from a new perspective. In this chapter, I will discuss our efforts to produce high-quality active device from MOF single crystals through vapor-phase synthesis.

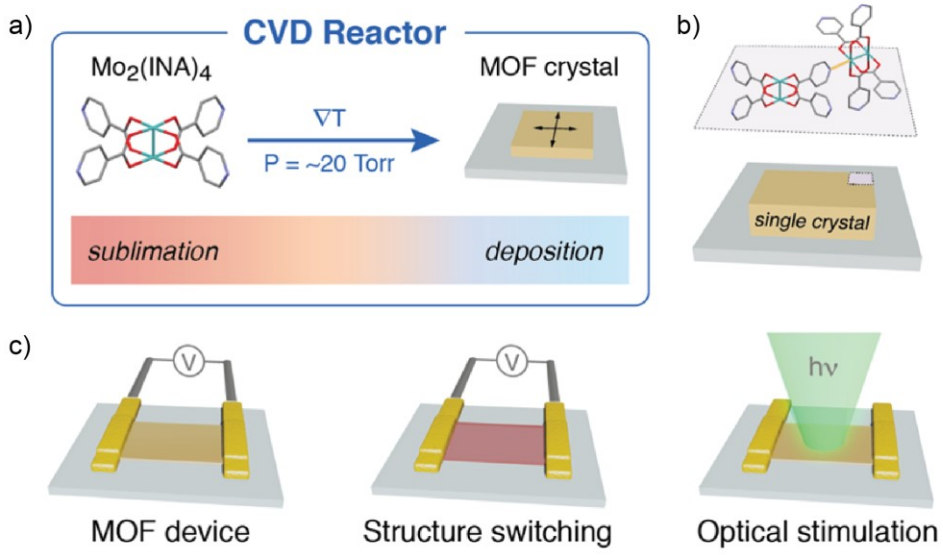

Figure 4.1 | Gas-phase synthesis of large area MOF crystals and their integration into devices. (a) Schematic outlining the process for CVD growth of high-quality MOF single crystals with minimal defects and single crystal character. A MOF precursor, such as $Mo_2(INA)_4$, sublimes under vacuum, is swept by a carrier gas along a thermal gradient, and deposits at lower temperatures to form high-quality MOF single crystals on a range of substrates. (b) Concerted deposition and coordination of $Mo_2(INA)_4$ clusters leads to single MOF crystals covering large areas of the substrate. (c) The large-area single crystals are integrated into devices (left), which are used to monitor the electronic response of the MOF to induced structural changes (middle) and to optical stimulation (right).

4.2 Chemical vapor deposition of single crystal MOF from $Mo_2(INA)_4$

In this study we use chemical vapor deposition to prepare MOF single crystals and then demonstrate reversible switching of their structure and conductivity. The MOF crystals are comprised of $Mo_2(INA)_4$ paddlewheel clusters, which serve as modular building units and have been shown to assemble from the solution-phase into a number of topologies, including linear molecular chain (MF–101) and 2D lattices (MF–102 and MF–103)[1,2]. These paddlewheel clusters resemble a broader class of di-nuclear complexes containing multiply-bonded transition metals[18–22]. Moreover, these clusters are excellent candidate building blocks of an optoelectronically responsive MOF owing to the fact that they exhibit Class III Robin-Day mixed valency and a diversity of optical transitions[23,24]. Notably, we demonstrate the sublimation and concomitant deposition of $Mo_2(INA)_4$ as thin single crystals on glass substrates under high-vacuum CVD conditions (**Figure 4.1**). This single step reaction involves the deposition and coordination of neighboring clusters to yield crystalline extended solids. The exceptional uniformity and quality of the as-grown MOF crystals facilitates their integration and fabrication into active and responsive single crystal devices. To demonstrate the underlying responsiveness of the $Mo_2(INA)_4$ MOF, we monitor *in situ* the conductivity change of the single crystal device as the MOF undergoes structural switching and optical excitation (**Figure 4.1**). Collectively, these data represent the first demonstration of structural and electronic switching behavior within a single crystal device comprised of a MOF prepared solely through gas-phase methods.

We first assessed the potential to grow singly crystalline MOFs using CVD. At a reactor pressure of 20 Torr, $Mo_2(INA)_4$ undergoes sublimation (at 325 °C) and concomitant deposition from the gas phase to form a light red coating on glass substrates (**Figure 4.2a**). Optical images and scanning electron micrographs reveal that this coating consists of many individual rectangular deposits having faceted edges and a mean projected area of 96 μm^2

(**Figures 4.2b**,**c** and **C1**). Extensive growth studies have identified that temperature and pressure conditions of 300–375 °C and 20–40 Torr, respectively, routinely yield near complete substrate coverage with uniform deposits having 10–50 μm edge lengths and thicknesses in the hundreds of nanometers (**Figure C2**). Performing the reaction at slightly higher temperatures or at lower pressures yields polycrystalline films. In an effort to synthesize thinner deposits, we established in our CVD reactor a gradual negative thermal gradient extending 11 cm from the site of sublimation to the site of deposition by shifting the substrate 2 cm further downstream from the precursor. Atomic force microscopy (AFM) of the products of a reaction conducted under these conditions shows that the individual deposits are ∼20 nm thick and exceptionally smooth, with a measured root mean square surface roughness of Rq = 2.9 nm over a 100 μm^2 area (**Figure 4.2d**). Additional AFM data identify discrete steps at the edges of the deposits, suggesting a layered structure (**Figure C3**). Raman spectra acquired on a solid powder of $Mo_2(INA)_4$ before CVD synthesis and on a substrate coated with the aforementioned deposits after CVD growth are largely identical. Notably, a prominent peak at 383 cm^{-1}, which is attributable to the ∼ν(Mo–Mo) mode[19] associated with the quadruple-bonded di-Mo core of the $Mo_2(INA)_4$ cluster, is evident in both spectra (**Figure 4.2e**). These Raman data suggest that the deposits after CVD synthesis are comprised of intact $Mo_2(INA)_4$ clusters.

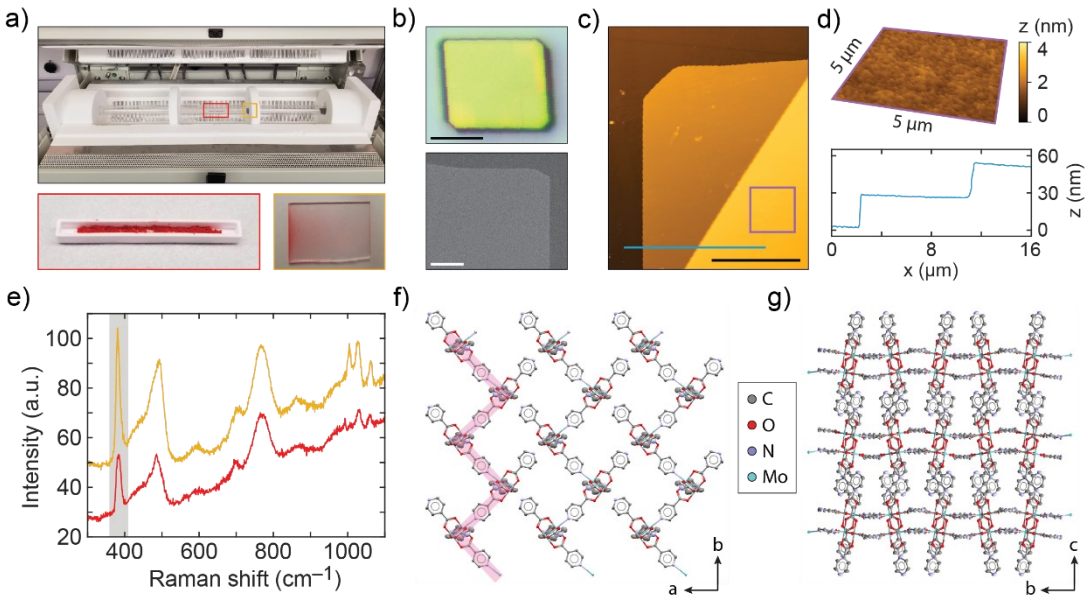

Figure 4.2 | High-quality $Mo_2(INA)_4$ MOF single crystals from gas-phase synthesis. (a) *Top*: Photograph of the quartz tube reaction chamber of our CVD system. The reaction chamber is divided into three independent thermal zones. Reactants flow from left to right through the quartz tube. The red and yellow boxed regions denote the positions of the precursor and deposition substrate, respectively, during the reaction. *Bottom left*: Photograph of the ceramic crucible containing $Mo_2(INA)_4$ powder. *Bottom right*: Photograph of a red film of MF–104 deposited on a glass substrate. The left-hand side of the substrate is nearest the precursor boat. (b) *Top*: Optical image of a single deposit of MF–104. Scale: 10 µm. *Bottom*: Scanning electron micrograph of a corner of one deposit of MF–104. Scale: 1 µm. (c) 2D AFM topographical map of a single thin deposit of MF–104. The purple box and blue line denote approximate regions of interest investigated further in 'd'. A 10 µm × 10 µm region of this AFM map was used to calculate the root mean square surface roughness reported in the text. Scale: 10 µm. (d) *Top*: 3D AFM topographical map encompassing the 25 μm^2 area annotated by the purple box in 'c'. These data exemplify the exceptionally low surface roughness of the CVD grown deposits. *Bottom*: AFM height profile along the path annotated by the blue line in 'c'. (e) Raman spectra of the $Mo_2(INA)_4$ powder precursor (red) and of a single deposit of MF–104 (yellow). The gray band highlights the prominent peak at 383 cm^{-1} attributable to $\tilde{\nu}$(Mo–Mo)[19]. (f) Crystal packing structure of MF–104 viewed down the *c* axis. The pink line highlights one of the 1D zig-zag coordinated chains. (g) Crystal packing structure of MF–104 viewed down the *a* axis showing its layered structure. Hydrogen atoms have been omitted for clarity. Displacement ellipsoids are given at 50 % probability.

The X-ray crystal structure of a single CVD-grown deposit reveals a uniform crystal comprised of "zig-zagging" one-dimensional (1D) chains of partially-coordinated $Mo_2(INA)_4$ paddlewheels (**Figures 4.2f,g** and **C4**). Henceforth, crystals exhibiting this CVD-grown

structure will be referred to as MF–104. This crystal structure is consistent with our reported Raman data, which showed that the deposits are comprised of intact $Mo_2(INA)_4$ paddlewheel clusters. Mo–Mo bond lengths are measured at 2.1143(4) Å throughout the structure. These bond distances are consistent with those previously reported in quadruple bonded Mo_2 cores[2,25]. Individual 1D chains propagate along the *b*-axis, while parallel chains assemble along the *a*-axis. Parallel 1D chains form sheets, which stack in the *c* direction, are spaced 2.835 Å apart, and are offset by half a unit cell (**Figure 4.2g**). Superimposed sheets are separated by a larger distance of 9.617 Å. The as-grown crystals observed by optical microscopy and AFM are comprised of these layered crystalline sheets, and the crystals appear to have their major (002) face oriented parallel to the substrate (**Figure C5**). Notably, though the Mo and N atoms of adjacent 1D chains do not engage in coordination bonds, the distance between these atoms (**Figures 4.2** and **C6**) is such that inter-chain binding may be feasible under appropriate conditions to yield a new framework.

4.3 Vapor-induced, reversible structural switching from MF–104 to MF–102

We next explored the possibility of inducing single crystal structural transitions in our molecular framework. A large single crystal of MF–104 was monitored in the presence of dimethylacetamide (DMA) vapor over the course of seven days. After six hours in the presence of DMA vapor, optical images reveal the appearance of red regions within the initially yellow-orange crystal (**Figure 4.3a**). The size of these red regions grows under continued exposure to DMA vapor, and nearly complete conversion to a dark red crystal is observed in six days. X-ray structural analysis of MF–104 exposed to DMA vapor reveals a crystal comprised of layered 2D lattices of fully coordinated $Mo_2(INA)_4$ clusters, MF–102 (**Figures 4.3b** and **C7**). While the twisting of coordinated $Mo_2(INA)_4$ clusters along the 1D chains in MF–104 likely prevents Mo–N bond formation between adjacent parallel 1D chains,

the introduction of DMA may facilitate inter-chain binding to form MF–102. It is possible that entry of DMA into the crystal lattice accommodates a structural adjustment sufficient to allow Mo–N bond formation across adjacent 1D chains, ultimately leading to formation of the fully coordinated 2D lattice with disordered solvent molecules situated within square sub-cells.

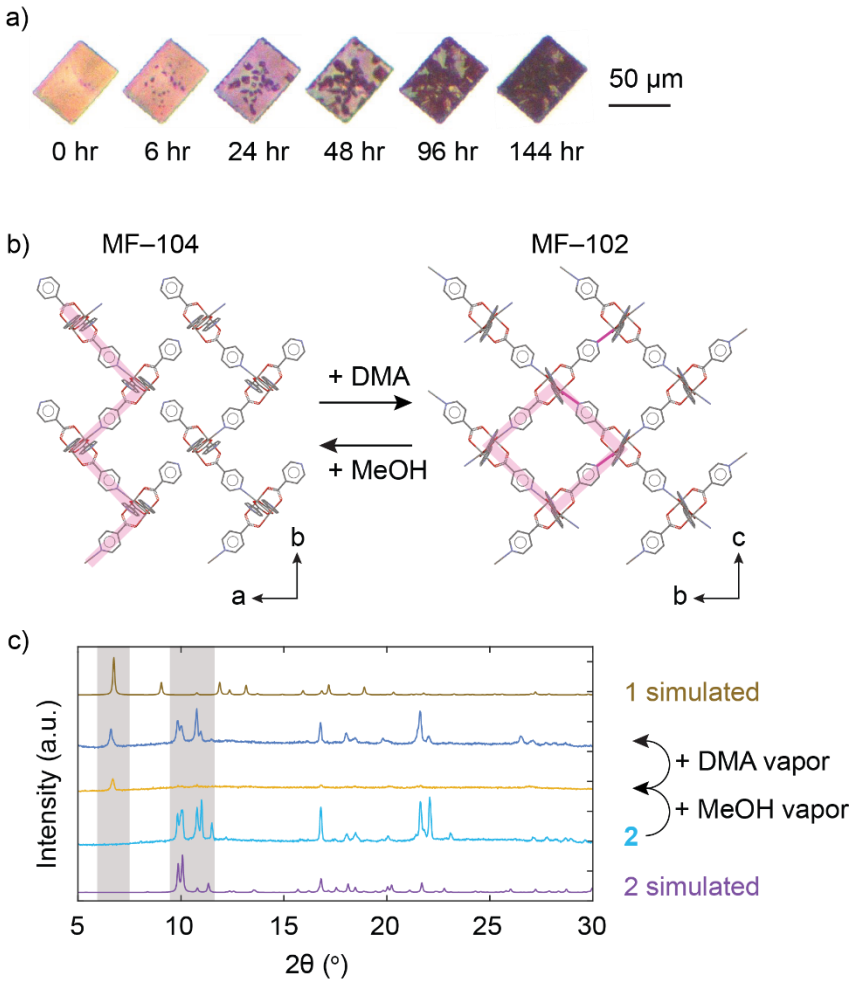

Figure 4.3 | Reversible structural switching between MF–104 and MF–102. (a) Photographs of a single crystal of MF–104 exposed over time to dimethylacetamide (DMA) vapor. (b) Single crystal structures of MF–104 (left) and of MF–102 (right) showing how exposure to DMA and methanol can facilitate interconversion between the two structures. Solvent molecules have been omitted for clarity. (c) Simulated and experimental powder XRD scans of bulk samples of MF–104 and MF–102 used to demonstrate reversible conversion between the MOF structures.

We subsequently assessed the reversibility of structural transitions involving our as-grown and converted MOFs. Bulk samples of MF–102 were prepared to facilitate conversion

trials. The powder X-ray diffraction (pXRD) scan of a bulk sample of MF–102 (**Figure 4.3c**) contains the same principal peaks between 9.7˚ and 12.4˚ as the pXRD scan of MF–102 obtained through routine simulation from the single crystal structure of MF–102 (**Figure 4.3c**). These data verify that bulk quantities of MF–102 are representative of the single crystal structure of MF–102. Subsequently, a 10 mg sample of MF–102 was exposed to methanol vapor for 48 hours. A dominant peak at 6.7˚ is apparent in the pXRD scan of this methanol exposed sample. A peak at this same 2θ angle is present in the pXRD scan of MF–104 obtained through routine simulation from the single crystal structure of MF–104. These data suggest that MF–102 converts to MF–104 upon exposure to methanol. The 6.7˚ peak likely corresponds to the aforementioned (002) plane of MF–104, because this is the major crystal face in the highly oriented CVD-grown crystals (**Figure C5**). Heat capacity measurements on dried samples of MF–104 show no additional transitions between 2–300K (**Figure C9**). Finally, this same sample was exposed to DMA vapor for 48 hours and its pXRD scan was acquired (**Figure 4.3c**). The peaks within this scan are similar (traces of MF–104 remain) to those found in the scan of MF–102 after it was first converted from MF–104 by exposure to DMA. The small differences between 10˚ and 12˚ and emergent peaks near 22° in the two pXRD scans for the 2D phases can be attributed to minor structural differences arising from different and possibly incomplete DMA incorporation during separate conversion cycles (**Figure C10**). Together, these data show that MF–102 can be converted to MF–104 through exposure to methanol and then back to MF–102 through exposure to DMA, thereby showing the reversible and cyclic structural transitions our $Mo_2(INA)_4$ MOF system is capable of.

4.4 Integration of MF–104 single crystals into active device architectures

4.4.1 Fabrication of single crystal MOF devices

Our identification of reversible structural transitions inspired us to look for other examples of switching behavior in our MOF. To explore the responsive properties of our MOF further, we undertook fabrication of high-quality devices on single crystals of MF–104. As noted above, the as-grown crystals are singly-crystalline, are absent of solvent, and have uniformly flat surfaces. Together, these features facilitate the fabrication of high-quality devices which permit the measurement of the intrinsic transport properties of the molecular framework. Large single crystals of MF–104 were transferred *via* mechanical exfoliation to a $Si_3N_4/SiO_2/Si$ substrate. To make a device, two Au/Ti contacts were selectively fabricated atop either side of a transferred crystal through the use of electron-beam lithography and thermal evaporation (**Figure 4.4a**). An AFM line profile of the resulting device confirms that the crystal is 247 nm thick and has a uniform topography (**Figure C11**).

4.4.2 Electronic response during structural switching

Current-voltage (*I*-*V*) measurements performed on the single crystal device of MF–104 reveal a linear dependence of drain current on source-drain voltage with an extracted conductivity value of 2.25×10^{-8} S cm^{-1} (**Figures 4.4b** and **C11**). This value is comparable to conductivity values reported for electrically conductive MOFs and represents one of the few examples of transport measurements taken at the level of a single MOF crystal[10,26–30]. Notably, when single-crystal devices of MF–104 were exposed to the conditions previously used to convert MF–104 to MF–102, a higher conductivity value of 6.22×10^{-7} S cm^{-1} was observed (**Figures 4.4b** and **C11**). This nearly 30-fold increase in conductivity is likely due to the significant increase in carrier percolation paths in going from a partially- to a fully-coordinated network of $Mo_2(INA)_4$ clusters. The occurrence of a large conductivity switch

during absorption of DMA vapor suggests the promise of our MOF platform in chemical sensing. To the best of our knowledge, these data represent the first *in situ* measurements of electronic property change in a single crystal MOF undergoing a structural transition in response to an external stimulus.

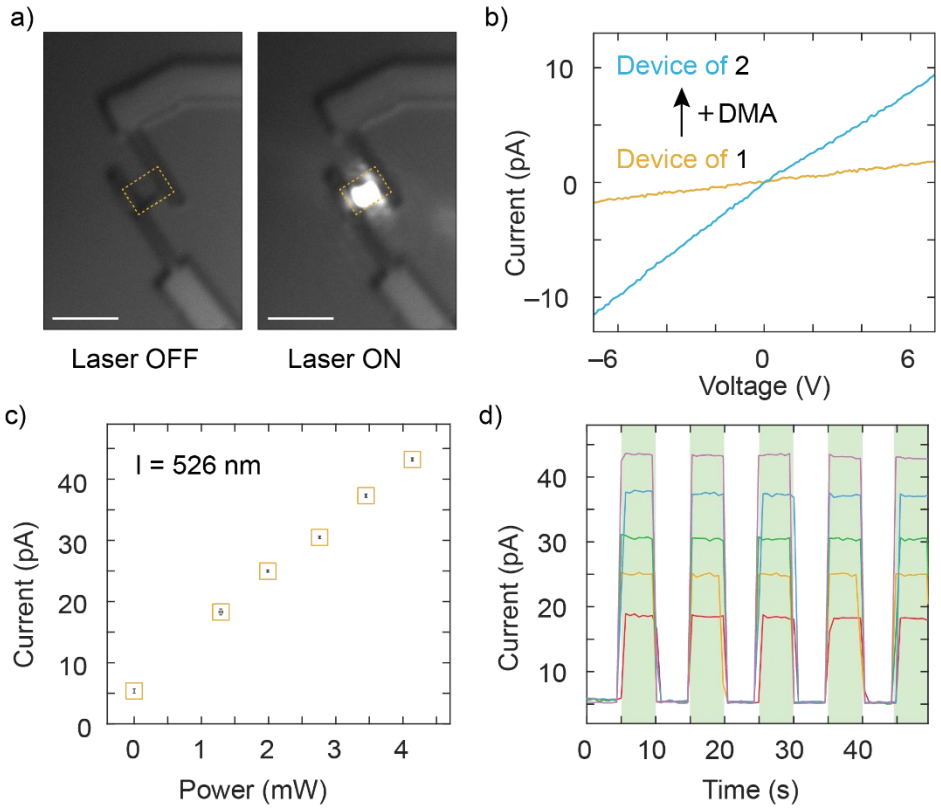

Figure 4.4 | Stimuli responsive conductivity of $Mo_2(INA)_4$ single crystal MOF devices. (a) Optical images collected during measurement of a device fabricated on a single crystal of MF–104. The crystal boundary is highlighted by the dashed gold box and bright diffraction-limited laser spot is evident in the right image. Scale: 5 μm. (b) Current-voltage characteristics of a single crystal device of MF–104 (yellow) and of a single crystal device of MF–102 (blue) prepared through exposure to DMA. (c) Photocurrent generated by a single crystal device of MF–104 when illuminated with a 526 nm laser at 1.29 mW, 1.99 mW, 2.76 mW, 3.45 mW, and 4.14 mW. The device source-drain bias was held constant at 20 V. Error bars denote standard deviation. (d) Photocurrent switching behavior of a single crystal device of MF–104 subjected to periodic laser illumination at 5 s intervals (green highlighted regions). Device switching behavior was assessed at 1.29 mW (red), 1.99 mW (orange), 2.76 mW (green), 3.45 mW (blue), and 4.14 mW (purple).

4.4.3 Electronic response during optical stimulation

To further elucidate the responsive characteristics of our MOF devices, we assessed their response to optical illumination. We irradiated a single crystal device of MF–104 with the output of a 526 nm diode laser and measured its current response (at V_{SD} = 20 V) as a function of laser power (**Figure 4.4c**). When not illuminated and kept in a rigorously darkened enclosure, the MOF crystal device produced a "dark" current of 5.39 pA. When illuminated, the device produced a current with linear dependence on laser power, with irradiation at 4.14 mW yielding an 8-fold larger current than the "dark" current. Moreover, periodic illumination of the device at 5-s intervals yielded reversible cycling of photocurrent at laser powers of 1.29, 1.99, 2.76, 3.45, and 4.14 mW (**Figure 4.4d**). The device photocurrent output for a particular laser power did not deviate by more than 2.7% between illumination cycles and the device returned to within 6.4% of its "dark" current value whenever not illuminated. In a study of a distinct but related framework comprised of $Mo_2(INA)_4$ clusters, we found evidence of dimer-like metal-to-ligand charge transfer (MLCT) states at energies of 2.19 eV (566 nm)[1]. The photocurrent produced by our material may arise from excitation of such MLCT states, which are created through a lifting of the degeneracy of the single cluster orbitals. These data establish the robust photocurrent switching properties of our single crystal MOF device and suggest the promise of this and related MOF systems in photodetection applications.

4.5 Scanning tunneling microscopy analysis of framework assembly

Finally, we sought to inspect the molecular-level assembly of $Mo_2(INA)_4$ from the gas phase by scanning tunneling microscopy (STM). A single layer 2D $Mo_2(INA)_4$ MOF was grown on a Au(111) surface in ultra-high vacuum by thermal deposition and annealing. An STM topographical map of a Au surface containing deposited $Mo_2(INA)_4$ clusters before annealing

shows that the clusters are randomly distributed and are present in different orientations, as evidenced by the different intensities they elicit in the STM map (**Figure 4.5**). After annealing, the $Mo_2(INA)_4$ clusters form a highly-ordered monolayer characterized by alternating 90°-rotated oval features that form a square lattice with associated lattice constants a = b = 10.8 ± 0.4 Å (**Figures 4.5** and **C12**). Notably, the distance between the centroids of two neighboring clusters (centroid here is defined as the midpoint of the Mo–Mo bond axis) in the crystal structure of MF–102 ranges between 10.535–10.551 Å. The order and spacing of the features in the STM map are consistent with the arrangement of $Mo_2(INA)_4$ clusters in the crystal structures of MF–104 and MF–102, and with the distance between $Mo_2(INA)_4$ clusters in the structure of MF–102, respectively. These data suggest that growth at elevated temperatures is sufficient to facilitate the organization of randomly deposited $Mo_2(INA)_4$ clusters into our reported MOF phases. Facile deposition and ordering of individual $Mo_2(INA)_4$ clusters under gas-phase synthesis conditions reinforces the potential for use of CVD methods in the preparation of flat, uniform, and single-molecule thick MOFs suitable for detailed study.

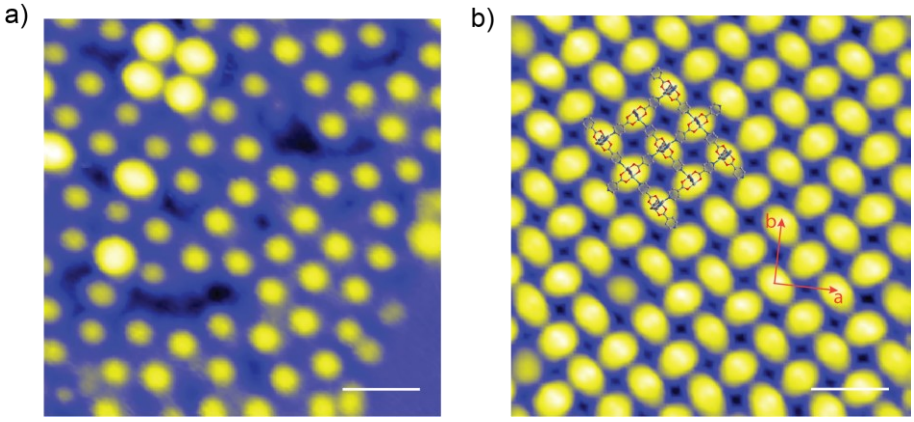

Figure 4.5 | STM topography images of a $Mo_2(INA)_4$ monolayer on a Au(111) surface. (a) STM image (bias V = 0.05 V, tunneling current I = 5 pA) of $Mo_2(INA)_4$ clusters deposited on Au(111) before annealing. Scale: 2.0 nm. (a) STM image (V = 2 V, I = 10 pA) of a 2D $Mo_2(INA)_4$ MOF monolayer on Au(111) after annealing (crystal structure MF–102 is superimposed). Scale: 2.0 nm.

4.6 Conclusions

We have demonstrated the growth of high-quality single crystals of a responsive MOF using gas-phase methods. We show that the paddlewheel cluster, $Mo_2(INA)_4$, sublimes as a molecular unit to form an extended framework in the absence of solvent and is capable of assembly into a truly two-dimensional (2D), single-molecule thick MOF. Moreover, we show that the crystal structure of this material can be reversibly switched to and from a layered 2D framework upon exposure to solvent vapors. Devices fabricated from single crystals of MF–104 show appreciable electronic conductivity. Notably, we measured *in situ* a 30-fold increase in conductivity as a single-crystal device underwent conversion to a 2D topology. Furthermore, we found a significant and cyclable photocurrent response for single-crystal devices. We also note that our MOFs exhibit concurrent responses in their conductivity and structure at room temperature and can therefore be distinguished from many of the previously studied responsive molecular crystal and polymer systems. We foresee broader use of gas-phase methods, including CVD, for the preparation of high-quality molecular frameworks (*e.g.* MOFs and COFs), and the prospect for facile integration of these diverse materials into devices, including sensors, actuators, and detectors.

REFERENCES

1. Li, M. M.; Claire, F. J.; Solomos, M. A.; Tenney, S. M.; Ivanov, S. A.; Siegler, M. A.; Kempa, T. J. Molecular chains of coordinated dimolybdenum isonicotinate paddlewheel clusters. RSC Adv. 9, 16492–16495 (2019).
2. Claire, F. J.; Li, M. M.; Tenney, S. M.; Siegler, M. A.; Wagner, J. S.; Hall, A. S.; Kempa, T J.

metal–organic frameworks: State-of-the-art and future Directions. *Chem. - A Eur. J.* **22**, 14452–14460 (2016).

4. Stassin, T. *et al.* Vapour-phase deposition of oriented copper dicarboxylate metal–organic framework thin films. *Chem. Commun.* 3–6 (2019). doi:10.1039/C9CC05161A
5. Krishtab, M. *et al.* Vapor-deposited zeolitic imidazolate frameworks as gap-filling ultra-low-k dielectrics. *Nat. Commun.* **10**, 3729 (2019).
6. Salmi, L. D. *et al.* Studies on atomic layer deposition of MOF-5 thin films. *Microporous Mesoporous Mater.* **182**, 147–154 (2013).
7. Lausund, K. B. & Nilsen, O. All-gas-phase synthesis of UiO-66 through modulated atomic layer deposition. *Nat. Commun.* **7**, 1–9 (2016).
8. Ahvenniemi, E. & Karppinen, M. Atomic/molecular layer deposition: A direct gas-phase route to crystalline metal-organic framework thin films. *Chem. Commun.* **52**, 1139–1142 (2016).
9. Stassen, I. *et al.* Chemical vapour deposition of zeolitic imidazolate framework thin films. *Nat. Mater.* **15**, 304–310 (2016).
10. Xie, L. S. *et al.* Tunable mixed-valence doping toward record electrical conductivity in a three-dimensional metal-organic framework. *J. Am. Chem. Soc.* **140**, 7411–7414 (2018).
11. Talin, A. A. *et al.* Tunable electrical conductivity in metal-organic framework thin-film devices. *Science.* **343**, 66–70 (2014).
12. Bhardwaj, S.K. *et al.* An overview of different strategies to introduce conductivity in metal-organic frameworks and miscellaneous applications thereof. *J. Mater. Chem. A* **6**, 14992-15009 (2018).
13. Calvo, J.J., Angel, S.M. & So, M.C. Charge transport in metal-organic frameworks for electronics applications. *APL Mater.* **8**, 050901-01-050901-10 (2020).

14. Lee, J.M., Otake, K. & Kitagawa, S. Transport properties in porous coordination polymers. *Coord. Chem. Rev.* **421**, 213447 (2020).
15. Xie, L.S., Skorupskii, G. & Dincă, M. Electrically conductive metal-organic frameworks. *Chem. Rev.* **120**, 8536-8580 (2020).
16. Huang, X. *et al.* 2-dimensional π-d conjugated coordination polymer with extremely high electrical conductivity and ambipolar transport behaviour. *Nat. Commun.* **6**, 1–8 (2015).
17. Jin., Z. *et al.* Solution-processed transparent coordination polymer electrode for photovoltaic solar cells. *Nano Energy* **40**, 376-381 (2017).
18. Chisholm, M. H. & Macintosh, A. M. Linking multiple bonds between metal atoms: Clusters, dimers of 'dimers', and higher ordered assemblies. *Chemical Reviews* **105**, 2949–2976 (2005).
19. Chisholm, M. H. Metal to metal multiple bonds in ordered assemblies. *Proc. Natl. Acad. Sci.* **104**, 2563–2570 (2007).
20. Cotton, F. A. *et al.* Fully localized mixed-valence oxidation products of molecules containing two linked dimolybdenum units: An effective structural criterion. *J. Am. Chem. Soc.* **125**, 12945–12952 (2003).
21. Chisholm, M. H. & Lear, B. J. M2δ to ligand π-conjugation: Testbeds for current theories of mixed valence in ground and photoexcited states of molecular systems. *Chem. Soc. Rev.* **40**, 5254–5265 (2011).
22. Kubiak, C. P. Inorganic electron transfer: Sharpening a fuzzy border in mixed valency and extending mixed valency across supramolecular systems. *Inorg. Chem.* **52**, 5663–5676 (2013).
23. Cotton, F. A., Donahue, J. P. & Murillo, C. A. The first supramolecular assemblies comprised of dimetal units and chiral dicarboxylates. *Inorg. Chem. Commun.* **5**, 59–63

(2002).

24. Cotton, F. A., Lin, C. & Murillo, C. A. Supramolecular arrays based on dimetal building units. *Acc. Chem. Res.* **32**, 769–771 (2001).
25. Cotton, F. A., Mester, Z. C. & Webb, T. R. Dimolybdenum tetraacetate. *Acta Crystallogr. Sect. B* **B30**, 2768–2770 (1974).
26. Hmadeh, M. *et al.* New porous crystals of extended metal-catecholates. *Chem. Mater.* **24**, 3511–3513 (2012).
27. Park, S. S. *et al.* Cation-dependent intrinsic electrical conductivity in isostructural tetrathiafulvalene-based microporous metal-organic frameworks. *J. Am. Chem. Soc.* **137**, 1774–1777 (2015).
28. Wang, Q.-X. *et al.* Rigid pillars and double walls in a porous metal-organic framework: single-crystal to single-crystal, controlled uptake and release of iodine and electrical conductivity. *J. Am. Chem. Soc.* **132**, 2561–2563 (2010).
29. Day *et al*. Single crystals of electrically conductive two-dimensional metal–organic frameworks: structural and electrical transport properties. *ACS Cent. Sci.* **5**, 1959–1964 (2019).
30. Sun, L., Park, S. S., Sheberla, D. & Dincă, M. Measuring and reporting electrical conductivity in metal-organic frameworks: Cd2(TTFTB) as a case study. *J. Am. Chem. Soc.* **138**, 14772–14782 (2016).

CHAPTER FIVE

Conclusions and Outlook: Expanding the possibilities for modular synthesis of metal-organic frameworks

5.1 Conclusions: Progress towards active MOF devices

Our success with the assembly of novel molecular frameworks from the modular building unit $Mo_2(INA)_4$ suggests a number of strategies and opportunities for realizing a broad family of new MOFs with responsive properties. The intrinsic features of our molecular building unit, namely the presence of adaptable binding motifs and redox-active Mo_2 moieties, allow us to create a variety of functional materials from the same building unit. The 1D linear MF–101 shows that the intrinsic properties of the material are dependent on the architecture of the extended framework as the absorption spectra of MF–101 are distinct from those of the $Mo_2(INA)_4$ monomer.[1] Redox activity in MF–102 provided evidence that it may be possible to tune charge transport within this class of MOFs. Additionally, the flexible layered structures of MF–102 and MF–103 signaled that these MOFs are structurally responsive towards changes in the nature and amount of solvent or gas present within the porous structure.[2] Finally, we developed a novel synthetic process to produce high-quality MF–104 single crystals which can be integrated into devices. These crystalline molecular frameworks, when fashioned into devices, were subsequently shown to be structurally and electronically responsive to various external stimuli.[3]

In order to realize active device architectures using molecular frameworks, we have met two important criteria:

3. *MOFs were designed with structures and properties that can be manipulated by external stimuli.*
4. *Vapor-phase synthetic methods produced high-quality crystalline MOFs for seamless integration into device architectures.*

We designed MOFs that are responsive to multiple stimuli. Introducing new solvent environments will modify the 1D MF–101 structure into a 2D MF–102 structure which can subsequently be changed to MF–104 and back to MF–102 through exposure to solvent

vapors. In addition, the layered structure of the 2D MOF, MF–102, is flexible in such a way to allow for the anomalous adsorption and desorption of CO_2. When MF–104 is stimulated by a laser, the conductivity of the MOF reversibly increases. We are able to measure the single-crystal conductivity of the MOF due to our novel synthetic method which produces high-quality single crystals through chemical vapor deposition. This synthetic method is made possible by the $Mo_2(INA)_4$ building unit which contains both the organic and metal components necessary to form a MOF. The $Mo_2(INA)_4$ unit remains intact when sublimated, allowing us to directly synthesize a MOF through vapor-phase methods.

5.2 Modular synthesis of metal-organic frameworks

All four of the frameworks we have synthesized to-date are derived from the $Mo_2(INA)_4$ molecular cluster, but this modular method of synthesizing MOF from a molecular building unit has the potential to be expanded to a wide variety of building units. The $Mo_2(INA)_4$ molecular cluster contains both the metal center and organic ligands necessary to form MOF architectures. This concept can be extended to a variety of metal-ligand combinations to create a series of modular units that can assemble into unique frameworks.

5.2.1 Mixed-ligand Mo_2 paddlewheel molecules

Perhaps the most readily apparent building units that could work for this method of MOF synthesis are derivatives of the $Mo_2(INA)_4$ paddlewheel molecule. Maintaining the same dimetallic paddlewheel structure and simply exchanging some or all of the ligands can yield new molecular building units with the same coordination environments to produce similar extended framework architectures. In each of the $Mo_2(INA)_4$ MOFs, at least two INA ligands on each paddlewheel do not take part in the extended coordination of the framework. In MF–102, for example, the two INA ligands perpendicular to the plane of the 2D layers do not

coordinate through their INA nitrogen atoms. One can imagine exchanging these undercoordinated INA ligands for a new carboxylate ligand with different steric bulk than INA which would allow the MOF to maintain its 2D coordination but would modify the stacking properties of the 2D layers. Synthesizing mixed-ligand paddlewheels with either 2,4,6-triisopropyl benzoate (TiPB) or benzene carboxylate (BA) and INA at a 1:1 could produce new 2D MOFs with the same coordination structure as MF–102, but with new layering properties (**Figure 5.1**). Lattice expansion could also be induced by increasing the distance between the carboxylate and pyridine moieties within the coordinating ligand. Using a ligand such as 4(4-pyridinyl)benzoate (PBA) to replace INA could produce a new MOF structure with greater distances between the Mo_2 centers (**Figure 5.1**). Any of these changes would likely lead to interesting MOF variants with intriguing properties.

5.2.2 Soft-ligand M_2 paddlewheel molecules

Similarly, one could substitute the ligands or metal to produce paddlewheel molecules with unique metal–ligand interactions. Substituting the oxygen atoms in INA with sulfur atoms would produce a softer ligand, changing the MLCT characteristics of the cluster and therefore altering charge transport within the extended framework. This could enable the formation of more highly conductive MOFs due to the higher degree of orbital overlap between the ligands and metal ions. Replacing INA with 4-pyridinyl dithiobenzoate (4-pyrTB) could produce a series of new MOFs with higher conductivities than MF–102 and MF–104. Further modification of MLCT characteristics can be achieved through metal centers other than Mo_2, such as W_2 or Cr_2 (**Figure 5.1**).

5.2.3 Novel precursors for CVD synthesis

The CVD synthesis of MF–104 is the first example of direct MOF synthesis in a one-step vapor-phase process. The molecular design of $Mo_2(INA)_4$ removes the issue of incommensurate sublimation conditions for the individual components that make up MOFs. Without the molecular building unit, it is difficult to produce conditions under which both the organic ligand and metal clusters will be stable in the vapor phase simultaneously. In order for this method of synthesis to be useful to a broader class of MOFs, creative design of molecular precursors is necessary. One can implement the strategy of using heterotopic ligands like INA which coordinated strongly on one end (carboxylate) and more weakly on the other end (pyridinyl N). Surrounding a metal cluster with such ligands could produce a molecular species that exists as a stable monomer and is capable of readily assembling into an extended framework. The use of labile coordinating molecules (i.e. DMF) can be used to maintain stable monomer units in solution which can then assemble into MOF through removal of the solvent/protecting group.

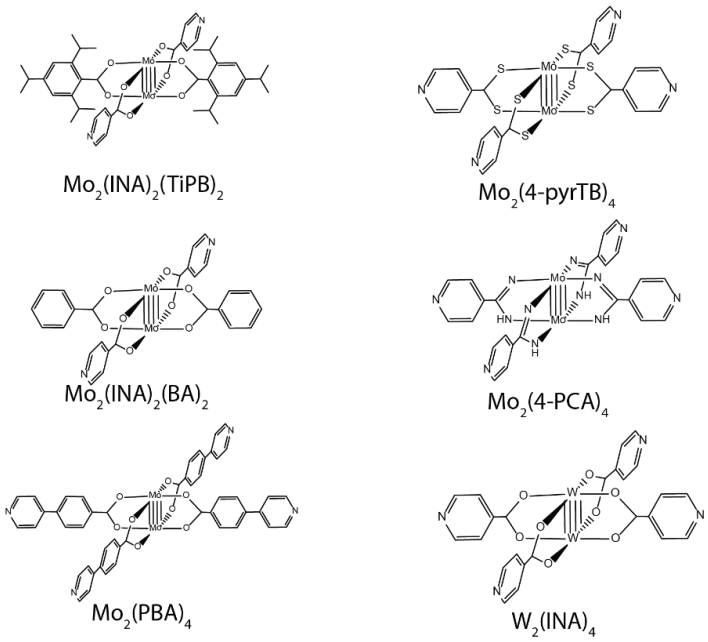

Figure 5.1 | Potential molecular building units derived from the $Mo_2(INA)_4$ paddlewheel structure.

5.3 Continuing device property measurements

There is opportunity for further investigation into the electronic properties of these MOFs. More complex device architectures can be fabricated incorporating MF–104 single crystals to gain insight into the mechanism of charge transport within the framework and its responsive properties.

5.3.1 Direct device fabrication

Using our CVD synthesis method, we are able to directly deposit MOF single crystals onto existing electrode contacts to produce basic device architectures. A simple array of Au contacts can be defined by photolithography onto a Si/SiO_2 substrate which can subsequently be used as the deposition substrate for a CVD synthesis. Single crystals of MF–104 that grow between neighboring Au contacts function as simple two-probe devices for conductivity measurements (**Figure 5.2**). This method for creating devices simplifies the device fabrication process allowing for higher throughput with greater cost efficiency. Our previous method of device fabrication involved exposing the MOF crystals to electron beam irradiation during lithography, high temperatures during thermal evaporation of metal contacts, and potentially damaging solvents during development and removal of the polymer resist. Each of these steps could be damaging to less stable molecular crystals, compared to their inorganic counterparts. If we are to expand our studies to new molecular frameworks and MOFs, this process of direct deposition will be valuable towards investigating electronic conductivity characteristics of materials that are not suitable for more intensive fabrication processes.

5.3.2 Anisotropic conductivity

In our measurements of the conductivity of MF–104 converted to MF–102, we observe a significant increase in conductivity in the more highly coordinated MF–102. This observation could be evidence that the extent of coordination within the framework affects charge transport. The structure of MF–104 has intrinsic anisotropy within the 2D stacked layers. In the *a* direction there is a continuous coordinated chain of zig-zagging $Mo_2(INA)_4$ clusters. In the *b* direction the neighboring chains do not connect through coordination bonds. We could measure the conductivity in each of these directions by fabricating devices with four points of contact on a MOF crystal. This concept can also be used to measure the out of plane conductivity by connecting electrode contacts to the top and bottom of the crystal. It has been shown in other 2D MOF systems that the out of plane conductivity is significantly less than in the plane of the 2D sheets. A more detailed understanding of the charge transport mechanism within the crystals can inform design changes for future MOF architectures for improved electronic performance.

5.3.3 Electrochemically gated field effect transistors

Our work to-date has shown that MF–102 is redox-active and electrically conductive. One potential strategy to take advantage of these two properties in tandem is to fabricate an electrochemically gated field-effect transistor (FET) using MOF single crystals (**Figure 5.2**). With this device architecture, we could analyze the redox-state-dependent conductivity of MOF crystals.

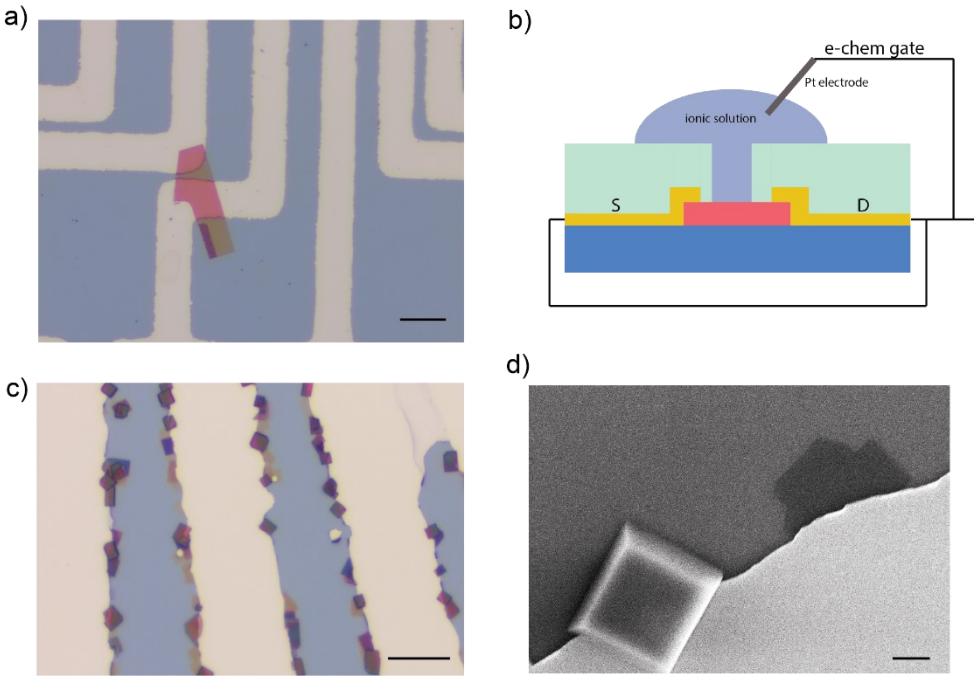

Figure 5.2 | (a) Direct deposition of MF–104 single crystal onto photolithographically defined Au electrode patterns. Scale bar 20 μm. (b) Electrochemically gated FET schematic. MOF crystal (red) is deposited on a SiO_2 surface (blue) and contacted by two Au electrodes (gold). Polymer resist (green) protects the electrodes from contacting the electrolyte solution (purple) through which the redox state of the MOF crystal is modulated. (c) Optical image and (d) SEM micrograph of MF–104 crystals nucleating on Au edges. Scale bars 20 μm and 2 μm.

5.4 Approaching true 2D MOF monolayers

When working with 2D materials, the end goal is almost always to reach the true 2D monolayer limit to achieve unique properties of low-dimensional materials. Many methods have been attempted to produce 2D monolayer MOFs, including chemical and mechanical exfoliation of bulk, layered MOFs. We believe our vapor-phase synthetic method provides an opportunity for directly producing MOF monolayers without need for exfoliation.[10–14] Under growth conditions of 40 Torr and 300 °C, MF–104 crystals preferentially nucleate on the edges of Au on Si/SiO_2 substrates. Crystals nucleated on Au have been measured to be as thin as 10 nm, which is approaching only few-layer thick MOF crystals. Further study of the nucleation and growth mechanism of MOF crystals under these conditions could lead to a promise new method for direct growth of 2D monolayer MOFs.

Modular synthesis of this series of molecular frameworks from the $Mo_2(INA)_4$ molecular building unit provides many exciting opportunities for the future of MOF research. My work in the Kempa Group has laid the foundation for many new developments in molecular framework chemistry. The concept of molecular building units can be expanded to a wide variety of new MOF systems to develop frameworks that exhibit structurally responsive behavior. Sufficiently stable molecular clusters can undergo sublimation and subsequent deposition to produce high-quality MOF single crystals through vapor-phase methods, allowing for integration into active devices. I am excited by the possibilities of new structures and properties to be discovered for $Mo_2(INA)_4$-based MOFs and the potential for new MOF systems to be developed from modular building units.

REFERENCES

1. Li, M. M.; Claire, F. J.; Solomos, M. A.; Tenney, S. M.; Ivanov, S. A.; Siegler, M. A.; Kempa, T. J. Molecular chains of coordinated dimolybdenum isonicotinate paddlewheel clusters. RSC Adv. 9, 16492–16495 (2019).
2. Claire, F. J.; Li, M. M.; Tenney, S. M.; Siegler, M. A.; Wagner, J. S.; Hall, A. S.; Kempa, T J. Hierarchically ordered two-dimensional coordination polymers assembled from redox-active dimolybdenum clusters. *J. Am. Chem. Soc.* **140**, 10673–10676 (2018).
3. Claire, F. J.; Solomos, M. A.; Kim, J.; Wang, G.; Siegler, M. A.; Crommie, M. F.; Kempa, T. J. Structural and electronic switching of a single crystal 2D metal-organic framework prepared by chemical vapor deposition. *Nat. Commun.* **11** (1), 5524 (2020)
4. Solomos, M. A., Claire, F. J. & Kempa, T. J. 2D Molecular Crystal Lattices: Advances in their Synthesis, Characterization, and Application. *J. Mater. Chem. A* **7**, 23537-23562 (2019).

5. Hendon, C. H.; Rieth, A. J.; Korzynski, M. D.; Dincă, M. Grand Challenges and Future Opportunities for Metal–Organic Frameworks. *ACS Cent. Sci.* **3**, 554 (2017).
6. Ko, M., Mendecki, L. & Mirica, K. A. Conductive two-dimensional metal-organic frameworks as multifunctional materials. *Chem. Commun.* **54**, 7873–7891 (2018).
7. Allendorf, M.D. *et al.* Electronic devices using open framework materials. *Chem. Rev.* **120**, 8581-8640 (2020).
8. Stassen, I., De Vos, D. & Ameloot, R. Vapor-Phase Deposition and Modification of Metal–Organic Frameworks: State-of-the-Art and Future Directions. *Chem. - A Eur. J.* **22**, 14452–14460 (2016).
9. Colson, J. W. *et al.* Oriented 2D covalent organic framework thin films on single-layer graphene. *Science.* **332**, 228–232 (2011).
10. Tan, C., Cao, X., Wu, X. J., He, Q., Yang, J., Zhang, X., Chen, J., Zhao, W., Han, S., Nam, G. H., Sindoro, M. & Zhang, H. Recent Advances in Ultrathin Two-Dimensional Nanomaterials. *Chem. Rev.* **117**, 6225–6331 (2017).
11. Meng, Z., Stolz, R. M., Mendecki, L. & Mirica, K. A. Electrically-transduced chemical sensors based on two-dimensional nanomaterials. *Chem. Rev.* **119**, 478–598 (2019).
12. Furukawa, H., Cordova, K. E., O'Keeffe, M. & Yaghi, O. M. The chemistry and applications of metal-organic frameworks. *Science.* **341**, (2013).
13. Li, S., Yang, K., Tan, C., Huang, X., Huang, W. & Zhang, H. Preparation and applications of novel composites composed of metal-organic frameworks and two-dimensional materials. *Chem. Commun.* **52**, 1555–1562 (2016).
14. Liu, J., Yu, H., Wang, L., Deng, Z., Naveed, K. ur R., Nazir, A. & Haq, F. Two-dimensional metal-organic frameworks nanosheets: Synthesis strategies and applications. *Inorganica Chim. Acta* **483**, 550–564 (2018).

APPENDIX A

SUPPLEMENTARY INFORMATION FOR CHAPTER TWO

MATERIALS and METHODS

General: All glassware was cleaned and oven-dried prior to usage. All solvents were thoroughly degassed under inert atmosphere (N_2). Schlenk line techniques were used in the syntheses of molybdenum (II) acetate and molybdenum (II) isonicotinate.

Synthesis of Molybdenum (II) Acetate ($Mo_2(O_2CCH_3)_4$)[1,2]: A 500-mL round-bottom flask was charged with molybdenum hexacarbonyl (3.0 g, 11 mmol). To this flask, acetic acid (100 mL), acetic anhydride (20 mL), and hexane (5 mL) were added. The solution was refluxed at 130 °C for 20 hours with stirring. The solution turned brown, and a bright yellow crystalline solid precipitated. The yellow solid was filtered under N_2 and washed with ethanol. The product was dried under vacuum and stored under N_2 at −20 °C. Yield: 37.1%

Synthesis of Molybdenum (II) Isonicotinate ($Mo_2(INA)_4$•DMF): A solution of $Mo_2(O_2CCH_3)_4$ (0.250 g, 0.584 mmol) and isonicotinic acid (0.712 g, 5.79 mmol) in 50 mL anhydrous dimethylformamide (DMF) was prepared in a 100-mL Schlenk flask under an N_2 atmosphere. To this solution, acetic acid (0.033 mL, 0.574 mmol) was added. The red solution was refluxed at 120 °C for two days while stirring at 300 rpm. When this reaction is performed with stirring speed of 60 rpm, single crystals large enough for x-ray diffraction studies are deposited on the sidewalls of the flask, at the surface of the solution. The bright red product was filtered under N_2, washed with DMF, and dried under vacuum. The product was stored under N_2. Yield: 62%. Elemental analysis measures 42.28% C, 3.00% H, 9.12% N, and 25.74% Mo (theoretical values: 43.04% C, 3.08% H, 9.30% N, and 25.47% Mo).

Mass spectroscopy: A solution of JHMF–101 (5 mg) in 2 mL dimethyl-sulfoxide (DMSO) was diluted in 20 mL of acetonitrile. This solution was analyzed in positive mode ESI-MS on a Thermo Finnigan LCQ Duo Ion Trap Mass Spectrometer.

Single crystal X-ray diffraction: All reflection intensities were measured at 110(2) K using a SuperNova diffractometer (equipped with Atlas detector) with Mo Kα radiation (λ

= 0.71073 Å) under the program CrysAlisPro (Version CrysAlisPro 1.171.39.29c, Rigaku OD, 2017). The same program was used to refine the cell dimensions and for data reduction. The structure was solved with the program SHELXS-2014/7 and was refined on F2 with SHELXL-2014/7.[3] A numerical absorption correction based on Gaussian integration over a multifaceted crystal model was applied using CrysAlisPro. The temperature of the data collection was controlled using the system Cryojet (manufactured by Oxford Instruments). The H atoms were placed at calculated positions (unless otherwise specified) using the instructions AFIX 33, AFIX 43 or AFIX 137 with isotropic displacement parameters having values 1.2 or 1.5 Ueq of the attached C atoms. The structure is partly disordered.

Both Mo1-Mo1 and Mo2-Mo2 complexes are found at sites of inversion symmetry, and only the halves are crystallographically independent. The DMF molecules coordinated to the Mo2-Mo2 complex and one of the pyridine rings are disordered over two orientations. The occupancy factors of the major components of the disorder refine to 0.942(3) and 0.52(3), respectively.

^{1}H NMR of JHMF–101 after acid digestion: ^{1}H NMR spectra were obtained on a Bruker Avance 400 MHz spectrometer. Samples were prepared by dissolving approximately 5 mg of vacuum-dried JHMF–101 in 500 μL DMSO-d_6 and 100 μL dilute DCl solution (23 μL 35% DCl in D_2O, diluted in 1.0 mL DMSO).

Powder X-ray diffraction: Powder X-ray diffraction data were collected on a Bruker D8 Focus diffractometer using a Cu X-ray source (Kα = 8.04 keV, 1.5406 Å). The simulated pXRD pattern was calculated using the Mercury 3.10 powder calculation function. The simulated wavelength was set to 1.54056 Å and the peak shape was calculated for a FWHM (2θ) equal to 0.1.

Raman Spectroscopy: Raman spectroscopy was performed on a Horiba-Jobin-Yvon T64000 Raman Spectrometer using a 514 nm laser at 1 mW. The spectrum was collected on JHMF–101 with a 1800 grooves/mm grating during a 30-s exposure.

Infrared Spectroscopy: Infrared spectroscopy was performed on JHMF–101 with a ThermoNicolet Nexus 670 FTIR Spectrometer using OMNIC 6.0a operating software.

BET Analysis: Gas adsorption analysis was conducted on an ASAP 2020 V4.04 using N_2 as the adsorbate gas at 77.417 K. Measurements were made on 0.0797 g of JHMF–101 that was degassed overnight at 90 °C until vacuum stabilized at 10 μmHg. Partial pressures during the measurement ranged between 0.0067 p/p_0 to 0.5500 p/p_0 in a flask with 85.9091 cm^3 cold free space.

Thermogravimetric Analysis: Thermogravimetric analysis was performed on a SDT Q600 (V20.9 Build 20) instrument using alumina pans. Measurements were made from room temperature to 700 °C at a ramp rate of 5 °C/min under a nitrogen flush of 100 mL/min. A sample of JHMF–101 (3.6432 mg) was prepared by drying under vacuum, at room temperature, for 48 hours prior to TGA measurement.

Electron Paramagnetic Resonance: Electron paramagnetic resonance spectroscopy was performed using a Bruker EPR spectrometer with an ER 073 10" magnet and a Bruker ER041 XG microwave bridge. Measurements were made on a powder sample of JHMF–101 in a 4.0 mm quartz tube at 20 K using X-band microwave frequency (9.442639 GHz).

Simulation of the field-sweep continuous wave EPR spectrum was performed in EasySpin 5.2.20 in the slow-motional regime with axial symmetry from the following parameters under Sys: S = ½; Nucs = '(95,96,97)Mo'; Abund = [0.16 0.74 0.1]; g = [1.9345 1.8950]; A = [110 20], lw = 3, and tcorr = 1e-8. The system exhibits better fits under axial symmetry rather than under isotropic or rhombic symmetry.

Absorption Spectroscopy: Solid-state UV-vis absorption spectroscopy was performed on powder of JHMF–101 on glass using a Cary 5000 UV-Vis-NIR Spectrophotometer from Agilent Technologies with an integrating sphere. Absorption spectroscopy on solutions was performed on a Cary 60 UV-Vis Spectrophotometer from Agilent Technologies. A solution of $Mo_2(INA)_4$ in DMF was prepared by letting 5 mg of JHMF–101 powder sit in 5 mL dry DMF at room temperature and then removing the supernatant for measurement.

Elemental Analysis: Elemental analysis was performed at Robertson Microlit Laboratories.

Density Functional Theory Calculations: Computational resources were provided by the Maryland Advanced Research Computing Center (MARCC). Time-dependent DFT (TD-DFT) and molecular orbital calculations were completed using Gaussian09. The B3LYP functional was used along with a split basis set (6-31g* for H, C, N, O atoms and SDD for Mo atoms). Since the XYZ coordinates of 1 were obtained directly from the cif of the compound, single point energies were calculated. Avogadro 1.2.0 was used to isolate XYZ coordinates of the monomer. The same method produced XYZ coordinates the dimer. TD-DFT electronic absorptions were analyzed and visualized using GaussView 5.0.9. Molecular orbitals were rendered in Chemcraft 1.8.

SUPPLEMENTARY FIGURES

Table A1 | Crystallographic data MF–101:

Crystal data	
Chemical formula	$C_{27}H_{23}Mo_2N_5O_9$
M_r	753.38
Crystal system, space group	Triclinic, *P*-1
Temperature (K)	110
a, *b*, *c* (Å)	8.5571 (3), 11.9579 (5), 15.1881 (5)
α, β, γ (°)	111.799 (3), 92.248 (3), 99.262 (3)
V (Å^3)	1415.84 (10)
Z	2
Radiation type	Mo *K*α
μ (mm^{-1})	0.95
Crystal size (mm)	0.12 × 0.05 × 0.03
Data collection	
Diffractometer	SuperNova, Dual, Cu at zero, Atlas
Absorption correction	Gaussian *CrysAlis PRO* 1.171.39.29c (Rigaku Oxford Diffraction, 2017) Numerical absorption correction based on gaussian integration over a multifaceted crystal model Empirical absorption correction using spherical harmonics, implemented in SCALE3 ABSPACK scaling algorithm.
T_{min}, T_{max}	0.890, 1.000
No. of measured, independent and observed [$I > 2\sigma(I)$] reflections	21519, 6499, 5123
R_{int}	0.042
$(\sin \theta/\lambda)_{max}$ (Å^{-1})	0.650
Refinement	
$R[F^2 > 2\sigma(F^2)]$, $wR(F^2)$, *S*	0.033, 0.062, 1.06
No. of reflections	6499
No. of parameters	461

No. of restraints	350
H-atom treatment	H-atom parameters constrained
$\Delta\rho_{max}$, $\Delta\rho_{min}$ (e Å^{-3})	0.53, -0.47

Figure A1

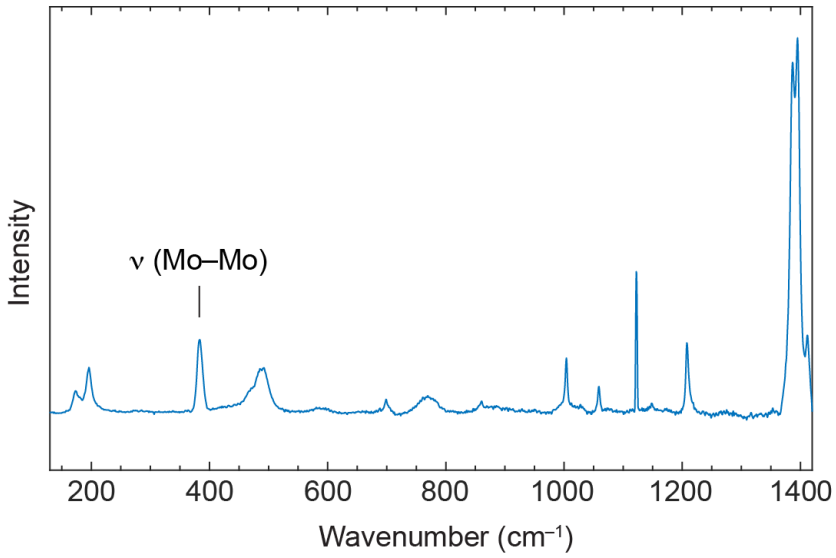

Figure A1 | Raman spectrum of MF–101. The band at 383 cm^{-1} is assigned to the dimolybdenum symmetric mode and is within the range of values reported in the literature.[4]

Figure A2

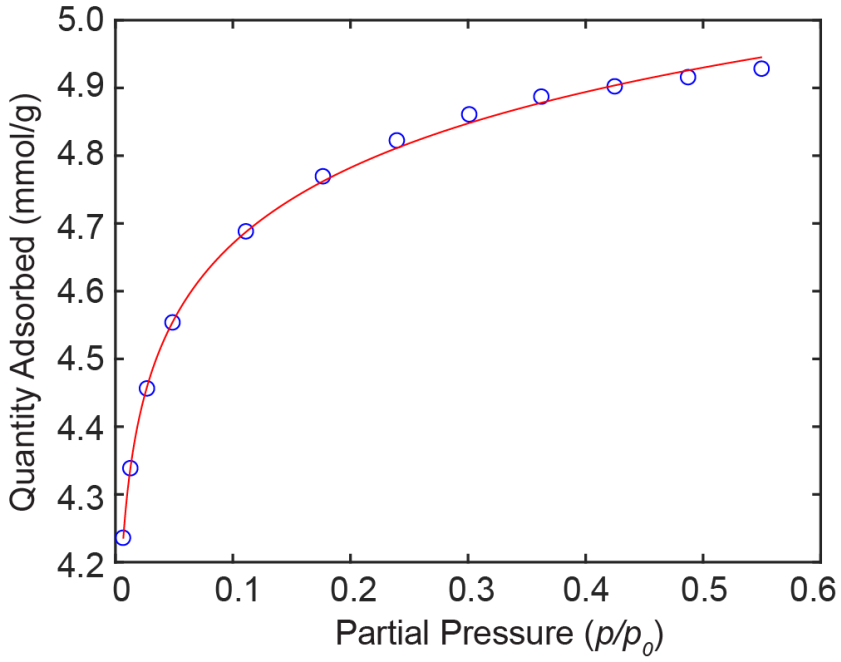

Figure A2 | N_2 adsorption isotherm of MF–101. The N_2 adsorption isotherm for JHMF–101 collected at 77 K. The fit (red line) to the data was used to calculate an apparent BET surface area of 325.8 m^2/g.

Figure A3

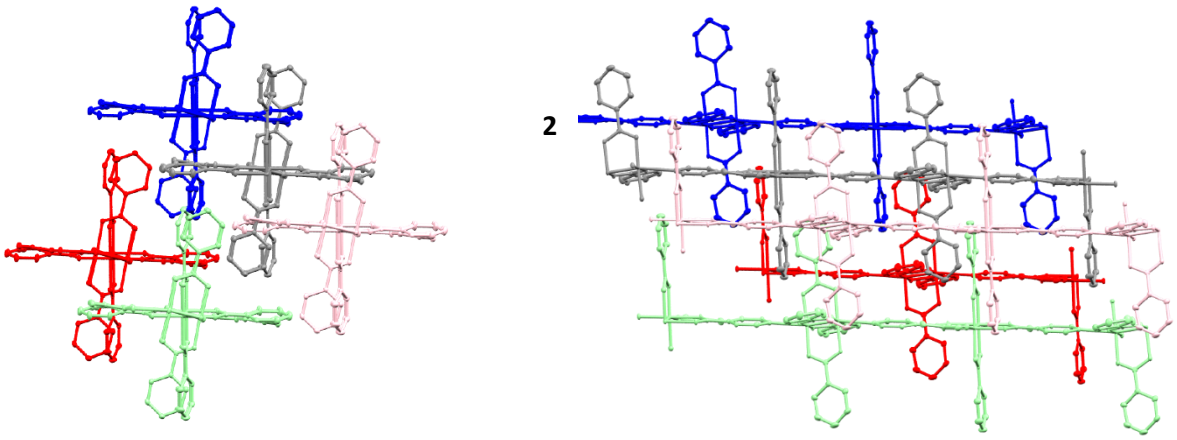

Figure A3 | Crystal packing of MF–101. Packing of the one-dimensional coordination polymers down the axis of coordination (View 1), and along the sides of the 1D molecular chains (View 2).

Figure A4

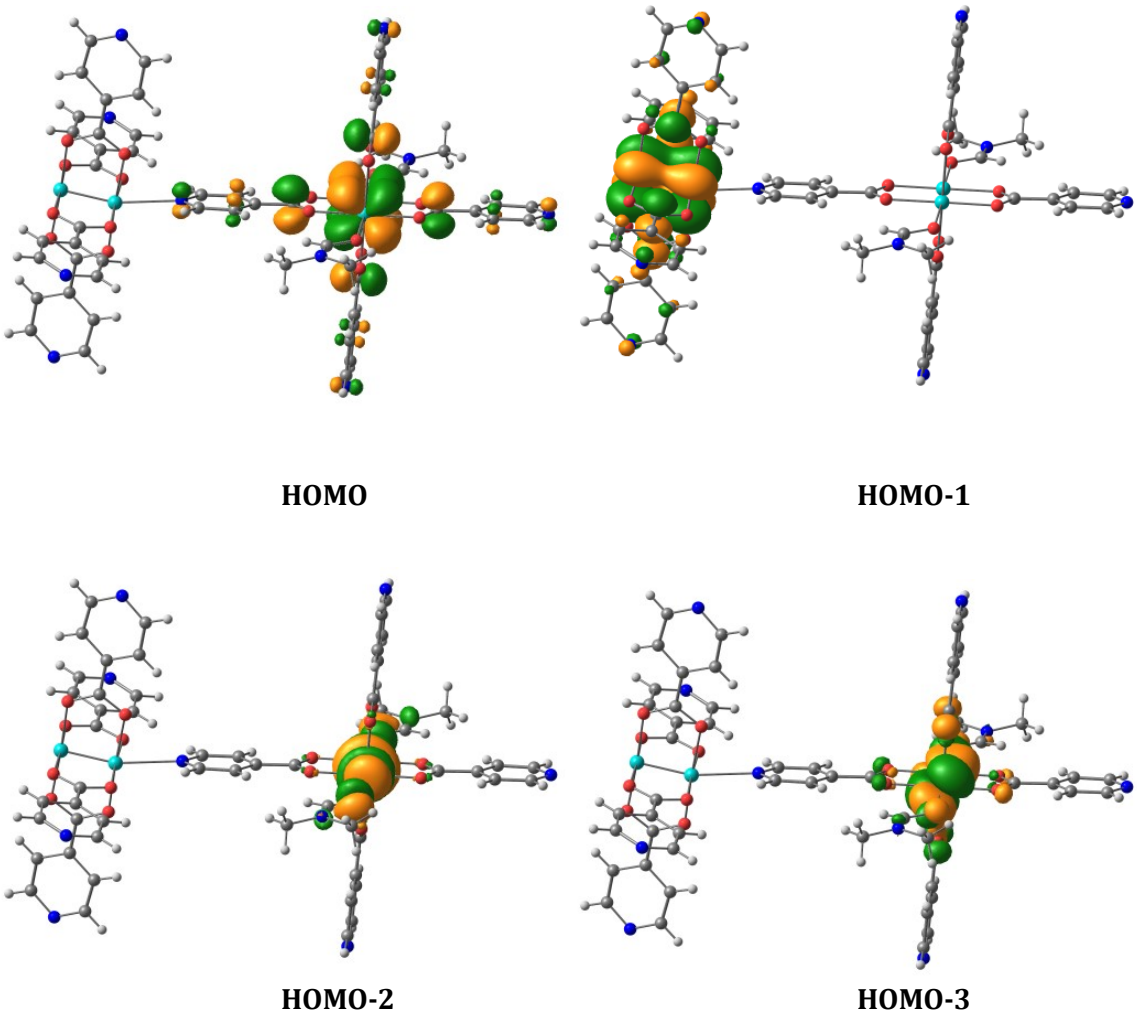

Figure A4 | Electron densities from highest occupied molecular orbitals of the $Mo_2(INA)_4$ dimer. Four highest occupied molecular orbitals from single-point energy calculation on the dimer, showing localized and metal-centered electron densities.

Figure A5

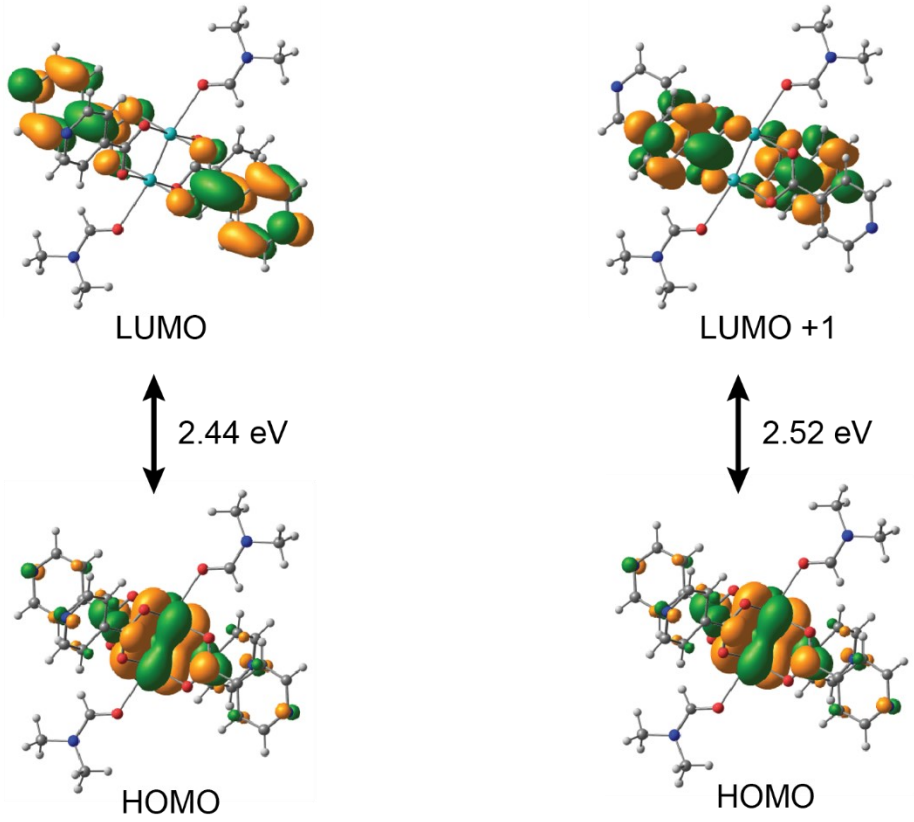

Figure A5 | Calculated electronic transitions of the $Mo_2(INA)_4$ monomer. There are two main electronic transitions calculated for a single paddlewheel unit coordinated to DMF. Both occur primarily between δ(Mo_2) orbital (HOMO) and ligand π* orbitals (LUMO and LUMO +1; 2.44 eV, 507 nm; 2.52 eV, 491 nm).

Figure A6

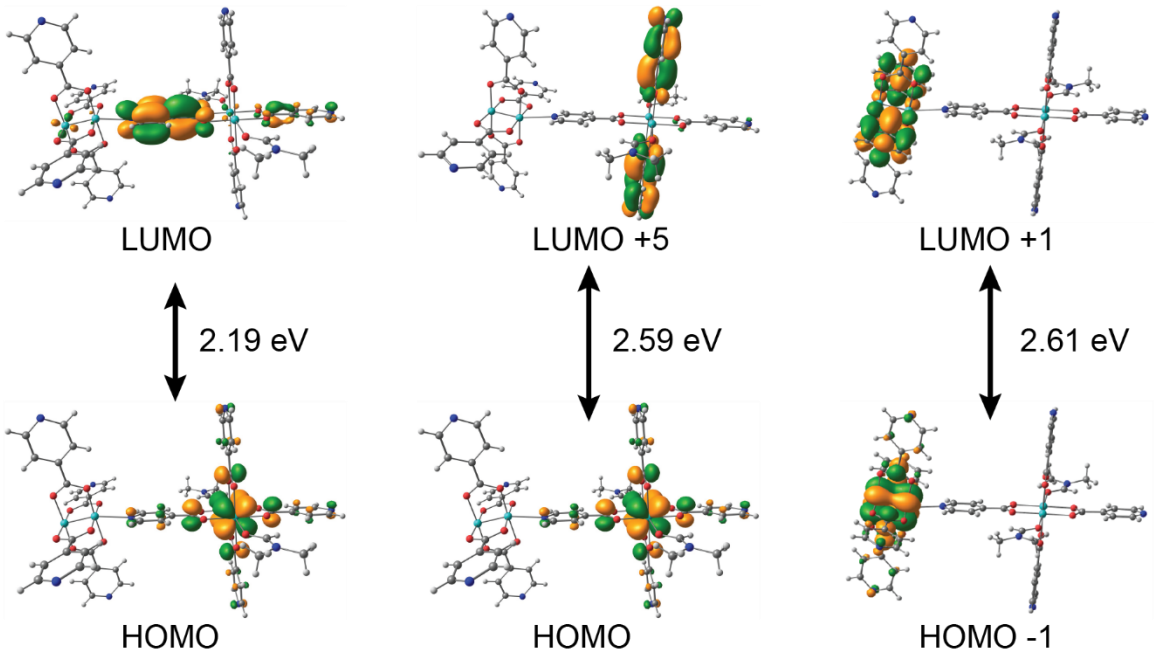

Figure A6 | Calculated electronic transitions of the $Mo_2(INA)_4$ dimer. Three electronic transitions were calculated to be major contributors in the absorbance spectrum based on the calculations of a representative dimer. The HOMO-LUMO transition (2.19 eV, 566 nm) occurs primarily from the $\delta(Mo_2)$ orbital of the DMF-coordinated paddlewheel to the π^* of the INA ligand connecting the two paddlewheels, along the direction of one-dimensional chain. Another major transition (2.59 eV, 479 nm) comes primarily from the HOMO $\delta(Mo_2)$ to the π^* (LUMO +5) of the ligands perpendicular to the connecting ligand. A similar transition (2.61 eV, 475 nm) occurs at the $\delta(Mo_2)$ orbital of the paddlewheel not coordinating to DMF (HOMO -1) to the attached ligand π^* (LUMO +1). The two higher energy transitions are perpendicular to the direction of the one-dimensional chain.

Figure A7

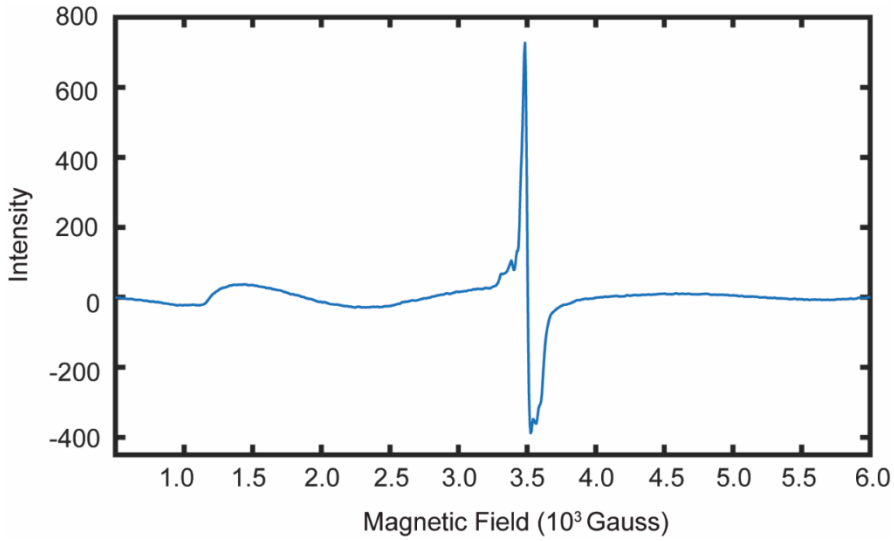

Figure A7 | Electron paramagnetic resonance spectrum of MF–101. The system was modeled as an axial paramagnet.[5] Hyperfine splitting due to molybdenum isotopes (^{95}Mo, I = 5/2; ^{97}Mo, I = 5/2) was observed with a coupling constant of 3.9 mT. A broad feature was also observed around 1500 G ($g \sim 4.5$) and may be attributed to impurities or forbidden half-field transitions.[6]

REFERENCES

1. T. A. Stephenson, E. Bannister and G. Wilkinson, *J. Chem. Soc.*, 1964, **0**, 2538.
2. L. E. Pence, A. M. Weisgerber and F. A. Maounis, *J. Chem. Educ.*, 1999, **76**, 404.
3. Sheldrick, G. M. SHELXTL Version 2014/7. http://shelx.uni-ac.gwdg.de/SHELX/index.php
4. F. A. Cotton and J. G. Norman, *J. Am. Chem. Soc.*, 1972, **94**, 5697–5702.
5. F.E. Mabbs, and D. Collison, *Electron Paramagnetic Resonance of d Transition Metal Compounds,* Elsiever Science Publishers, Amsterdam, The Netherlands, 1992
6. F. A. Cotton, N. S. Dalal, C. Y. Liu, C. A. Murillo, J. M. North and X. Wang, *J. Am. Chem. Soc.*, 2003, **125**, 12945–12952.

APPENDIX B

SUPPLEMENTARY INFORMATION FOR CHAPTER THREE

MATERIALS and METHODS

General: All glassware was cleaned and oven-dried prior to usage. All solvents were thoroughly degassed under inert atmosphere (N_2). Schlenk line techniques were used in the syntheses of molybdenum (II) acetate and molybdenum (II) isonicotinate.

Synthesis of Molybdenum (II) Acetate ($Mo_2(O_2CCH_3)_4$)[1,2]: A 500-mL round-bottom flask was charged with molybdenum hexacarbonyl (3.0 g, 11 mmol). To this flask, acetic acid (100 mL), acetic anhydride (20 mL), and hexane (5 mL) were added. The solution was refluxed at 130 °C for 20 hours with stirring. The solution turned brown, and a bright yellow crystalline solid precipitated. The yellow solid was filtered under N_2 and washed with ethanol. The product was dried under vacuum and stored under N_2 at −20 °C. Yield: 37.1%

Synthesis of Molybdenum (II) Isonicotinate ($Mo_2(INA)_4$•DMF): A solution of $Mo_2(O_2CCH_3)_4$ (0.250 g, 0.584 mmol) and isonicotinic acid (0.712 g, 5.79 mmol) in 50 mL anhydrous dimethylformamide (DMF) was prepared in a 100-mL Schlenk flask under an N_2 atmosphere. To this solution, acetic acid (0.033 mL, 0.574 mmol) was added. The red solution was refluxed at 120 °C for two days while stirring at 300 rpm. When this reaction is performed with stirring speed of 60 rpm, single crystals large enough for x-ray diffraction studies are deposited on the sidewalls of the flask, at the surface of the solution. The bright red product was filtered under N_2, washed with DMF, and dried under vacuum. The product was stored under N_2. Yield: 62%. Elemental analysis measures 42.28% C, 3.00% H, 9.12% N, and 25.74% Mo (theoretical values: 43.04% C, 3.08% H, 9.30% N, and 25.47% Mo).

Assembly of 2D MOFs, MF–102 and MF–103

MF–102: A solution containing $Mo_2(INA)_4$ (0.02 g, 0.03 mmol) in 10 mL dry DMA was allowed to sit at room temperature undisturbed for 2 days. The red solution gradually turned yellow as a dark red precipitate formed at the bottom of the vial. The dark red precipitate was collected and contained single crystals large enough for single-crystal X-ray diffraction (XRD).

The powder XRD pattern of this bulk product matched the simulated powder XRD pattern extracted from single-crystal XRD data.

MF–103: A solution containing $Mo_2(INA)_4$ (0.02 g, 0.03 mmol) and 2 equivalents of DABCO in 10 mL dry DMA was allowed to sit at room temperature undisturbed for 2 days. The red solution gradually turned yellow as a dark red precipitate formed at the bottom of the vial. The dark red precipitate was collected and contained single crystals large enough for single-crystal X-ray diffraction (XRD). The powder XRD pattern of this bulk product matched the simulated powder XRD pattern extracted from single-crystal XRD data.

Single crystal X-ray crystallography of MF–102: All reflection intensities were measured at 110(2) K using a SuperNova diffractometer (equipped with Atlas detector) with Mo *K*α radiation (λ = 0.71073 Å) under the program CrysAlisPro (Version CrysAlisPro 1.171.39.29c, Rigaku OD, 2017). The same program was used to refine the cell dimensions and perform data reduction. The structure was solved with the program SHELXS-2014/7 (Sheldrick, 2015) and was refined on F^2 with SHELXL-2014/7 (Sheldrick, 2015). A numerical absorption correction based on gaussian integration over a multifaceted crystal model was applied using CrysAlisPro. The temperature of the data collection was controlled using the Cryojet system (Oxford Instruments). The H atoms were placed at calculated positions using the instructions AFIX 33, AFIX 43 or AFIX 137 with isotropic displacement parameters having values 1.2 or 1.5 *U*eq of the attached C atoms. The structure is partly disordered.

The Mo-Mo complex is found to be mostly ordered, except for one $-C_5H_4N$ group that is disordered over two orientations. The occupancy factor of the major component of the disorder refines to 0.60(2).

The crystal lattice contains some amount of lattice DMA solvent molecules, and the ratio (Mo-Mo complex):DMA is 1:2. There are four crystallographically independent lattice DMA solvent molecules in the asymmetric unit, but their occupancy factors are all

constrained to 0.5 as those solvent molecules are located at sites of two-fold axial symmetry. One of the four lattice DMA solvent molecule is heavily disordered over 3 orientations, and no anisotropic refinement was performed for those atoms (*i.e.*, C5S > O2S (first orientation); C5S' > O2S' (second orientation); C5SC > O2SC (third orientation). The sum of the occupancy factor of the three different orientations was constrained to be 0.5 using the SUMP instruction.

Single crystal X-ray crystallography of MF–103: All reflection intensities were measured at 110(2) K using a SuperNova diffractometer (equipped with Atlas detector) with Cu *K*α radiation (λ = 1.54178 Å) under the program CrysAlisPro (Version CrysAlisPro 1.171.39.29c, Rigaku OD, 2017). The same program was used to refine the cell dimensions and for data reduction. The structure was solved with the program SHELXS-2014/7 (Sheldrick, 2015) and was refined on F^2 with SHELXL-2014/7 (Sheldrick, 2015). Analytical numeric absorption correction using a multifaceted crystal model was applied using CrysAlisPro. The temperature of the data collection was controlled using the Cryojet system (Oxford Instruments). The H atoms were placed at calculated positions using the instructions AFIX 43 or AFIX 137 with isotropic displacement parameters having values 1.2 or 1.5 *U*eq of the attached C atoms. The structure is partially disordered.

The asymmetric unit contains three lattice DMA solvent molecules. Two of those molecules are fully occupied (one is disordered over two orientations and one is ordered)*, while the third molecule** is found at sites of inversion symmetry, and thus its occupancy factor must be 0.5.

* The occupancy factor of the major component of the disorder refines to 0.797(7).

** This molecule must be disordered as DMA does not have inversion symmetry.

NMR of MF–102 and MF–103 after acid digestion: ^{1}H NMR spectra of solutions of MF–102 and MF–103 were obtained on a Bruker Avance 400 MHz spectrometer. Samples

were dried under vacuum overnight and approximately 5 mg was dissolved in 500 μL DMSO-d_6 and 100 μL dilute DCl solution (23 μL 35% DCl in D_2O in 1.0 mL DMSO).

BET Analysis: Adsorption data were obtained with a Micromeritics 3Flex gas adsorption analyzer. The 3Flex tube was evacuated after being heating in an oven at 150 °C for 24 hours. Once cooled and evacuated, the sealed tube was weighed and loaded with 70 mg of solid. The sample was evacuated at room temperature for 3 hr, with special attention to keeping the evacuation pressure above 1 mbar. After this evacuation, the sample was cooled to 195 K and further evacuated for three hours under full vacuum. Once fully activated, the tube was removed from the instrument and reweighed to determine an accurate mass of the sample (59.9 mg). CO_2 adsorption was measured from 0.00056 to 0.95 P/P_o in a 195 K bath (dry ice/isopropanol).

Powder X-ray diffraction: Powder x-ray diffraction data were collected on a Bruker D8 Focus diffractometer using a Cu x-ray source (Kα = 8.04 keV, 1.5406 Å). The simulated pXRD patterns shown in Figure S7 (purple trace) were calculated using the Mercury 3.10 powder calculation function. The simulated wavelength was set to 1.54056 Å and the peak shape was calculated for a FWHM (2θ) equal to 0.1.

Cyclic Voltammetry: Materials: Graphite rod (99.9995% metals basis, 6.15 mm (0.232 in. diameter × 6 in. long)), Ferrocene (99%, Alfa Aesar), Tetrabutylammonium Hexafluorophosphate (TBA PF_6) (99%, Sigma Aldrich), and 1-Butyl-3-Methylimidazolium Tetrafluoroborate (BMIM BF_4) (98%, Thermo Fisher Scientific).

All electrochemical measurements were performed at ambient temperature (23 ± 1°C), and the instrument utilized consisted of a WaveDriver 20 Bipotentiostat/Galvanostat System controlled through the AfterMath™ Data organizer software. A custom 2-compartment borosilicate glass cell with a porous glass frit separating the working and auxiliary compartments was used. The working compartment and auxiliary compartment

were separated by a porous Aceglass fine frit. Prior to use, electrochemical cells were soaked in Piranha solution (25% H_2O_2), rinsed with Millipore water, and dried in an oven at 120 °C and used when ready. All measurements were conducted on functionalized glassy carbon using a glassy carbon RDE tip working electrode (5 mm diameter, 0.196 cm^2, Alfa Aesar). Prior to each experiment, glassy carbon (GC) electrodes were successively polished in an aqueous 1, 0.3, 0.05 μm slurry against a Tegramin-20 semi-automatic sample polisher and DAC polishing pad using a DiaoDuo diamond suspension. The resulting substrate had a mirror finish. The electrode was then activated by heating at 500 °C at 10^{-5} Torr for 2 hours to improve electrochemical properties.[1,2]

Unless otherwise stated, current densities were normalized to the geometric surface area of the working electrode. In all cases, the auxiliary electrode was a high surface area graphite rod (99.9995% metals basis). TBA PF_6, BMIM BF_4, and anhydrous acetonitrile were used as the supporting electrolyte unless otherwise noted. All measurements were conducted using a Ag/AgCl non-aqueous pseudoreference consisting of a bleach-oxidized silver wire immersed in 0.1 M TBA PF_6 electrolyte and 20 mM of BMIM BF_4. Both cell compartments were sparged continuously for 30 minutes with Argon and kept saturated. All potentials are referenced to the ferrocene/ferrocenium (Fc/Fc^+) couple, which was measured at the end of every experiment by adding a small amount of ferrocene (12 mg, 3 mmol) to the electrolyte solution.

Cyclic voltammograms (CVs) were corrected in situ for uncompensated Ohmic loss (iR_u loss) using positive feedback (PF) correction at the 80% level relative to the measured solution resistance value prior to the experiment.

SUPPLEMENTARY FIGURES

Table B1 | Crystallographic data for MF–102 and MF–103

	MF–102	**MF–103**
Crystal data:		
Chemical formula	$C_{24}H_{16}Mo_2N_4O_8 \cdot 2(C_4H_9NO)$	$2(C_{24}H_{16}Mo_2N_4O_8) \cdot 5(C_4H_9NO)$
M_r	854.53	1796.18
Crystal system, space group	Monoclinic, $P2/c$	Monoclinic, $P2_1/c$
Temperature (K)	110	110
a, b, c (Å)	16.3099 (5), 15.3787 (4), 14.4277 (4)	16.38752 (19), 15.60553 (19), 14.32079 (16)
β (°)	93.304 (3)	91.800 (1)
V (Å^3)	3612.81 (18)	3660.53 (7)
Z	4	2
Radiation type	Mo $K\alpha$	Cu $K\alpha$
μ (mm^{-1})	0.76	6.19
Crystal size (mm)	0.10 × 0.08 × 0.05	0.05 × 0.04 × 0.03
Data collection:		
Diffractometer	SuperNova, Dual, Cu at zero, Atlas	SuperNova, Dual, Cu at zero, Atlas
Absorption correction	Gaussian *CrysAlis PRO* 1.171.39.29c (Rigaku Oxford Diffraction, 2017) Numerical absorption correction based on gaussian integration over a multifaceted crystal model Empirical absorption correction using spherical harmonics, implemented in SCALE3 ABSPACK scaling algorithm.	Analytical *CrysAlis PRO* 1.171.39.29c (Rigaku Oxford Diffraction, 2017) Analytical numeric absorption correction using a multifaceted crystal model based on expressions derived by R.C. Clark & J.S. Reid. (Clark, R. C. & Reid, J. S. (1995). Acta Cryst. A51, 887-897) Empirical absorption correction using spherical harmonics, implemented in SCALE3 ABSPACK scaling algorithm.
T_{min}, T_{max}	0.920, 1.000	0.793, 0.861
No. of measured, independent and observed [$I > 2\sigma(I)$] reflections	28239, 8310, 6021	24295, 7200, 5379
R_{int}	0.043	0.041
$(\sin\theta/\lambda)_{max}$ (Å^{-1})	0.650	0.617
Refinement:		
$R[F^2 > 2\sigma(F^2)]$, $wR(F^2)$, S	0.040, 0.096, 1.03	0.028, 0.063, 1.01
No. of reflections	8310	7200

No. of parameters	629	560
No. of restraints	545	208
H-atom treatment	H-atom parameters constrained	H-atom parameters constrained
$\Delta\rho_{max}$, $\Delta\rho_{min}$ (e Å^{-3})	0.77, -0.40	0.59, -0.53

Figure B1

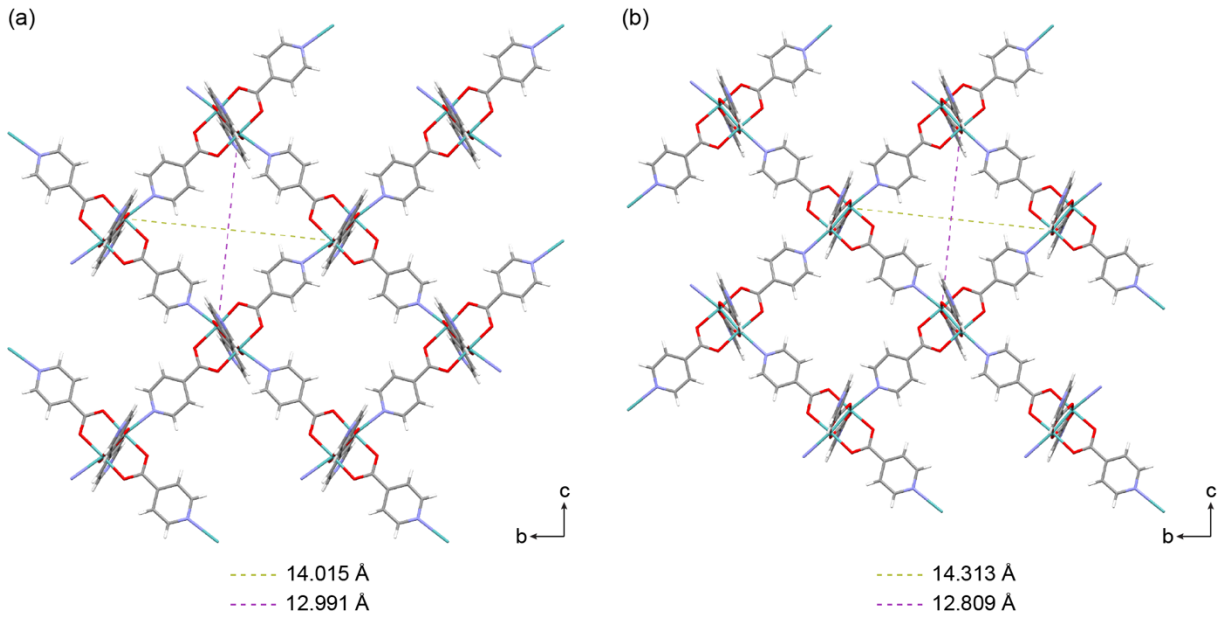

Figure B1 | (100) crystal planes of MF–102 and MF–103. (a) Crystal packing found in the (100) plane in the crystal structure of MF–102. (b) Crystal packing found in the (100) plane in the crystal structure of MF–103. For both structures, the body diagonals (green and purple dashed lines) of the square sub-cell are measured between pairs of Mo atoms across from each other in the crystal structure. Lattice DMA solvent molecules and disorder have been omitted for clarity.

Figure B2

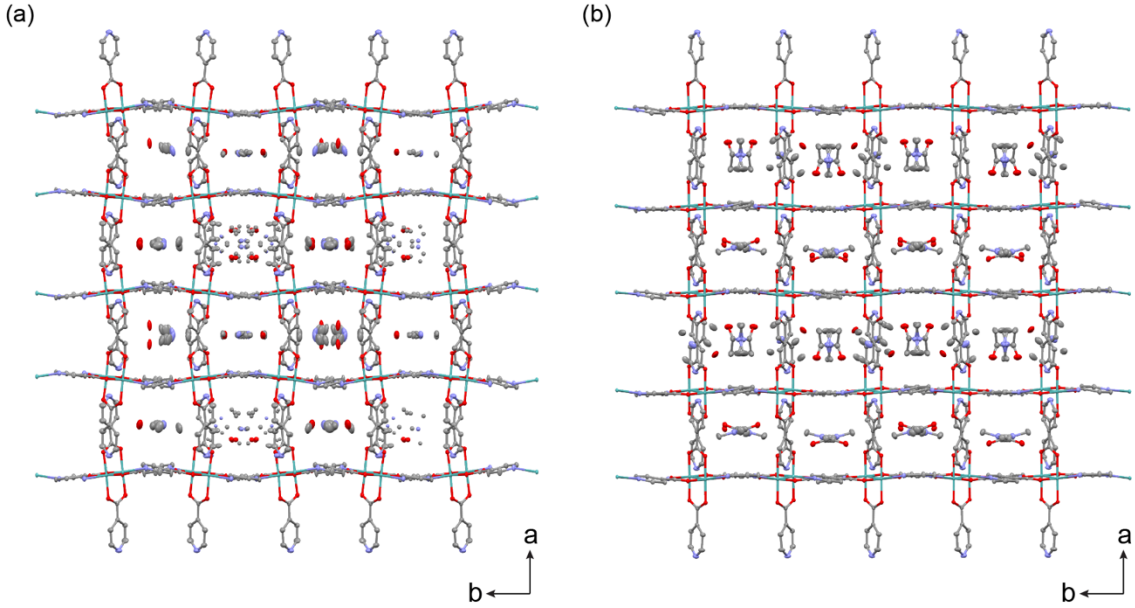

Figure B2 | Crystal structures of MF–102 and MF–103 with solvent. a) Crystal packing structure of MF–102 viewed down the *c* axis. b) Crystal packing structure of MF–103 viewed down the *c* axis. For both structures, displacement ellipsoids are given at 50% probability level. The structure of MF–102 identifies kinking of the 2D lattices and disordered DMA solvent molecules within asymmetric pores. The structure of MF–103 shows a flatter structure for the 2D lattices and increased ordering of the DMA solvent molecules within more symmetric pores. When viewed along the *c* axis, the alternate *d*-spacing within MF–103 is apparent and it is associated with alternate ordering of the DMA solvent molecules.

Figure B3

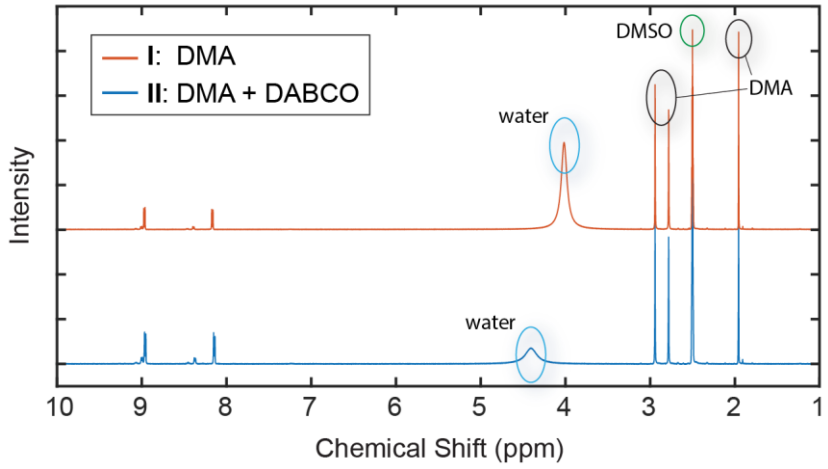

Figure B3 | ^{1}H NMR of MF–102 and MF–103 after acid digestion. Under the digestion conditions used a DABCO ^{1}H would appear at 3.5 ppm. The ^{1}H NMR spectra of MF–102 and MF–103 after acid digestion are similar (save for the position of a water peak) and do not show a peak between 3 and 4 ppm. We conclude that DABCO, though involved in the process of crystallizing MF–103, does not incorporate into the crystal of MF–103.

Figure B4

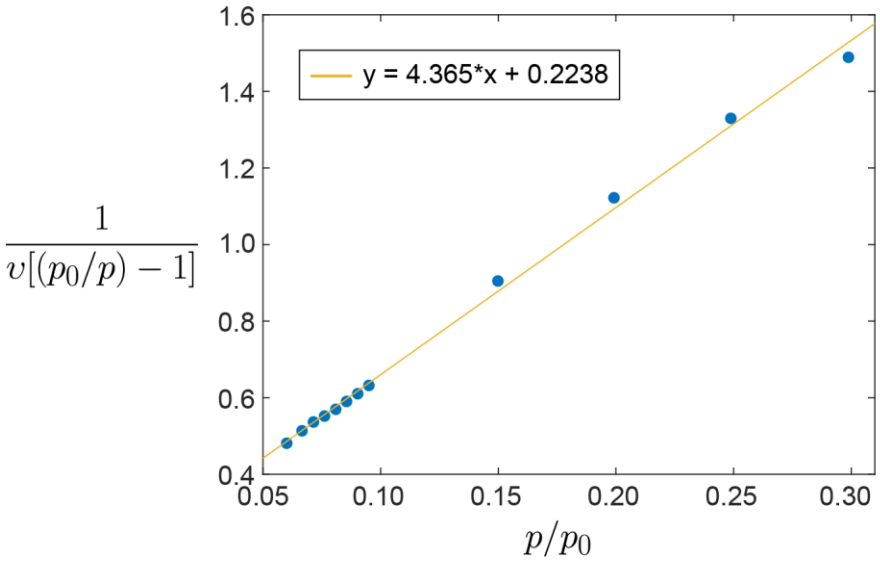

Figure B4 | Calculation of BET surface area. A slope and y-intercepts from a linear fit of the CO_2 adsorption isotherm of MF–102 between 0.05 and 0.30 p/p_0 are used to solve the equation $S_{BET} = \frac{1}{m+b} N_A s$, where m is the slope, b is the y-intercept, N_A is Avogadro's number, and s is the CO_2 adsorption cross-section (0.1420 nm^2). These calculations yield S_{BET} = 18.636 m^2 / g

Figure B5:

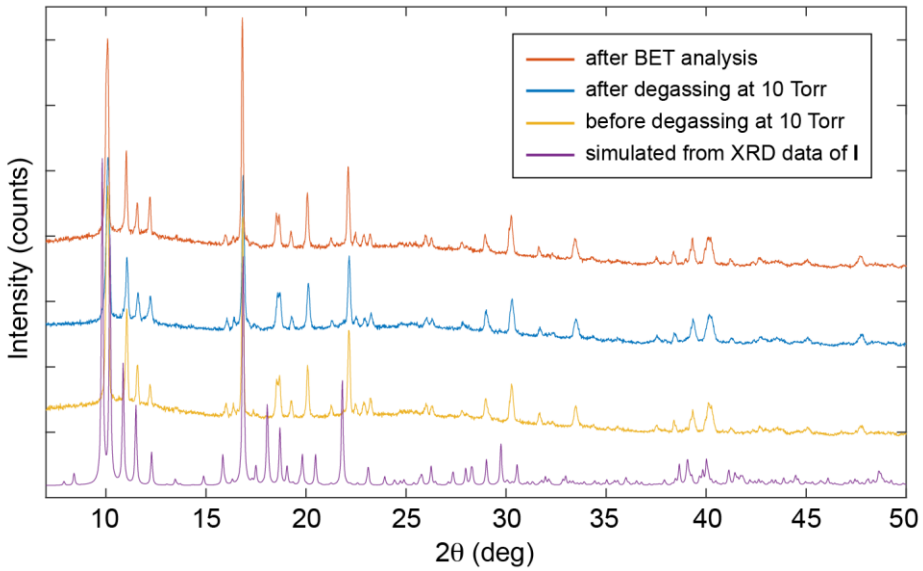

Figure B5 | Powder XRD of MF–102. Powder XRD spectra were collected on the same sample of 2D MF–102 crystals before and after degassing prior to BET analysis, and also after BET analysis. The spectra collected on a sample of MF–102 before degassing at 10 Torr (yellow), after degassing at 10 Torr (blue), and after BET analysis (orange) closely match with each other and also with the simulated pXRD pattern (purple) obtained from the single crystal data (see Methods). Together these data show the crystal structure of MF–102 was maintained throughout the various treatments the sample was subjected to as part of BET analysis.

Figure B6

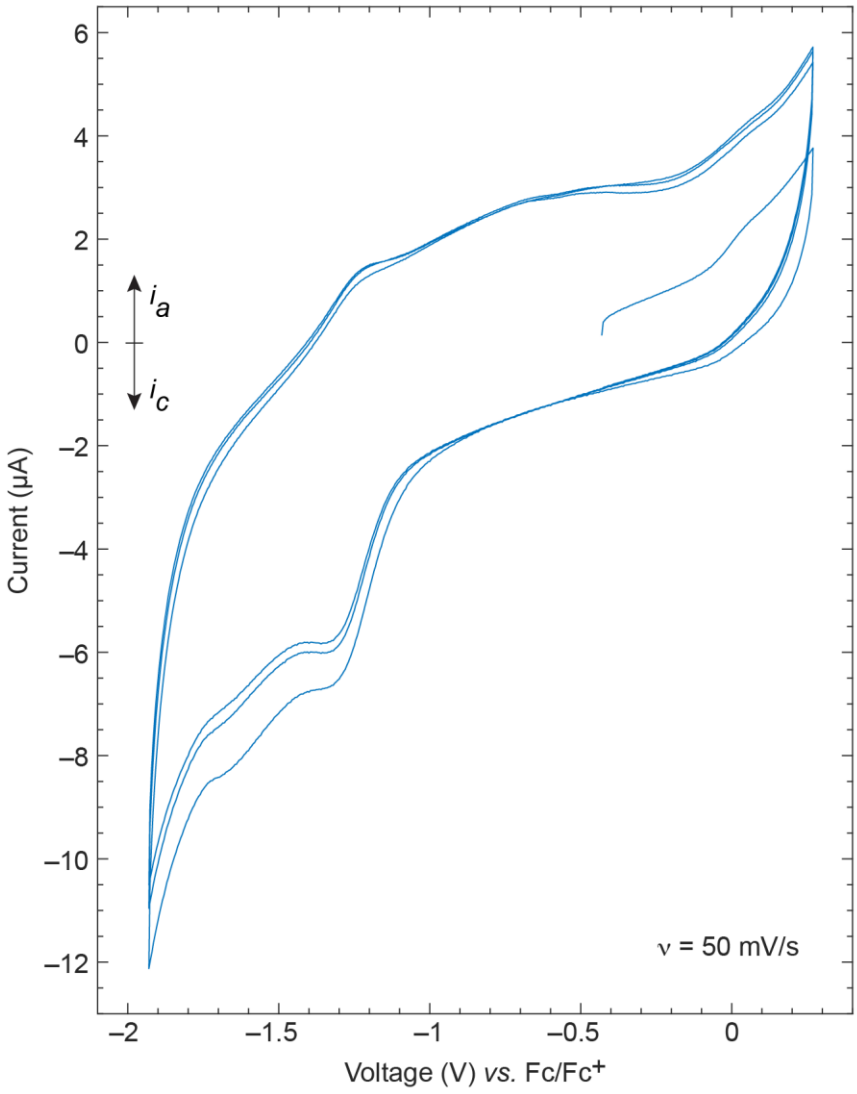

Figure B6 | Cyclic voltammogram of MF–102 at 50 mV/s for 3 cycles. The CV data show that the redox behavior of MF–102 remains stable over the course of multiple CV scans at 50mV/s.

Figure B7

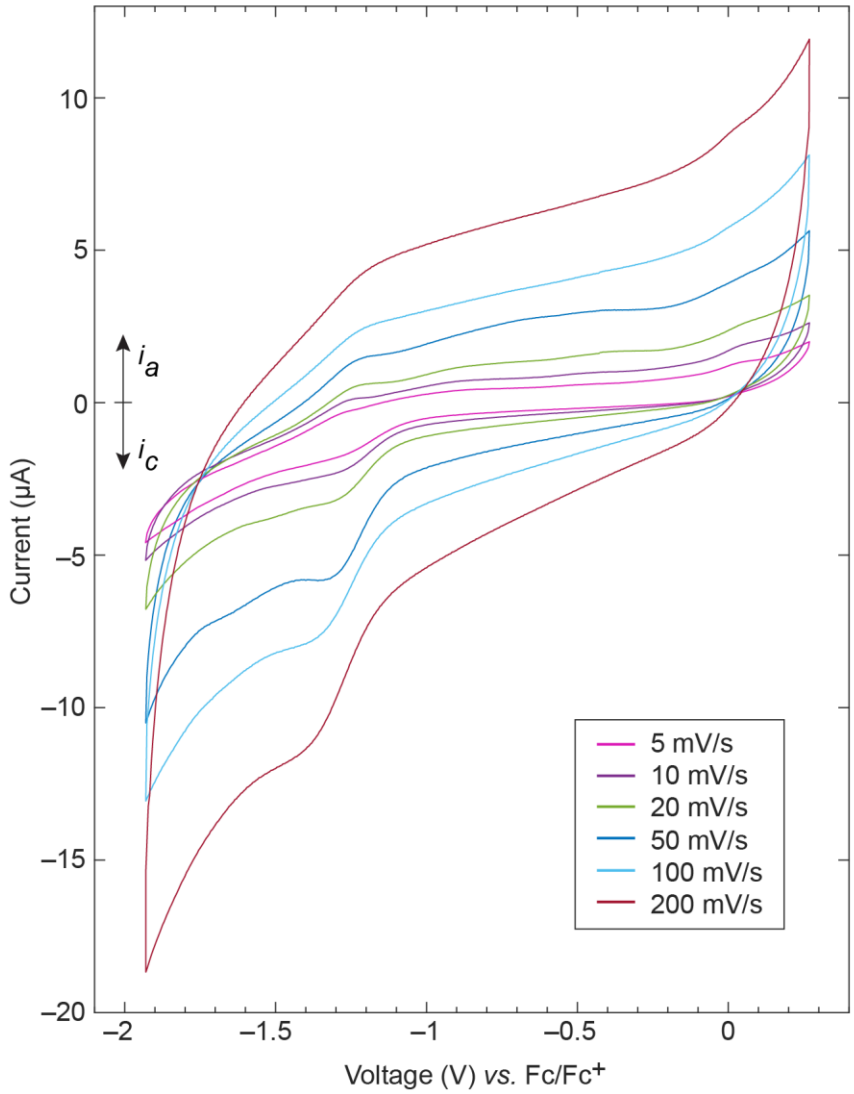

Figure B7 | Cyclic voltammogram of MF–102 at multiple scan rates. CV scans of MF–102 were collected at scan rates ranging from 5 mV/s to 200 mV/s between –2.0 V and +0.5 V. Potentials are referenced with respect to ferrocene/ferrocenium couple (Fc/Fc^+).

Figure B8

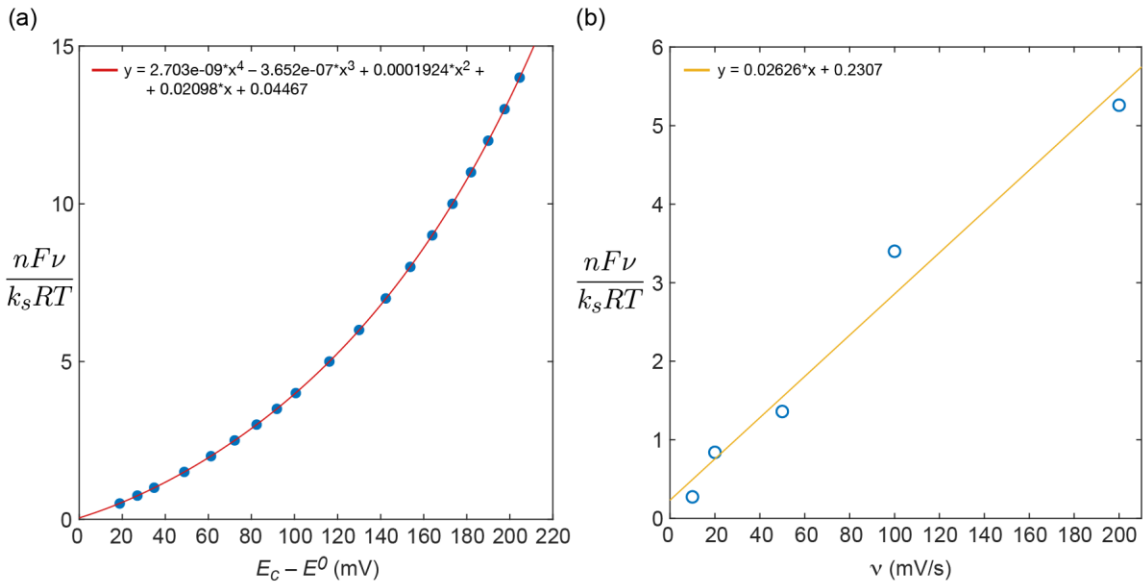

Figure B8 | Calculation of heterogeneous electron transfer rate constant k_s. (a) When peak potential separations can only be extracted from CV scans taken at less than ~ 200 mV/s, we use Laviron's calculations for $nF\nu/k_sRT$ *vs.* ΔE_p with an assumption of a charge transfer coefficient α = 0.5, where n is the number of electrons (1), F is Faraday's constant, ν is the scan rate, k_s is the standard heterogeneous electron transfer rate constant, R is the gas constant, and T is temperature. These data are obtained from Ref. 3 and appear as the blue filled circles. A 4th order polynomial fit to these data allows extraction of the $nF\nu/k_sRT$ values shown as blue open circles in **b**. (b) The slope from a linear fit of $nF\nu/k_sRT$ (obtained from **a**) *vs.* scan rate ν is used to solve $k_s = \frac{nF}{RT}\frac{1}{b}$, where b is the slope of the linear fit, 0.02626. These calculations furnish k_s = 1.49 s^{-1}.

REFERENCES

1) Fagan, D. T.; Hu, I.-F.; Kuwana, T. *Anal. Chem*. **1985**, *57*, 2759–2763.

2) Stutts, K. J.; Kovach, P. M.; Kuhr, W. G.; Wightman, R. M. *Anal. Chem.* **1983**, *55*, 1632–1634.

3) Laviron, E. *J. Electronanal. Chem.* **1979**, *101*, 19–28.

APPENDIX C

SUPPLEMENTARY INFORMATION FOR CHAPTER FOUR

MATERIALS and METHODS

CVD Reactor: Our home-built chemical vapor deposition (CVD) system is a versatile quartz tube hot-wall reactor design with a manifold of mass flow controllers (MKS Instruments: GM50A series MFCs) and a closed-loop pressure control system (MKS Instruments: 640B pressure controller). The manifold and pressure control circuit are both operated through custom LabView scripts running on a PC. The furnace (Thermo Scientific-Lindeberg Blue M – 3 zone) has 3 independently controllable zones, each of which measures 25 cm in length and can reach temperatures of 1200 ˚C. A 400 ˚C temperature differential can be maintained between adjacent zones through the use of thermal inserts. A high-vacuum pump (Leybold: LV80 screw pump) is used to evacuate our CVD system to a base pressure of 0.01 mTorr and is able to safely manage any toxic or pyrophoric effluent. The metal sealed GM50A series mass flow controllers on our CVD reactor permit highly accurate (1% setpoint accuracy) flow control and are accompanied by NIST traceable calibration sheets. Prior to all CVD reactions, we thoroughly washed and then performed bake out of quartz tubes (Quartz Plus: 22 mm inner diameter, 25.4 mm outer diameter) at 600 ˚C for 1 hr under a 10 sccm N2 flow.

CVD Synthesis and Methods: Crystalline powder $Mo_2(INA)_4$ (0.010 g) was added to a ceramic boat and this boat was placed in a quartz tube (see §1 above) along with a glass or SiO_2/Si deposition substrate. Substrates were cleaned by sonication in acetone and IPA and then dried with compressed air. When the quartz tube was placed in the three-zone furnace, the boat containing $Mo_2(INA)_4$ was centered in the middle zone and the deposition substrate was placed 9 cm downstream of the precursor boat and aligned with a thermal insulator between the center and downstream zones. The system was degassed to 1×10^{-5} Torr. The system was held at 20 Torr with a 20 sccm N_2 flow. The middle zone was heated to 325 °C at a rate of 15 °/min and then held at 325 °C for 15 minutes. The set point for the temperature

controller operating the downstream zone, which contains the substrate, was set to room temperature. Based on independent calibration runs and measurements, we estimate the temperature inside the quartz tube to be ~40 ˚C higher than the controller set point value and the region containing the substrate to be approximately 100 ˚C cooler than the middle zone containing the precursor. From these data points we estimate the substrate temperature to be ~265 ˚C. After the initial 15 min of reaction time, the reactor was allowed to cool slowly over 20 min to 200 °C while maintaining 20 Torr. Finally, to rapidly terminate the reaction, the furnace lid was propped open, thereby allowing the quartz tube to cool by 100 ˚C within ~1 min, and the reactor pressure was raised to atmosphere.

For reactions yielding thinner deposits, the only modification to these aforementioned reaction conditions was the placement of the substrate 11 cm downstream of the precursor. The optical images in Figure 4.2 and Figure C1 are of crystals synthesized with the substrate positioned 9 cm from the precursor boat. The SEM and AFM images in Figure 4.2 are of crystals synthesized with the substrate positioned 11 cm from the precursor boat.

AFM Methods: Atomic force microscopy was performed in tapping mode using a Molecular Imaging PicoScan Controller. Aluminum reflex coated Si AFM probes were used. Data were processed and analyzed using Gwyddion 2.49 software.[44]

OM Methods: Optical images were obtained using a Zeiss Axio Scope.A1 microscope interfaced with a Zeiss Axiocam 105 color microscope camera (5 megapixel resolution). CVD grown crystals of $Mo_2(INA)_4$ were imaged directly on growth substrates and analyzed using ZEN software.

Powder X-ray Diffraction: Powder x-ray diffraction data were collected on a Bruker D8 Focus diffractometer using a Cu x-ray source (Kα = 8.04 keV, 1.5406 Å). The step size for a 5–60°, 4 minute scan is 0.018585749° using a LynxEye detector. The exact scan time is 4 minutes and 10 seconds, using 2961 steps at 0.08 seconds/step. Measurements were

performed at room temperature. The simulated pXRD patterns shown in Figure 3 and Figure S5 (blue trace) were calculated using the Mercury 3.10 powder calculation function. The simulated wavelength was set to 1.54056 Å and the peak shape was calculated for a FWHM (2θ) equal to 0.1.

Single Crystal X-ray Diffraction: Individual single crystal samples were isolated from the substrate on which they were grown/formed via an oil-lubricated Kapton loop. All reflection intensities were measured at 175(2) K* using a SuperNova diffractometer (equipped with Atlas detector) with Cu *K*α radiation (λ = 1.54178 Å) under the program CrysAlisPro (Version CrysAlisPro 1.171.39.29c, Rigaku OD, 2017). The same program was used to refine the cell dimensions and for data reduction. The structure was solved with the program SHELXS-2014/7[45] and was refined on F^2 with SHELXL-2014/7[45]. Analytical numeric absorption correction using a multifaceted crystal model was applied using CrysAlisPro. The temperature of the data collection was controlled using the system Cryojet (manufactured by Oxford Instruments). The H atoms were placed at calculated positions using the instructions AFIX 43 with isotropic displacement parameters having values 1.2 *U*eq of the attached C atoms. The structure is partly disordered. The crystallographic structure of MF–104 is provided in Figure C13.

A few attempts to collect data at 110 K were made (the crystals were flashcooled from RT to 110 K), but the data were unsatisfactory as the crystals always diffracted weakly (possibly due to some crystal damage from a solid-solid phase transition). A phase transition occurring at *ca.* 150 K was later confirmed *via* a set of *Cp* vs. *T* measurements. It was then decided to collect another data set at 175 K (the crystal being flashcooled from RT to 175 K). At 175 K, the crystal behaved normally, and the diffraction pattern was clean and consistent with a single crystal.

One of the four coordinated 4-pyridinecarboxylate is found to be disordered over two orientations, and the occupancy factor of the major component refines to 0.51(2). Because a and b are approximately equal in length, a check for twinning (an orthorhombic unit cell emulating a tetragonal unit cell) was done using the twin relationship 0 1 0 / 1 0 0 / 0 0 -1. The BASF scale factor refined to zero, and thus twinning could be ruled out. The crystal lattice contains some solvent accessible voids that contain some unresolved electron density. In the asymmetric unit, three peaks (Q7-Q8-Q9) ranging from 0.72-0.74 e⁻ Å^3 were found in one void. As those residual electron density peaks were small in values, and could not be fully interpreted (maybe some partially occupied lattice water molecule trapped in the crystal), their contribution was then removed from the final refinement using the SQUEEZE[46] procedure.

Single Crystal X-ray Crystallography of MF–104 → MF–102. Individual single crystal samples were isolated from the substrate on which they were grown/formed via an oil-lubricated Kapton loop. All reflection intensities were measured at 110(2) K using a SuperNova diffractometer (equipped with Atlas detector) with Cu Kα radiation (λ = 1.54178 Å) under the program CrysAlisPro (Version CrysAlisPro 1.171.39.29c, Rigaku OD, 2017). The same program was used to refine the cell dimensions and for data reduction. The structure was solved with the program SHELXS-2014/7[45] and was refined on F2 with SHELXL-2014/7[45]. Analytical numeric absorption correction based on a multifaceted crystal model was applied using CrysAlisPro. The temperature of the data collection was controlled using the system Cryojet (manufactured by Oxford Instruments). The H atoms were placed at calculated positions using the instructions AFIX 33, AFIX 43 or AFIX 137 with isotropic displacement parameters having values 1.2 or 1.5 Ueq of the attached C atoms. The structure is partly disordered. The crystallographic structure of 2 is provided in Figure C14.

The Mo-Mo complex is found to be mostly ordered, except for one –C5H4N group that is disordered over two orientations. The occupancy factor of the major component of the disorder refines to 0.64(3).

The crystal lattice contains some amount of lattice DMA solvent molecules, and the ratio (Mo-Mo complex):DMA is 1:2. There are four crystallographically independent lattice DMA solvent molecules in the asymmetric unit, but their occupancy factors are all constrained to 0.5 as those solvent molecules are located at sites of twofold axial symmetry. One of the four lattice DMA solvent molecule is heavily disordered over 3 orientations, and no anisotropic refinement was performed for those atoms (i.e., C5S > O2S (first orientation); C5S' > O2S' (second orientation); C5SC > O2SC (third orientation). The sum of the occupancy factor of the three different orientations was constrained to be 0.5 using the SUMP instruction.

Single Crystal X-ray Crystallography of MF–104 → 2D MOF Variant: Individual single crystal samples were isolated from the substrate on which they were grown/formed via an oil-lubricated Kapton loop. All reflection intensities were measured at 110(2) K using a SuperNova diffractometer (equipped with Atlas detector) with Cu Kα radiation (λ = 1.54178 Å) under the program CrysAlisPro (Version CrysAlisPro 1.171.39.29c, Rigaku OD, 2017). The same program was used to refine the cell dimensions and for data reduction. The structure was solved with the program SHELXS-2014/7[45] and was refined on F2 with SHELXL-2014/7[45]. Analytical numeric absorption correction based on a multifaceted crystal model was applied using CrysAlisPro. The temperature of the data collection was controlled using the system Cryojet (manufactured by Oxford Instruments). The H atoms were placed at calculated positions using the instructions AFIX 43 with isotropic displacement parameters having values 1.2 Ueq of the attached C atoms. The structure is partly disordered. The crystallographic structure of the 2D MOF variant is provided in Figure C15.

The Mo-Mo complex is found at a site of twofold axial symmetry in the asymmetric unit, and only one half of the molecule is crystallographically independent. The crystal lattice includes some fair amount of lattice DMA solvent molecules that are found to be very disordered. In the final refinement, their contributions have been removed using the SQUEEZE procedure in Platon[46].

Scanning electron microscopy: High resolution scanning electron micrographs were obtained on a Tescan Mira3 GMU SEM equipped with a field emission gun. Images of device of MF–104 and MF–102 were collected using the Mira3's in-lens secondary electron detector for beam energies between 10 – 20 kV, a working distance of 10 mm, and accumulation times of 10 minutes.

Raman spectroscopy: Raman spectroscopy was performed on a Horiba-Jobin-Yvon T64000 Raman Spectrometer using a 514 nm laser operating at a power of 1 mW.

Phase conversions: Conversion of MF–104 to MF–102 was initially observed by exposing CVD crystals to anhydrous DMA vapors. Crystals of MF–104 grown on glass substrates were placed within 20 mL glass scintillation vials, which were inserted, uncapped, within 100 mL VWR glass media bottles filled with 2 mL anhydrous DMA. The media bottles were capped and left undisturbed in RT conditions. Conversion to MF–102 could be observed in 48 hours as an orange-red color change.

Cyclic conversions between MF–104 and MF–102 were more easily completed using bulk polycrystalline samples of each form. Solution grown crystals of MF–102 were obtained from recrystallization of 10 mg $Mo_2(INA)_4$ in 5 mL anhydrous DMA. Crystals grown after 48 hours were collected and dried under vacuum. 5 mg crystals were placed in 20 mL glass scintillation vials, which were placed, uncapped, within 100 mL VWR glass media bottles filled with 2 mL anhydrous methanol for 48 hours. Upon complete conversion to MF–104, the remaining

crystalline sample was placed in a second media bottle with 2 mL anhydrous DMA for 48 hours. pXRD was used to monitor conversion between MF–104 and MF–102.

Heat capacity measurement: Heat capacity data were collected on a Quantum Design Physical Property Measurement System from 2K to 300K, with a total of 80 temperature set points. Sample pellets were prepared by mechanically pressing powders of MF–104 converted from MF–102 then dried.

Device fabrication: A single crystal of MF–104 was transferred from a growth substrate to a $Si_3N_4/SiO_2/Si$ substrate by mechanical exfoliation using Kapton tape. Electrical contacts (Ti (adhesion layer): 7 nm; Au (contact layer): 300 nm) were patterned over the MOF crystals by electron-beam lithography and then deposited through thermal evaporation. First, PMMA/MMA (C2/EL 11) layers were deposited over the device substrates containing the 1D and 2D crystals by spin-coating at 4000 rpm for 40 s. The resists were subjected to baking at 180 ˚C for 2 min after each coating step. The contact patterns were defined by electron-beam lithography (JEOL JSF-7001F) followed by resist development and rinsing in MIBK and IPA for 90 s and 30 s, respectively. A 7 nm thick Ti adhesion layer followed by a 300 nm thick Au layer was deposited by thermal evaporation. Residual metal lift-off was performed in acetone over 3 hr.

Charge transport measurements: The fabricated devices were mounted to a *xyz*-translation stage, which is part of our home-built device characterization workstation. The devices were connected via Au-plated W probes (74JA-BT-PS108, American Probe & Technologies Inc.) and triax cables to an ultra-low noise (< 100 fA) semiconductor parameter analyzer (Keithley 4200-SCS). The device current was recorded while the applied voltage was swept from –20 V to 20 V. For the photocurrent measurement, the output of a continuous wave laser diode was focused on the device during the *I-V* measurement. The wavelength and spot size of the pump beam were 520 nm and ~1 μm, respectively. For characterization of

the temporal photoresponse of the devices, periodic laser illumination was generated by using a home-built optical chopper with an interval and duration of 5 s.

Scanning tunneling microscopy: All STM experiments were performed by the Crommie group at UC Berkeley in a home built ultra-high vacuum (UHV) STM system with Pt/Ir tips at T ~7 K. Standard Ar^+ sputtering/annealing cycles were applied in order to prepare atomically-clean Au(111) growth substrates. $Mo_2(INA)_4$ precursors were deposited onto the Au(111) surface, which was held at room temperature under UHV conditions (base pressure ≈ 2×10^{-10} Torr), using a home-built Knudsen-type evaporator. The coverage was controlled by separately adjusting the evaporator temperature (typically 280 °C) and deposition time (typically 15 minutes). After deposition the sample was annealed up to 250 °C to form the single-layer 2D MOF. After growth the samples were directly transferred into the STM chamber and were cooled to ~7 K for STM imaging. All STM images were processed using WSxM freeware[47].

SUPPLEMENTARY FIGURES

Figure C1

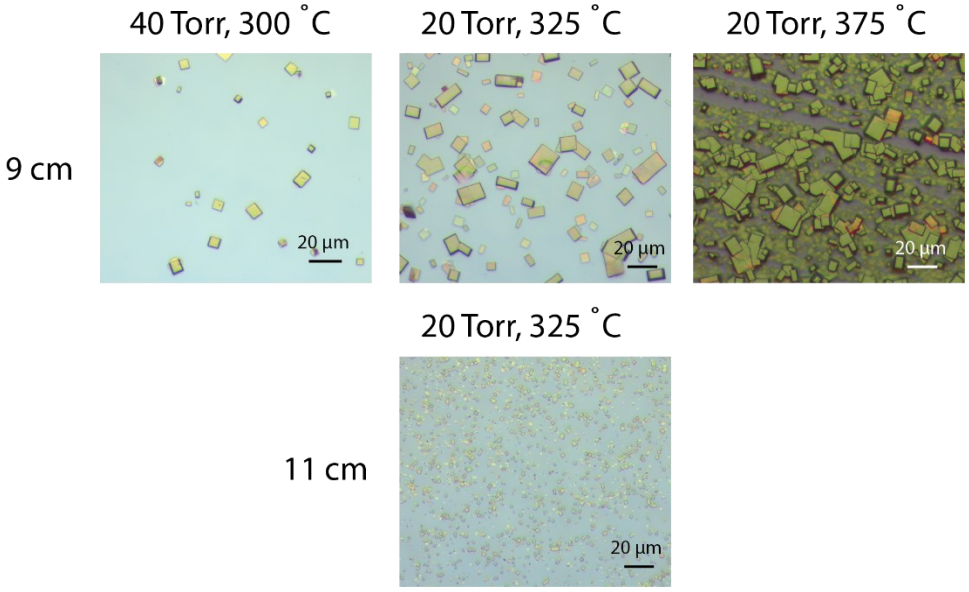

Figure C1 | CVD growth of 1 at various conditions. Optical images of representative crystal growth under various growth conditions. Crystals grown at 20 Torr and 325 °C have edge lengths up to ~50 µm and have a mean area of 96 ± 55 µm^2 (center). Crystals grown at lower temperatures are typically smaller in size and exhibit lower nucleation density (left) while crystals grown at higher temperatures exhibit greater surface coverage of the deposition substrate and begin to form films (right). Crystals grown with the substrate 11 cm downstream of the precursor boat are smaller and thinner (bottom).

Figure C2

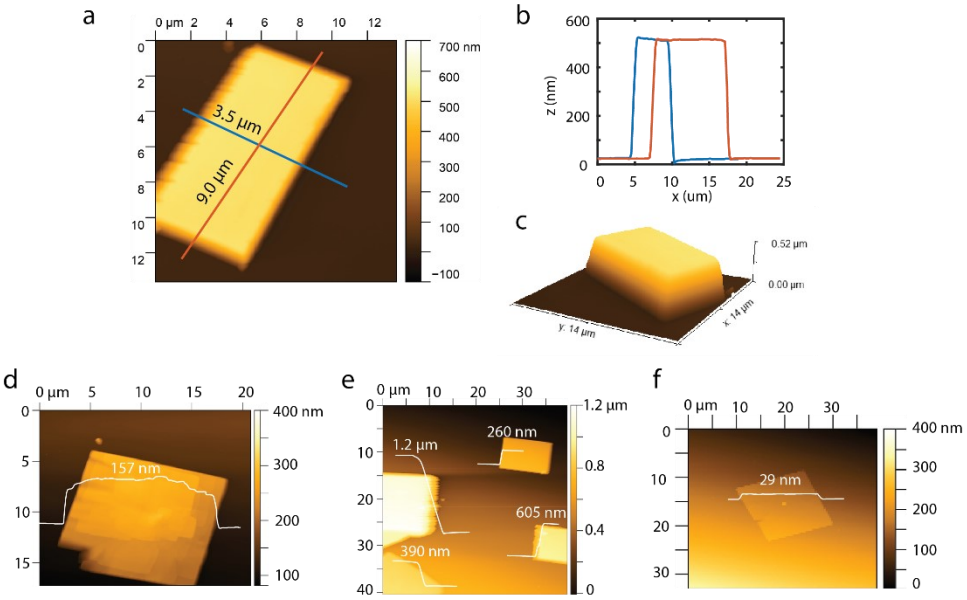

Figure C2 | Atomic force microscopy of MF–104. (a) Atomic force micrograph of a 9.0 µm × 3.5 µm rectangular crystal of MF–104. (b) Line profiles taken along the annotated portions of the AFM in 'a'. The crystal is uniform and 500 nm thick. (c) 3D AFM map of the crystal displayed in 'a'. (d.e) Atomic force micrographs of crystals synthesized under standard reaction conditions with the substrate 9 cm downstream of the precursor. These crystals have thicknesses in the range of 100 – 1200 µm. (f) Atomic force micrograph of a single crystalline deposit synthesized under standard reaction conditions with the substrate 11 cm downstream of the precursor. The crystal is 29 µm thick.

Figure C3

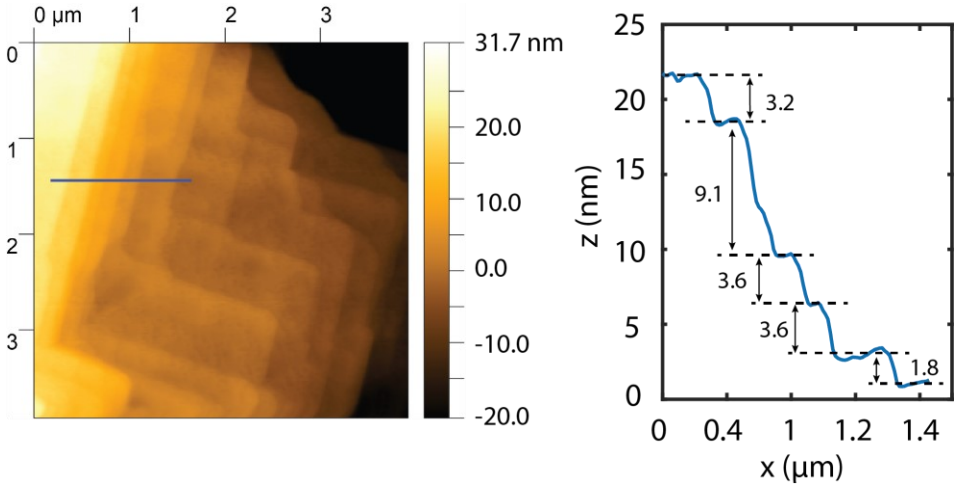

Figure C3 | Atomic force microscopy of MF–104. Atomic force micrograph of the edge of a crystal of MF–104. Step edges are clearly visible and are associated with layers measuring between 1.8 nm and 9.1 nm. These layers are likely comprised of between 2 and 10 stacked sheets of horizontally assembled 1D zig-zag chains as shown in Figure 4.2.

Figure C4

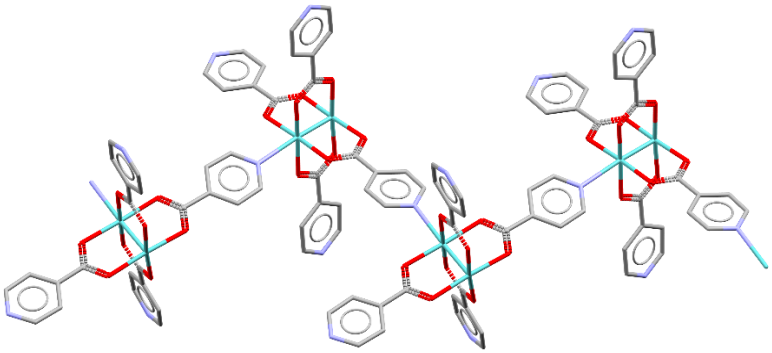

Figure C4 | Crystal structure 1D zig-zag chain. Crystal packing structure of an under-coordinated 1D chain of MF–104. H atoms and disorder have been omitted for clarity.

Table C1 | Crystallographic information of MF–104 and MF–102

	MF–104	MF–102
Crystal data		
Chemical formula	$C_{24}H_{16}Mo_2N_4O_8$	$C_{24}H_{16}Mo_2N_4O_8 \cdot 2(C_4H_9NO)$
M_r	680.29	854.53
Crystal system, space group	Orthorhombic, *Pbca*	Monoclinic, $P2/c$
Temperature (K)	175	110
a, b, c (Å)	14.8962 (3), 14.8796 (3), 26.2130 (4)	16.3096 (7), 15.3613 (4), 14.4440 (4)
β (°)	90°	93.000 (3)
V (Å^3)	5810.10 (19)	3613.8 (2)
Z	8	4
Radiation type	Cu $K\alpha$	Cu $K\alpha$
μ (mm^{-1})	7.50	6.22
Crystal size (mm)	0.07 × 0.07 × 0.02	0.05 × 0.04 × 0.01
Data collection		
Diffractometer	SuperNova, Dual, Cu at zero, Atlas	SuperNova, Dual, Cu at zero, Atlas
Absorption correction	Analytical *CrysAlis PRO* 1.171.39.29c (Rigaku Oxford Diffraction, 2017) Analytical numeric absorption correction using a multifaceted crystal model based on expressions derived by R.C. Clark & J.S. Reid. (Clark, R. C. & Reid, J. S. (1995). Acta Cryst. A51, 887-897) Empirical absorption correction using spherical harmonics, implemented in SCALE3 ABSPACK scaling algorithm.	Gaussian *CrysAlis PRO* 1.171.39.29c (Rigaku Oxford Diffraction, 2017) Numerical absorption correction based on gaussian integration over a multifaceted crystal model Empirical absorption correction using spherical harmonics, implemented in SCALE3 ABSPACK scaling algorithm.
T_{min}, T_{max}	0.648, 0.876	0.795, 0.941
No. of measured, independent and observed [$I > 2\sigma(I)$] reflections	19400, 5697, 4758	21755, 7093, 4009
R_{int}	0.034	0.087
$(\sin\theta/\lambda)_{max}$ (Å^{-1})	0.617	0.617
Refinement		
$R[F^2 > 2\sigma(F^2)]$, $wR(F^2)$, S	0.044, 0.114, 1.05	0.057, 0.151, 1.01
No. of reflections	5697	7093

No. of parameters	407	623
No. of restraints	304	596
H-atom treatment	H-atom parameters constrained	H-atom parameters constrained
$\Delta\rho_{max}$, $\Delta\rho_{min}$ (e Å^{-3})	1.23, -1.05	1.50, -0.87

Computer programs: *CrysAlis PRO* 1.171.39.29c (Rigaku OD, 2017), *SHELXS2014*/7 (Sheldrick, 2015), *SHELXL2014*/7 (Sheldrick, 2015), *SHELXTL* v6.10 (Sheldrick, 2008).

Figure C5

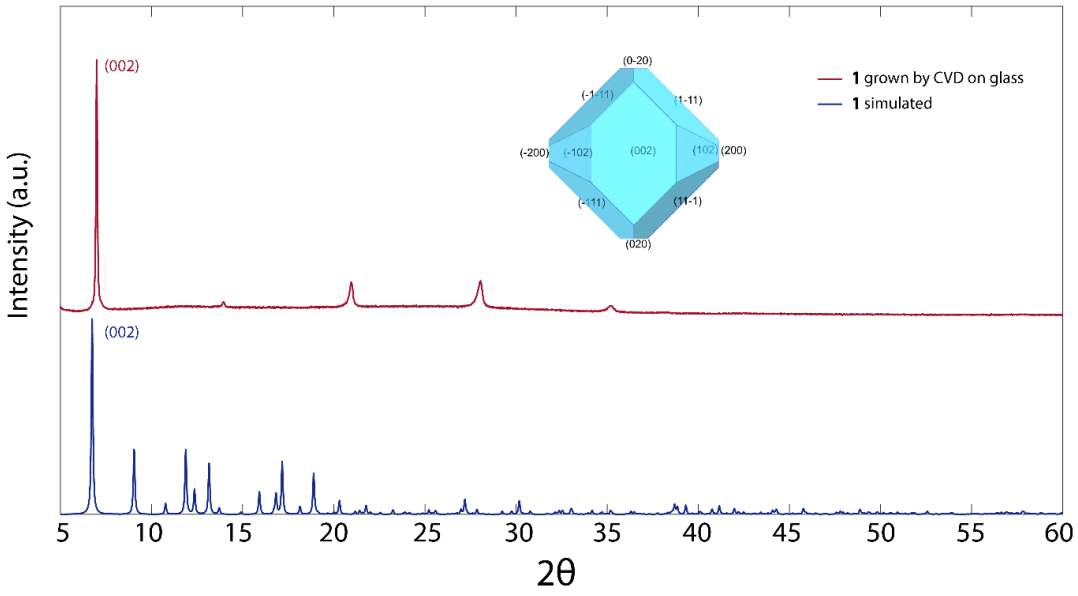

Figure C5 | pXRD and BFDH morphology of MF–104. pXRD of MF–104 grown on glass substrate (red) compared to a simulated pXRD pattern of MF–104 from its single crystal structure (blue). The intense peak at ~6.7° agrees well with the (002) reflection of the simulated diffraction pattern. The BFDH morphology calculated from Mercury also suggests that the crystals grow with the large (002) crystal face parallel to the glass substrate surface.

Figure C6

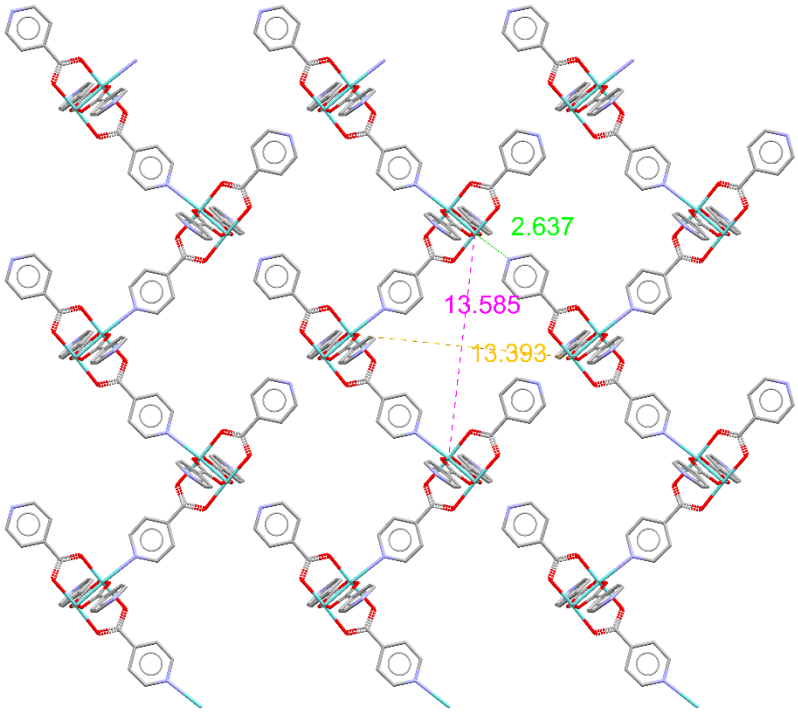

Figure C6 | Bond distances and body diagonals of MF–104. Body diagonals and Mo–N distances of MF–104. The Mo–N distance of 2.637 Å is longer than the 2.546(3) Å and 2.586(3) Å Mo–N bond lengths previously reported in the 2D phase. The measured body diagonals are in agreement with those reported for the square sub-cells of the 2D phase.

Figure C7

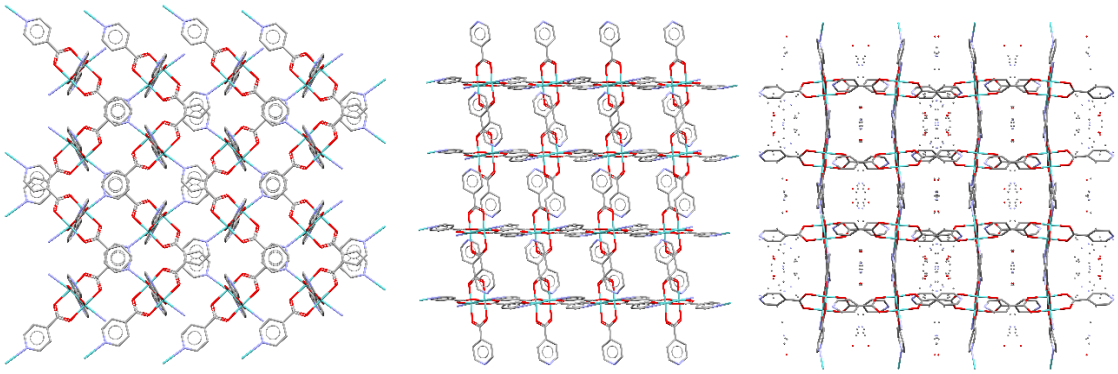

Figure C7 | Single crystal structure of MF–102. Crystal packing structure of MF–102 viewed down the *a* (left), *b* (center), and *c* (right) axes. Disordered DMA molecules are included in the view down the *c* axis to show solvent arrangement within the framework. We note that MF–104 has a void space of 350 $Å^3$ which corresponds to 6% of its unit cell (measured using a 2.0 Å probe radius), and that this space is consistent with uptake of DMA molecules required for conversion of MF–104 to MF–102. Though bulk and single crystal analyses repeatedly yielded the structure reported in this figure, we did observe on one occasion a closely-related variant of this 2D MOF. Details of this 2D MOF variant are provided in Figure C10.

Figure C8

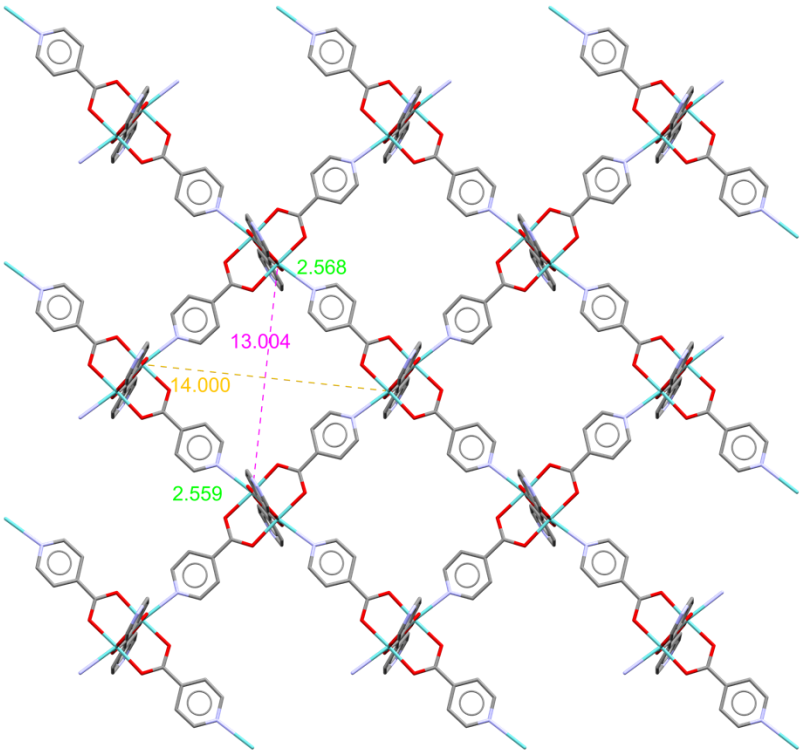

Figure C8 | Bond distances and body diagonals of 2. Body diagonals and Mo–N distances of MF–102. The Mo–N bond lengths of 2.568 Å and 2.559 Å agree well with the 2.546(3) Å and 2.586(3) Å Mo–N bond lengths previously reported for the 2D phase and are also shorter than the 2.637 Å Mo–N distance reported for MF–104. The measured body diagonals are also in agreement with those reported for the square sub-cells of the 2D phase.

Table C2 | Crystallographic data of 2D MOF variant

Crystal data	
Chemical formula	$C_{24}H_{16}Mo_2N_4O_8$
M_r	680.29
Crystal system, space group	Monoclinic, $C2/c$
Temperature (K)	110
a, b, c (Å)	16.4587 (2), 15.3102 (2), 14.3911 (2)
β (°)	95.7337 (15)
V (Å^3)	3608.21 (8)
Z	4
Radiation type	Cu $K\alpha$
μ (mm^{-1})	6.04
Crystal size (mm)	0.07 × 0.06 × 0.02
Data collection	
Diffractometer	SuperNova, Dual, Cu at zero, Atlas
Absorption correction	Analytical *CrysAlis PRO* 1.171.39.29c (Rigaku Oxford Diffraction, 2017) Analytical numeric absorption correction using a multifaceted crystal model based on expressions derived by R.C. Clark & J.S. Reid. (Clark, R. C. & Reid, J. S. (1995). Acta Cryst. A51, 887-897) Empirical absorption correction using spherical harmonics, implemented in SCALE3 ABSPACK scaling algorithm.
T_{min}, T_{max}	0.708, 0.910
No. of measured, independent and observed [$I > 2\sigma(I)$] reflections	10962, 3532, 3087
R_{int}	0.030
$(\sin\theta/\lambda)_{max}$ (Å^{-1})	0.616
Refinement	
$R[F^2 > 2\sigma(F^2)]$, $wR(F^2)$, S	0.031, 0.086, 1.06
No. of reflections	3532
No. of parameters	172
H-atom treatment	H-atom parameters constrained
Δr_{max}, Δr_{min} (e Å^{-3})	1.39, -0.51

Computer programs: *CrysAlis PRO* 1.171.39.29c (Rigaku OD, 2017), *SHELXS2014*/7 (Sheldrick, 2015), *SHELXL2014*/7 (Sheldrick, 2015), *SHELXTL* v6.10 (Sheldrick, 2008).

Figure C9

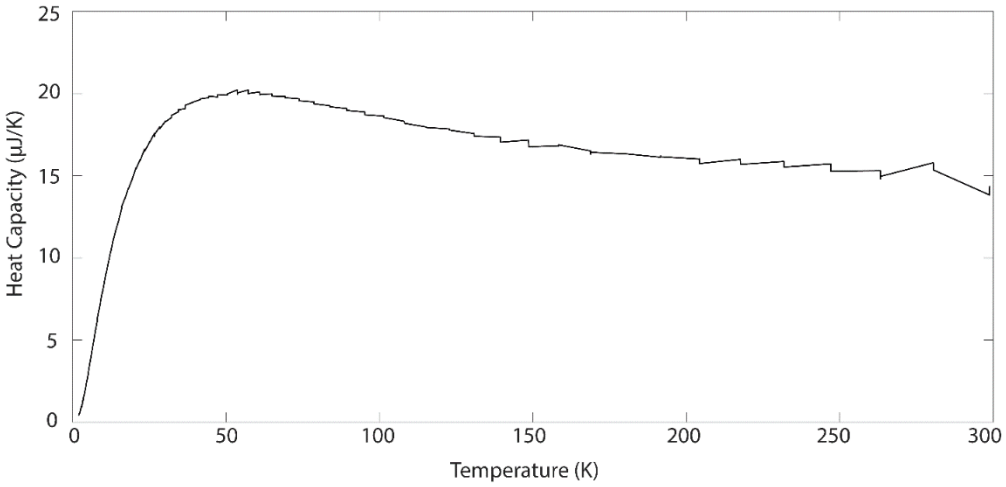

Figure C9 | Heat capacity data for MF–104. Heat capacity data for MF–104 after its conversion from MF–102 in the presence of methanol vapor. A 5.2 mg pellet was prepared from a dried sample of MF–104 and then analyzed from 2 K to 300 K. These data suggest this converted phase is stable at room temperature, an observation corroborated by our pXRD results.

Figure C10

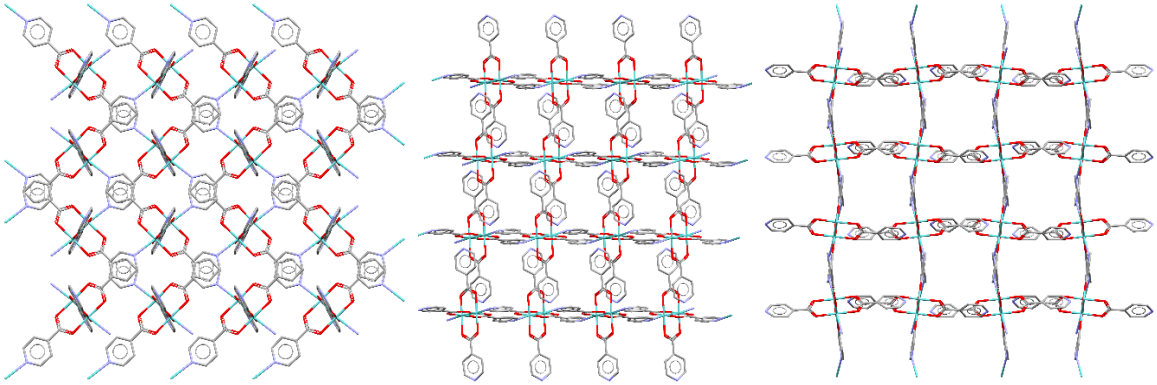

Figure C10 | Single crystal structure of 2D MOF variant. Crystal packing of an additional 2D phase viewed down the *a* (left), *b* (center), and *c* (right) axes. These structure data, though significantly similar to MF–102, suggest that solvent inclusion and intrinsic framework flexibility may facilitate the formation of assorted 2D phases.

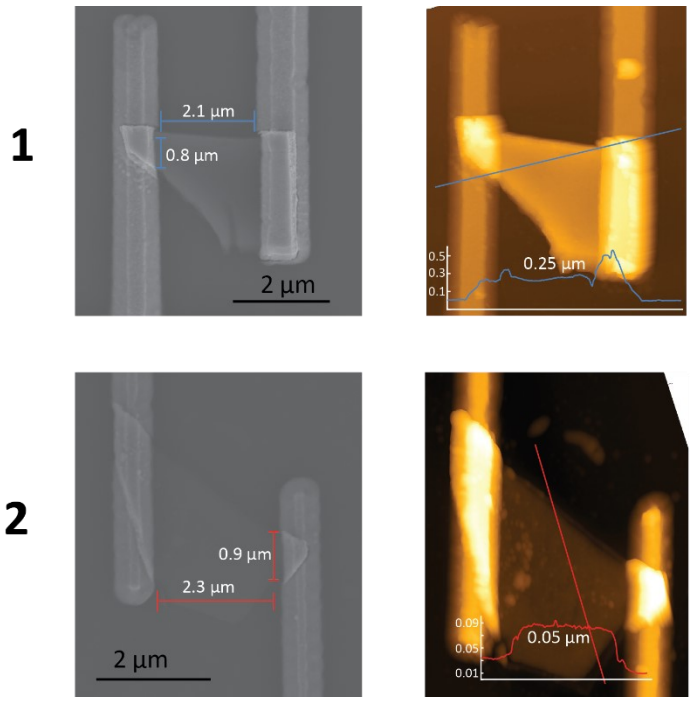

Figure C11 | Dimensions of devices of MF–104 and MF–102. SEM and AFM images of a device fabricated from exfoliated MF–104 (top) and MF–102 (bottom) crystals. The dimensions indicated here were used, in conjunction with measured current values (Figure 4.4) to calculate the conductivity of each device.

Figure C12

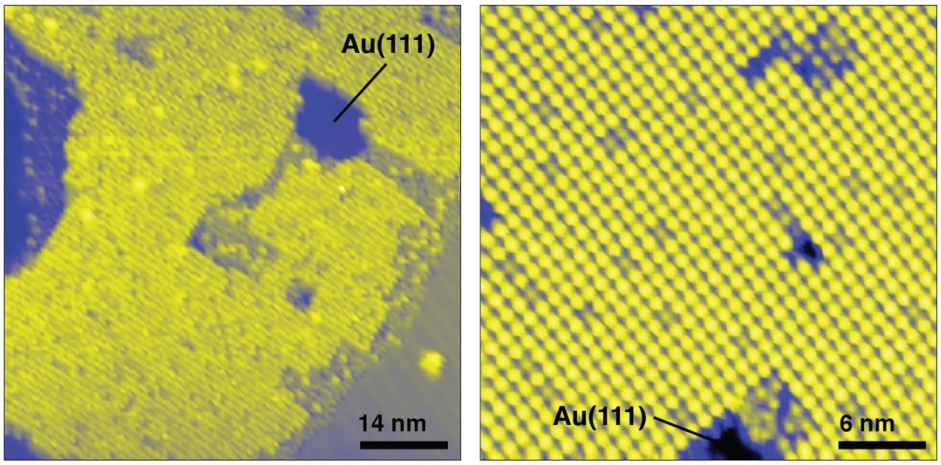

Figure C12 | STM maps of single layer $Mo_2(INA)_4$ on Au(111). STM maps collected after sample annealing. Cluster dose was adjusted to provide a 0.8 ML coverage. Under these conditions, bare Au(111) regions are visible and serve as a reference against which we verify that our 2D MOF is a single layer. The 2D MOF clearly persists over the Au(111) surface. *Imaging parameters*: V_{bias} = 0.05 V, I_{tunnel} = 5 pA.

Figure C13

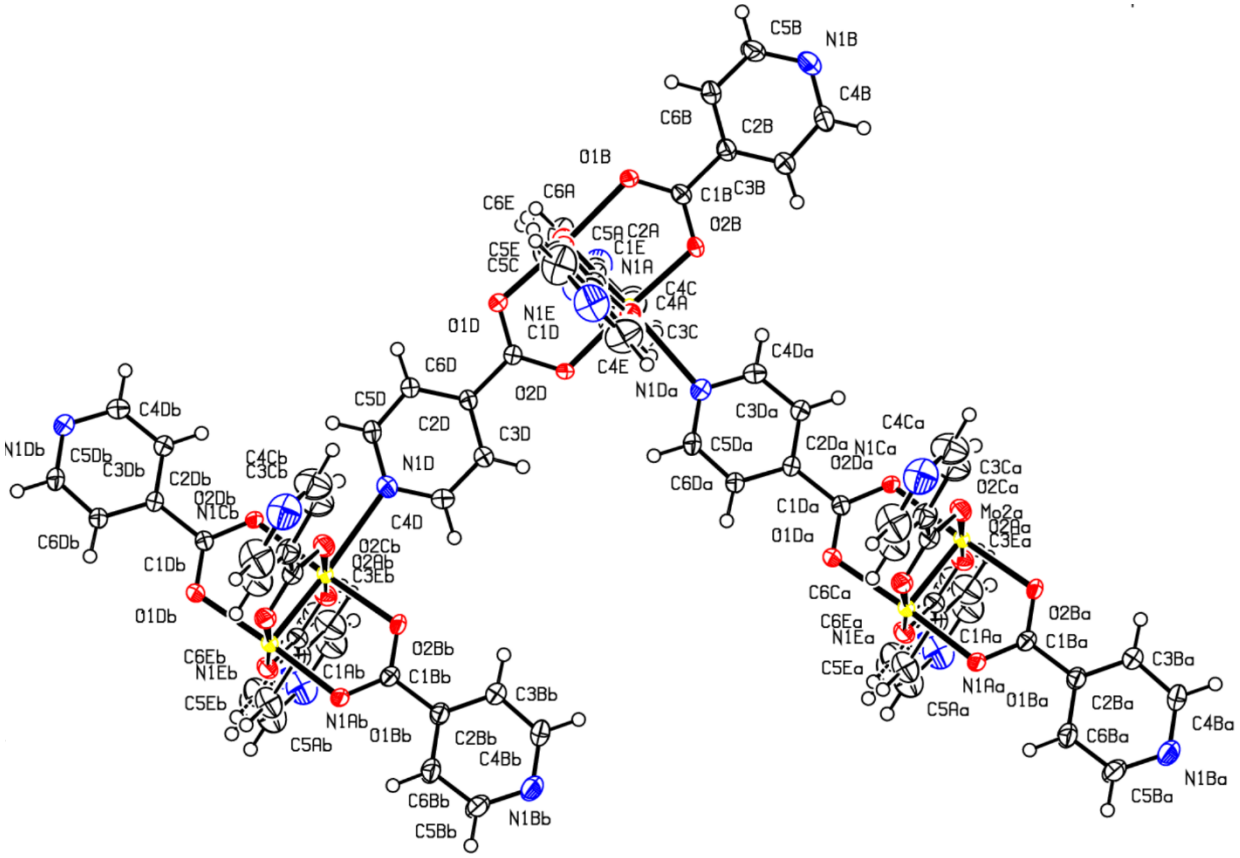

Figure C13 | Structural figure of MF–104. Crystallographic structure of MF–104 with ellipsoids set at 50% probability. See Table C1.

Figure C14

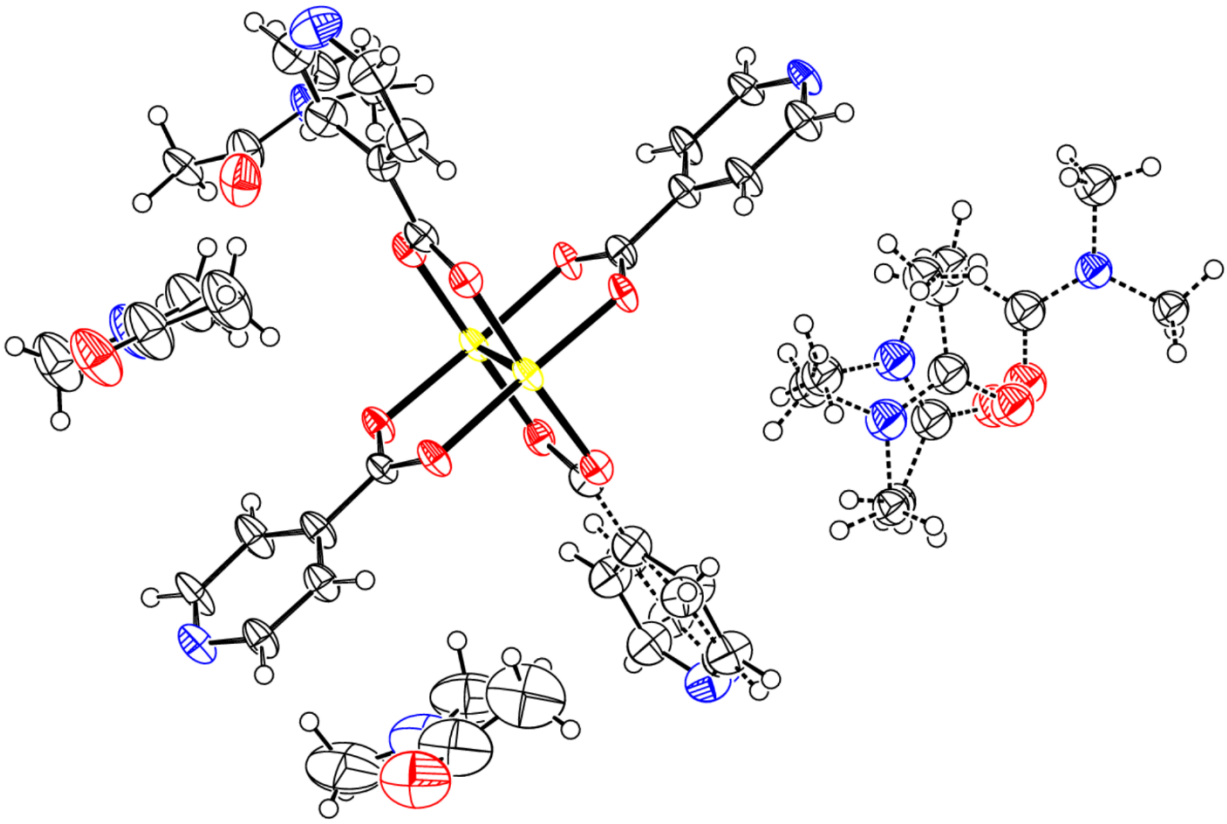

Figure C14 | Structural figure of MF–102. Crystallographic structure of MF–102 with ellipsoids set at 50% probability. See Table C1.

Figure C15

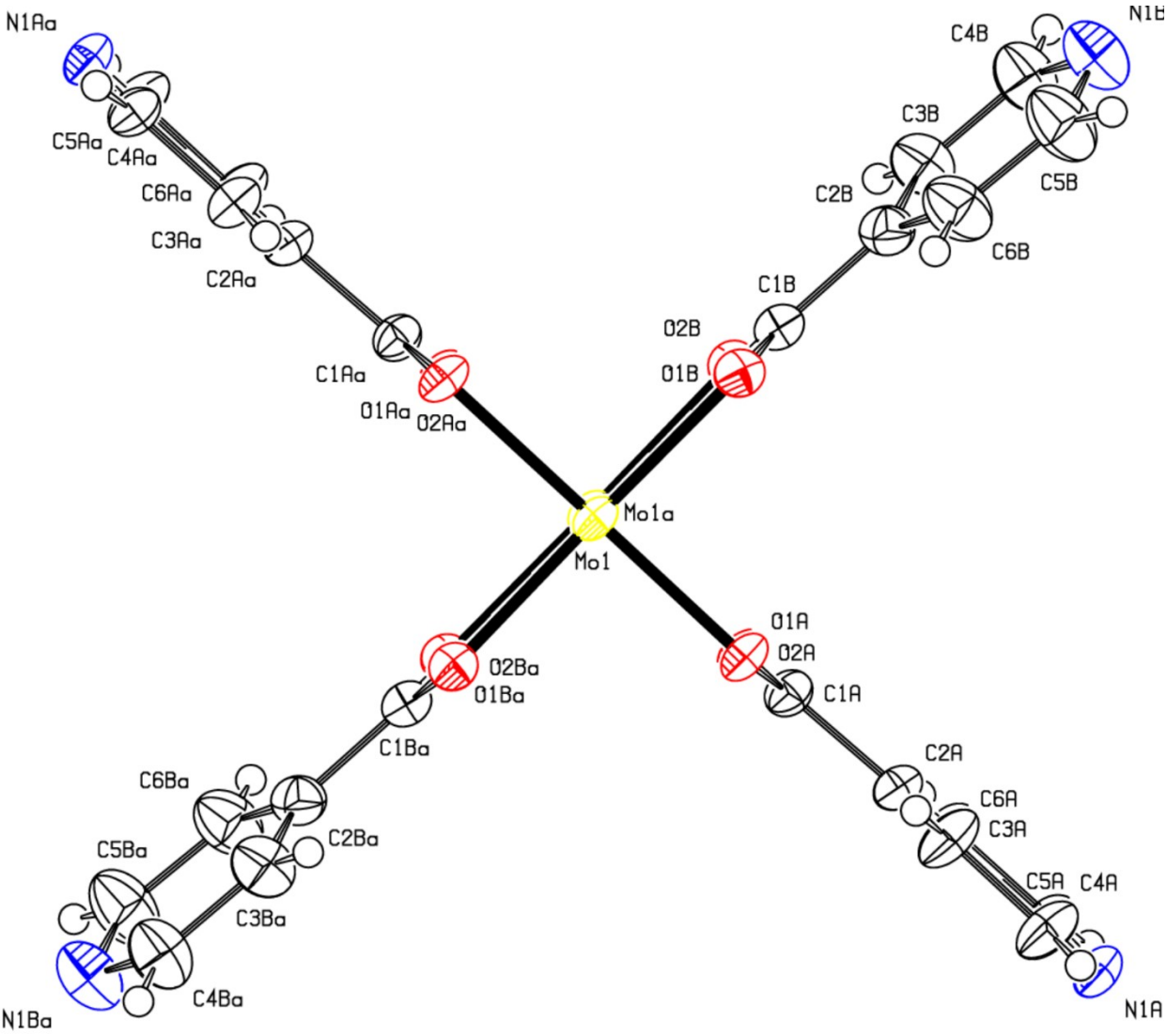

Figure C15 | Structural figure of 2D MOF variant. Crystallographic structure of 2D MOF variant with ellipsoids set at 50% probability. See Table C2.

REFERENCES

1. Nečas, D. & Klapetek, P. Gwyddion: an open-source software for SPM data analysis. *Cent. Eur. J. Phys.* **10**, 181–188 (2012).
2. Sheldrick, G. M. Crystal structure refinement with SHELXL. *Acta Crystallogr. Sect. C Struct. Chem.* **71**, 3–8 (2015).
3. Spek, A. L. Structure validation in chemical crystallography. *Acta Crystallogr. Sect. D Biol. Crystallogr.* **65**, 148–155 (2009).
4. Horcas I., Fernández R., Gómez-Rodríguez J.M., Colchero J., Gómez-Herrero J., Baro A.M. WSXM: A software for scanning probe microscopy and a tool for nanotechnology. *Rev. Sci. Instrum*. **78,** 013705 (2007).